NTNU
Norwegian University of Science and Technology

Modeling of Work Hardening for Aluminum Alloy Structures

Marius Eek
Kristian Kolstø Kaldager

Department of Structural Engineering
Faculty of Engineering Science and Technology
NTNU- Norwegian University of Science and Technology

MASTER THESIS 2016

SUBJECT AREA:	DATE:	NO. OF PAGES:
Computational Mechanics	June 10th 2016	20+92+41

TITLE:

Modeling of Work Hardening for Aluminum Alloy Structures

BY:

Marius Eek
Kristian Kolstø Kaldager

SUMMARY:
The hardening behavior of aluminum alloys can be described by a combined material model with both isotropic and kinematic hardening. The kinematic contribution is often excluded in numerical simulations if a cyclic stress state is not suspected, because additional experimental tests and calibration is required to include this contribution in the combined hardening model. This thesis examines the influence of a combined hardening model for an aluminum alloy AA6060 in tempers T4, T6 and T7 with respect to the structural response, compared to the increased complexity.

Pure tension, tension-compression and compression-tension load reversal tensile tests were performed in a uniaxial stress state. The experimental results obtained in this thesis showed a significant dispersion of the yield stress within each temper. The load sequence of the tensile tests was concluded to be insignificant for the experimental results. Distinct differences in the work hardening between the three tempers were experimentally observed. From the experimental data two material hardening models were calibrated: purely isotropic and combined isotropic-kinematic. These models were used for numerical finite element simulations of several cases in Abaqus including axial crushing, forming limit diagram, impact loading on stiffened plates and blast loading on clamped plates.

Temper T4 showed greater strain distribution and a reduced chance of fracture, compared to T6 and T7. The results found in this thesis suggest only minor differences between the two material hardening models. For the cases in this thesis it was concluded that using a combined material hardening model is not necessary for aluminum alloy AA6060 in tempers T4, T6 and T7, considering the increased cost and time required for additional calibration, when performing numerical simulations not subjected to considerable fluctuating stress states.

RESPONSIBLE TEACHER:	Professor Odd Sture Hopperstad
SUPERVISOR(S):	Professor Odd Sture Hopperstad, Professor Tore Børvik and PhD Candidate Bjørn Håkon Frodal
CARRIED OUT AT:	SIMLab, The Department of Structural Engineering, NTNU

Institutt for konstruksjonsteknikk
Fakultet for ingeniørvitenskap og teknologi
NTNU- Norges teknisk- naturvitenskapelige universitet

MASTEROPPGAVE 2016

FAGOMRÅDE:	DATO:	ANTALL SIDER:
Beregningsmekanikk	10. juni 2016	20+92+41

TITTEL:

Modellering av arbeidsherding i aluminium for styrkeanalyser

UTFØRT AV:

Marius Eek
Kristian Kolstø Kaldager

SAMMENDRAG:
Herdingsoppførselen til aluminiumslegeringer kan beskrives av en kombinert materialmodell med både isotropisk og kinematisk herding. Det kinematiske bidraget er som regel ekskludert i numeriske simuleringer hvis ikke en syklisk spenningstilstand er forventet, grunnet krav til ytterlige eksperimentelle tester og kalibreringer for å inkludere dets bidrag i den kombinerte arbeidsherdingsmodellen. Denne avhandlingen undersøker innvirkningen av en kombinert herdingsmodell for aluminiumslegeringen AA6060 i temperene T4, T6 og T7 på konstruksjonsoppførselen, tatt i betraktning den økte kompleksiteten.

Ren strekk, strekk-trykk og trykk-strekk lastreverserte materialtester ble utført i en enaksiell spenningstilstand. De eksperimentelle resultatene fra denne avhandlingen viste stor spredning mellom flytepunktene for hver temper. Lastrekkefølgen til materialtestene ble konkludert til å være ubetydelig for de eksperimentelle resultatene. Markante forskjeller i herdingen mellom de tre temperene ble observert eksperimentelt. De eksperimentelle dataene ble kalibrert til to herdningsmodeller: isotropisk og kombinert isotropisk-kinematisk. Disse modellene ble brukt i elementanalyser av forskjellige caser i Abaqus, inkludert stukning, formediagram, avstivede plater utsatt for konsentrert last og innspente plater utsatt for eksplosjonslast.

Temper T4 viste større tøyningsfordeling og dermed redusert sannsynlighet for brudd, sammenlignet med T6 og T7. Resultatene i denne avhandlingen viser kun små forskjeller mellom de to herdningsmodellene. For de simulerte casene i denne avhandlingen ble det konkludert at en kombinert herdningsmodell ikke er nødvendig for aluminiumslegeringen AA6060 i temperene T4, T6 og T7, tatt i betraktning de økte kostnadene og den ekstra tiden som kreves for kalibrering, når numeriske simuleringer uten betraktelig varierende spenningstilstander blir gjennomført.

FAGLÆRER: Professor Odd Sture Hopperstad

VEILEDER(E): Professor Odd Sture Hopperstad, Professor Tore Børvik og
ph.d. kandidat Bjørn Håkon Frodal

UTFØRT VED: SIMLab, Institutt for konstruksjonsteknikk, NTNU

Department of Structural Engineering
FACULTY OF ENGINEERING SCIENCE AND TECHNOLOGY
NTNU – Norwegian University of Science and Technology

MASTER'S THESIS 2016

for

Marius Eek og Kristian Kolstø Kaldager

Modeling of Work Hardening for Aluminum Alloy Structures

1. INTRODUCTION

Accurate modeling of work hardening is of utmost importance in simulation of structural collapse or structural impact. Work hardening affects both the capacity and ductility predicted in such simulations. The influence of work hardening on capacity is obvious, as the strength of the material increases with plastic straining, while the influence on structural ductility is less apparent. However, work hardening tends to distribute the plastic deformations over a larger region and thus lower the plastic strains and the required ductility of the material. There are two main types of work hardening: isotropic and kinematic. Isotropic hardening is due to evenly distributed storage of dislocations giving an isotropic increase of the material's yield strength. Kinematic hardening is caused by internal stresses in the material (so-called back stresses) which typically are induced by hard and soft regions in the material, e.g. hard particles in a soft matrix, or two-phase materials with a soft and a hard phase. Kinematic hardening leads to deformation-induced anisotropy: an initially isotropic material becomes plastically anisotropic during plastic deformation. The topic of this thesis is experimental characterization and numerical modeling of work hardening in AA6060 aluminum alloy with several different heat treatments.

2. OBJECTIVE

The main objectives of this thesis are to characterize the isotropic-kinematic hardening of AA6060 aluminum alloy as function of the heat treatment, to establish models for the observed behavior in Abaqus, and to study the influence of kinematic hardening on a range of structural components and load cases.

3. TASKS

The main topics in the research project will be as follows:

1. Literature study on the physical mechanisms responsible for work hardening in metallic materials and physically-based and phenomenological modeling strategies.
2. Experimental study on isotropic-kinematic hardening in AA6060 in several tempers.
3. Assessment of physically-based models and calibration of phenomenological models for isotropic-kinematic hardening.
4. Case studies with Abaqus on the influence of combined isotropic-kinematic hardening on the structural response, e.g. formability, structural collapse, crashworthiness and structural impact.

Supervisors: Odd Sture Hopperstad, Tore Børvik, Bjørn Håkon Frodal (NTNU)

The thesis must be written according to current requirements and submitted to the Department of Structural Engineering, NTNU, no later than June 10th, 2016.
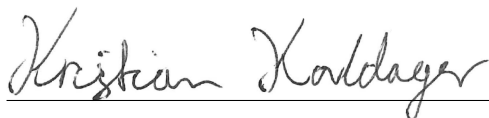
NTNU, January 15th, 2016.

Odd Sture Hopperstad
Professor

Preface

This thesis was written during 20 weeks in the spring of 2016 for Structural Impact Laboratory (SIMLab) at the Department of Structural Engineering at the Norwegian University of Science and Technology (NTNU), as the concluding requirement for the degree in Master of Science in Engineering and ICT, Structural Engineering with specialization in Computational Engineering. The experiments were founded by Centres for Research-based Innovation (SFI), Centre for Advanced Structural Analysis (CASA) and performed in the laboratory at the Department of Structural Engineering. It should be noted that neither of the authors of this thesis have taken a formal course in Materials Mechanics prior to this thesis. Therefore, in collaboration with the supervisor, the physically-based models and the associated theory have been omitted from the scope of this thesis. The authors have included substantial theory on the Cockcroft-Latham fracture criterion, considering its minor use in this thesis, for educational purposes.

Trondheim, June 10, 2016

Kristian Kolstø Kaldager   Marius Eek

Acknowledgments

Abstract

The hardening behavior of aluminum alloys can be described by a combined material model with both isotropic and kinematic hardening. The kinematic contribution is often excluded in numerical simulations if a cyclic stress state is not suspected, because additional experimental tests and calibration is required to include this contribution in the combined hardening model. This thesis examines the influence of a combined hardening model for an aluminum alloy AA6060 in tempers T4, T6 and T7 with respect to the structural response, compared to the increased complexity.

Pure tension, tension-compression and compression-tension load reversal tensile tests were performed in a uniaxial stress state. The experimental results obtained in this thesis showed a significant dispersion of the yield stress within each temper. The load sequence of the tensile tests was concluded to be insignificant for the experimental results. Distinct differences in the work hardening between the three tempers were experimentally observed. From the experimental data two material hardening models were calibrated: purely isotropic and combined isotropic-kinematic. These models were used for numerical finite element simulations of several cases in Abaqus including axial crushing, forming limit diagram, impact loading on stiffened plates and blast loading on clamped plates.

Temper T4 showed greater strain distribution and a reduced chance of fracture, compared to T6 and T7. The results found in this thesis suggest only minor differences between the two material hardening models. For the cases in this thesis it was concluded that using a combined material hardening model is not necessary for aluminum alloy AA6060 in tempers T4, T6 and T7, considering the increased cost and time required for additional calibration, when performing numerical simulations not subjected to considerable fluctuating stress states.

Contents

Nomenclature

α Stress ratio coefficient

$\bar{\sigma}$ Von Mises equivalent stress

β Incremental strain ratio coefficient

χ Backstress term for kinematic hardening

χ_{0i} Initial backstress for current half cycle

χ_{ij} Backstress tensor for kinematic hardening

$\Delta\sigma$ Stress differential

δ_{ij} Kronecker delta

$\dot{\lambda}$ Plastic parameter

$\dot{\varepsilon}$ Nominal strain rate

$\dot{\varepsilon}_{III}$ Third principle strain ratio

$\dot{\varepsilon}_{II}$ Second principle strain ratio

$\dot{\varepsilon}_{I}$ First principle strain ratio

$\dot{p}$ Equivalent plastic strain rate

η_i Combined hardening constraint coefficient

μ Lode parameter

ν Poisson's ratio

ω Damage parameter

σ^* Stress triaxiality

σ_0 Yield stress

σ_{eq} Equivalent stress

σ_H Hydrostatic stress

σ_{IH} Isotropic work hardening

σ_{III} Third principle stress

σ_{II} Second principle stress

σ_{ij} Cauchy stress tensor

σ_I First principle stress

σ_{KH} Kinematic work hardening

σ_t Cauchy (true) stress

θ_L Lode angle

$\tilde{u}$ Displacement integration variable

ε General strain

ε^e Elastic strain

ε_l^e Longitudinal elastic strain

ε^p Plastic strain

ε_l^p Longitudinal plastic strain

ε_U^p Plastic strain at necking

ε_0^p Initial plastic strain of current half cycle

$\varepsilon_{l,\text{off}}$ Longitudinal strain offset

ε_l Longitudinal strain

ε_r Radial strain

ε_{II} Second principle strain

ε_I First principle strain

ϑ Notation for sign function

A Current area of the minimal cross sectional geometry

a Specimen radius

A_0 Initial area

$C_{\chi i}$ Kinematic material hardening parameter

C_i Material hardening parameter

C_{Ri} Isotropic material hardening parameter

d Current diameter

D_0 Initial diameter of the minimal cross sectional geometry

d_0 Initial diameter

D_x Current diameter in x-direction

D_y Current diameter in y-direction

E Young's modulus

F Current applied force

f Yield function

F_m Mean force

L_0 Initial specimen gauge length

P Pressure

p Equivalent plastic strain

p_0 Initial equivalent plastic strain of current half cycle

p_f Equivalent plastic fracture strain

$Q_{\chi i}$ Kinematic material hardening parameter

Q_i Material hardening parameter

Q_{Ri} Isotropic material hardening parameter

R Isotropic hardening term

r Necking radius

R_H Yield point of the second half cycle

T Temperature

t Time

u Displacement

U_H Ultimate stress before load reversal

v Displacement velocity

W_c Fracture parameter

1 | Introduction

1.1 Background and Motivation

The material hardening model for aluminum alloys can be described by a combined model with both isotropic and kinematic hardening. In numerical simulations the total work hardening of the material is often simplified as isotropic, due to the simple calibration of isotropic material parameters by a uniaxial tensile test. Kinematic hardening is usually only included for models describing cycling loading patterns. This is due to the isotropic hardening's inability to describe the so-called Bauschinger effect [1, 2]. The kinematic hardening model is more complex and will need load reversal or cyclic material testing to calibrate the material model, which is more costly and time consuming.

The work hardening of metals has been studied for decades [3] and various mathematical material hardening models have been proposed for both isotropic and kinematic hardening. The isotropic hardening model most commonly used in materials such as aluminum is the Voce rule [4]. For kinematic hardening, a nonlinear model was proposed by Armstrong and Frederick [5] to describe time independent plasticity and the Bauchinger effect [2]. This nonlinear hardening model was evaluated by Chaboche [6] for stainless steel and is now commonly used.

Several studies have been conducted to describe the physically-based theory of kinematic work hardening of a material at the microscopic level. The influence of dislocations on work hardening is widely studied, and exemplified by Zhao and Holmedal [3], and Myhr et al. [7].

Several papers validate kinematic hardening models by conducting experimental studies and calibrating the obtained data to an existing model. AThis was performed in the paper by Hopperstad et al. [8], where the combined material hardening model from Chaboche [6] is calibrated for AA6060 in temper T4 from cyclic experimental data. Another calibration method has been used by Zhao and Lee [9], where a combined model is calibrated by exper-

1

imental results from bending. A reduced-parameters method for the hardening calibration was proposed by Tarigopula et al. [10], to simplify the calibration process by reducing the complexity of the material hardening model.

In the computer program Nano Structure Model (NaMo) developed from Myhr et al. [7], material parameters can be calculated based on the material's temperature history, but at the present time this only includes the isotropic hardening. A motivation for conducting this thesis is to get a basis for including the kinematic hardening as well in this program.

1.2   Objectives

The three main objectives of this thesis are an experimental study, a calibration of isotropic and combined material hardening models and an investigation of the importance of kinematic hardening in analyses of structural problems subjected to various stress states, excluding cyclic loading.

To study experimentally the isotropic and combined material hardening for aluminum alloy AA6060 in tempers T4, T6 and T7, pure tensional and load reversal tensile tests were performed. The tensile tests were divided into three load sequences to investigate the impact of the sequence on the work hardening. These were pure tension, tension-compression and compression-tension.

To calibrate material models from the experimental results, various methods were used to calculate the material parameters. The isotropic hardening model was calibrated with the Voce rule [4], and the kinematic model was calibrated with methods inspired by Manes et al. [11] and Tarigopula et al. [10].

The objective of the case study is to investigate whether a combined hardening model should be considered for numerical models not directly subjected to cyclic loading, and consider if the increased accuracy is worth the extra time and costs of calibrating a combined hardening model. This was done using numerical simulations in Abaqus for several cases. The included cases are based on the axial crushing performed by Hoang et al. [12], impact loading on stiffened plates by Langseth et al. [13] and blast loading on plates by Aune et al. [14]. A forming limit diagram is also included in the case study. These cases represent a wide variety of structural responses, which hopefully will uncover the importance of kinematic hardening.

1.3 Organization of Thesis

The thesis consists of four main parts: Literature study, experimental study, material calibration and case study. These topics are divided into chapters, and an outline of each of them follows:

Chapter 2 - Theory
Provides adequate theoretical background for the various methods and topics presented in this thesis.

Chapter 3 - Experimental Procedures
Description of the initial test preparations and laboratory experiments, followed by the experimental results.

Chapter 4 - Material Processing
Explanation of the various methods used to obtain the material parameters needed for the material models and implementation of a fracture criterion.

Chapter 5 - Case Studies
Description of the selected cases and the results from Abaqus. A short individual discussion is given for each case.

Chapter 6 - Concluding Remarks
Concluding remarks on the methods used and the results obtained are presented for the four main parts of the thesis.

2 | Theory

This chapter contains some of the theory concerning this thesis. It will provide key theories and formulas on major topics while not going into too much details on topics that are of less importance. If the reader should require additional information on a specific topic most sections have material for further reading. The formulas provided here do not consider strain rate, as the AA6060 aluminum alloy can be considered strain rate insensitive as indicated by the study of Chen et al. [15]. This is also indicated by Zukas et al. [16] in Figure 2.1, where it can be seen that heat treated aluminum alloys show minuscule strain rate sensitivity.

First, the chapter will provide adequate theory on the mechanics of metals and its applications in experimental material tensile tests. Secondly, theory concerning plasticity and work hardening is provided as it is the main topic of this thesis. Theory on the Cockcroft - Latham fracture criterion is also provided. Finally, theory on aluminum alloys and strengthening mechanisms is included.

2.1 Mechanical Behavior of Metals

The relative behavior of metals can be described with strain and stress [1]. Strain is defined as the deformation of a metal body subjected to forces and/or stresses. Stress is defined as the internal forces per area that material particles exert on each other in the metal. For small strains the response is said to be elastic, i.e. the material will reclaim its initial shape after the applied load or stress is removed. However, for larger strains the material will begin to yield and it will go into the plastic region of deformation. Further stress applied to the material after this will result in plastic strain and will not be recovered if the applied load or stress is then removed. Moreover, in this plastic state the material will work harden.

An infinitesimal stress element is shown in Figure 2.2 for a two-dimensional stress state where the shear stresses are zero. This state refers to a specific value for the stress in both
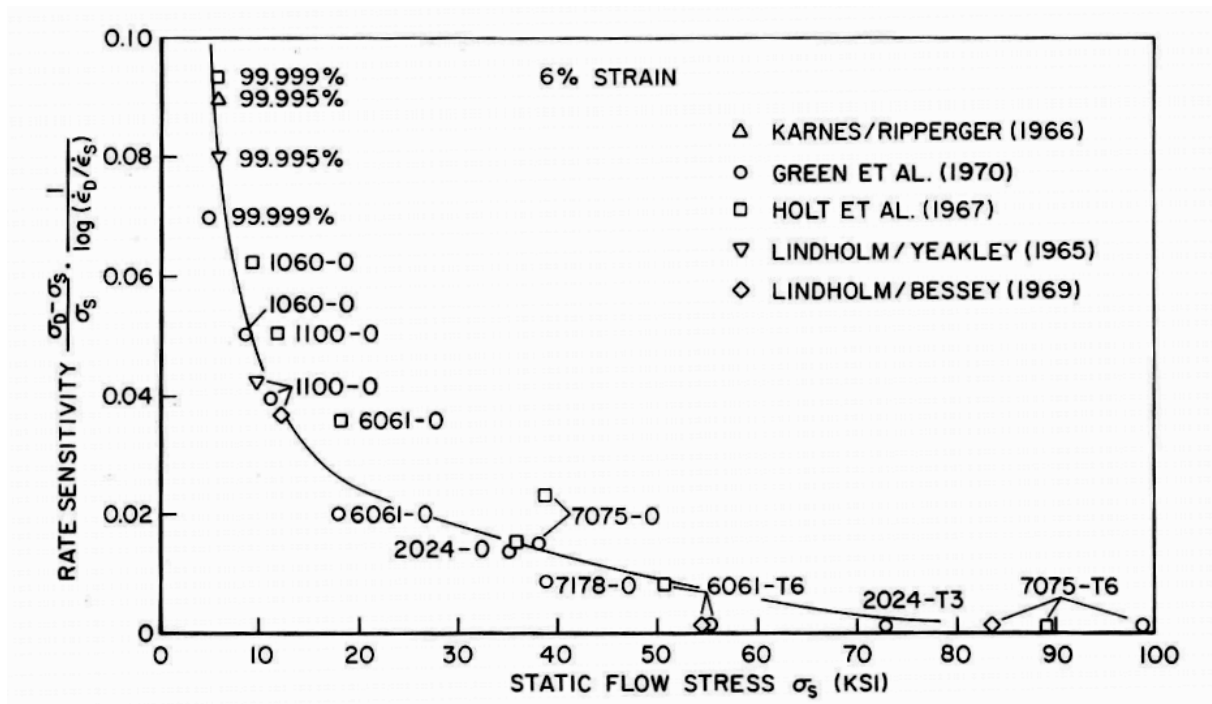
5

Figure 2.1: Strain rate sensitivity of aluminum alloys and their tempers from Zukas et al. [16]

the major, σ_I, and the minor direction, σ_{II}. If either the major or the minor stress is zero and the other is not, the stress state is referred to as uniaxial. Theory concerning this is covered by the following sections.
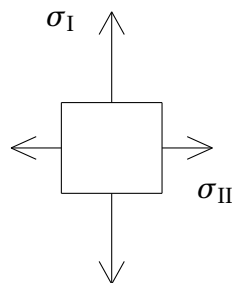

Figure 2.2: Principal stresses as shear stress is zero

2.1.1 Experimental Measures

To accommodate the experimental data provided by the tensile tests later in the thesis, this section contains theoretical background for experimental measures. Theory provided for the experimental measures are described for a uniaxial stress state. The Cauchy (true) stress, σ_t, is defined as

$$\sigma_t = \frac{F}{A} \tag{2.1}$$

where F is the current applied force and A is the current area of the minimal cross sectional geometry. This current area, is calculated based on measured diameters as

$$A = \frac{\pi}{4} D_x D_y \tag{2.2}$$

where D_x and D_y are perpendicular diameters provided by the tensile test data. In these tests diameter and force were given at the current time, therefore the strain and stress needs to be expressed from this. If plastic incompressibility and an isotropic material is assumed, the radial strain, ε_r, of a circular body is defined as

$$\varepsilon_r = ln\frac{d}{d_0} = -ln\frac{d_0}{d} = -\frac{1}{2}ln\frac{A_0}{A} \tag{2.3}$$

Here d denotes the current diameter and d_0 and A_0 are the initial values for the diameter and area, respectively. For considerable stress and strains in metals, the strain is defined by an elastic and a plastic term. The elastic term represents the reversible material deformation and the original geometry will be recovered if the specimen is unloaded. The plastic term will not recover the original geometry, as energy is used to permanently alter the specimen. Generally the strain, ε, can therefore be expressed with an elastic and a plastic strain component as

$$\varepsilon = \varepsilon^e + \varepsilon^p \tag{2.4}$$

where ε^e is the elastic strain component and ε^p is the plastic strain component. Under the assumption of plastic incompressibility and Hooke's law with Poisson's ratio, ν, the relationship between the radial and longitudinal strains, ε_r and ε_l, and their respective terms are defined by Rakvåg et al. [17] as

$$\varepsilon_r = \varepsilon_r^e + \varepsilon_r^p = -\nu\varepsilon_l^e - \frac{1}{2}\varepsilon_l^p = -\nu\varepsilon_l^e - \frac{1}{2}(\varepsilon_l - \varepsilon_l^e) \tag{2.5}$$

where $(*)^e$ denotes the elastic term and $(*)^p$ the plastic term. Solving this for the longitudinal strain, ε_l, yields

$$\varepsilon_l = -2\varepsilon_r + (1-2\nu)\varepsilon_l^e \tag{2.6}$$

The longitudinal elastic strain, ε_l^e is governed by Hooke's law. Using this law and Equation (2.4), an expression can be established for the longitudinal plastic strain, ε_l^p.

$$\sigma_t = E\varepsilon_l^e = E\left(\varepsilon_l - \varepsilon_l^p\right); \quad \varepsilon_l^p = \varepsilon_l - \frac{\sigma_t}{E} \tag{2.7}$$

Here E is the Young's modulus. Inserting equation (2.3) into the expression for the longitudinal strain (2.6) and using Hooke's law for the elastic longitudinal strain yields the following equation

$$\varepsilon_l = ln\frac{A_0}{A} + (1 - 2v)\frac{F}{AE} \tag{2.8}$$

The longitudinal strain is expressed as a function of the area and force. By expressing both the initial and current area with the equivalent diameter values from equation (2.2) yields

$$\varepsilon_l = ln\frac{D_0^2}{D_x D_y} + (1 - 2v)\frac{4F}{\pi D_x D_y E} \tag{2.9}$$

D_0 is the initial diameter of the minimal cross sectional geometry. After localization of the deformed part along the gauge length of the tensile test, defined as diffuse necking, the Cauchy stress no longer correctly represents the stress state in the material as it is no longer uniaxial. By using the Bridgman correction [18], the equivalent stress, σ_{eq}, can be calculated as

$$\sigma_{eq} = \frac{\sigma_t}{\left(1 + 2\frac{r}{a}\right)\left[ln\left(1 + \frac{a}{2r}\right)\right]} \tag{2.10}$$

where a is the specimen radius and r is the necking radius. The fraction $\frac{a}{r}$ can be approximated by experimental results from Le Roy et al. [19] as

$$\frac{a}{r} = 1.1\left(\varepsilon^p - \varepsilon_U^p\right), \quad \varepsilon^p > \varepsilon_U^p \tag{2.11}$$

Here ε_U^p is the plastic strain at necking. This measure is further explained in Section 2.2.1 and by equation (2.18). It should be noted that for strains less than the plastic strain at necking, the equivalent stress is equal to the Cauchy stress.

$$\sigma_{eq} = \sigma_t, \quad \varepsilon^p \leq \varepsilon_U^p \tag{2.12}$$

2.2 Plasticity

In material mechanics of solids, plasticity is the permanent deformation of solids when subjected to considerable stress. This is contrary to the elastic behavior which will allow reversible deformation as the solid is unloaded. The yield surface marks the change between these two material states in a triaxial stress state. When the material undergoes plastic deformation the material will work harden. This hardening is split into two categories: isotropic and kinematic hardening. This section provides theory on general plasticity, followed by details on each of the work hardening types.

2.2.1 Yield Criterion

With tensor notation the yield function, f, is defined as [1]

$$f = \sqrt{\frac{3}{2}\left(\sigma'_{ij} - \chi'_{ij}\right)\left(\sigma'_{ij} - \chi'_{ij}\right)} - (\sigma_0 + R) \leq 0 \tag{2.13}$$

Here σ_0 is the initial yield stress, R is the isotropic hardening term and is further explained in the following section. The material will yield whenever the yield function is equal to zero and it is in the elastic material domain when the yield function is less than zero. The yield function cannot be more than zero as the material will undergo plastic loading when the function is equal to zero. During this loading the material will work harden by expanding (isotropic hardening) and translating (kinematic hardening) the yield surface. The tensors σ'_{ij} and χ'_{ij} are defined as

$$\sigma'_{ij} = \sigma_{ij} - \sigma_H \delta_{ij}, \quad \sigma_H = \frac{1}{3}\sigma_{kk} \tag{2.14}$$

$$\chi'_{ij} = \chi_{ij} - \frac{1}{3}\chi_{kk}\delta_{ij} \tag{2.15}$$

where σ_H is the hydrostatic stress and δ_{ij} is the Kronecker delta. χ_{ij} is the backstress tensor for the kinematic hardening and σ_{ij} is the Cauchy stress tensor. The tensile tests in this thesis are carried out in a uniaxial stress state. Due to this, further theory on the material parameters, such as yield stress, is provided only for this specific stress state. In this state the yield function, f, is now defined as

$$f(\sigma_{eq} - \chi, R) = |\sigma_{eq} - \chi| - (\sigma_0 + R) \tag{2.16}$$

χ is the backstress term for the kinematic hardening. This is further explained in Section 2.2.3. The notation $\vartheta = sgn(\sigma_{eq} - \chi)$ is introduced, where the relation that any number can be expressed as $x = sgn(x)|x|$ is used. The following expression is the total stress equation with both work hardening rules, given that $f = 0$ when the material yields

$$\sigma_{eq} = \vartheta[\sigma_0 + R(p)] + \chi(p) \tag{2.17}$$

Here p is the equivalent plastic strain and it has the following relationship with the plastic strain, ε^p, in the uniaxial case for cyclic loading within a half cycle

$$p = p_0 + \vartheta\left(\varepsilon^p - \varepsilon_0^p\right) \tag{2.18}$$

The zero subscript parameters are the initial values of the current half cycle. Where the half cycle is defined as the continuous stress-plastic strain function within the applied loading changing signs one time to the next.

2.2.2   Isotropic Hardening

Increasing the stress in the plastic domain during plastic loading will lead to an overall expansion of the yield surface, as seen in Figure 2.3a by the dotted ellipse, resulting in a work hardening of the material. In a uniaxial stress state it is important to note that the yield surface will be reduced to the two solid points in the figure. When the material work hardens by isotropic hardening these points will increase in both directions to the hollow points and thus increasing the stress required for the material to yield in both load directions. The isotropic part of the equivalent stress, Equation (2.17), $R(p)$, is commonly defined as the Voce Rule [4] and will be used in this thesis.

$$R(p) = \sum_{i=1}^{n} Q_{Ri}\left(1 - e^{-C_{Ri}p}\right) \tag{2.19}$$

where Q_{Ri} is an isotropic material hardening parameter, hence the R subscript. It is measured in MPa, and represents the overall growth possibility of the function, i.e. the horizontal asymptote. C_{Ri} is another isotropic material hardening parameter which represents the growth rate of the function. The total index n is the number of terms used to express the isotropic hardening.
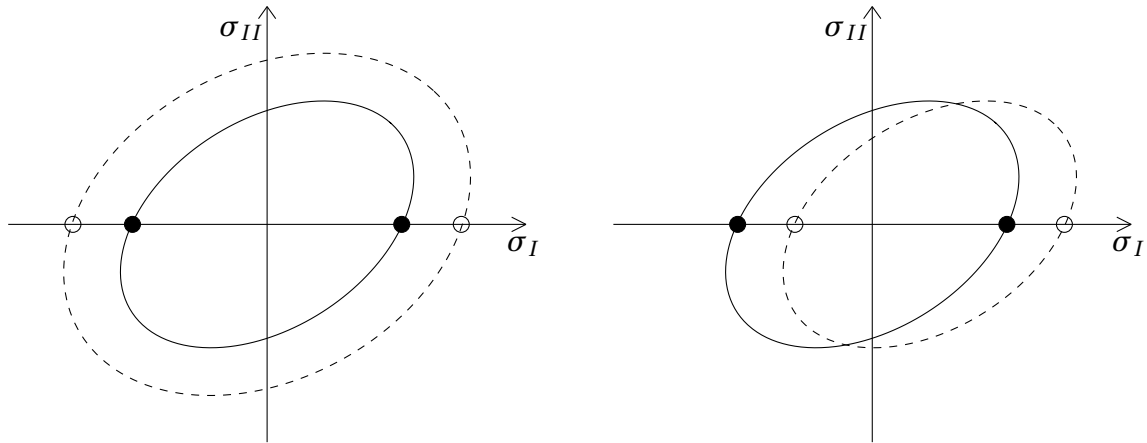
(a) Expansion of the yield surface by isotropic hardening

(b) Translation of the yield surface by kinematic hardening

Figure 2.3: Yield surface transformation by work hardening

2.2.3 Kinematic Hardening

If the strain increases and the material hardens with kinematic hardening, the yield surface is translated and not expanded as with isotropic hardening. This can be seen in Figure 2.3b by the dotted ellipse's center having been moved. This translation of the yield surface is what gives rise to the so called Bauschinger effect [2] in metallic materials subjected to cyclic loading conditions [20]. This effect will lower the yield stress when the material re-yields after the load reversal [1]. It is easier to acknowledge this effect if the uniaxial stress state is assumed. Then the yield surface will reduce to the two solid points shown in Figure 2.3b. When the material work hardens by kinematic hardening these two points will be translated along the σ_I-axis to the hollow points. The material in the figure yielded at the right solid point and the kinematic hardening will translate the yield surface to the right. If the loading is reversed, yielding will occur at the left hollow point, i.e. at an earlier point than before the kinematic hardening. The backstress term, χ, is defined by the Armstrong-Frederick's [5] nonlinear kinematic hardening rule, with notation from Tarigopula [10], as

$$\dot{\chi}_i = C_{\chi i} \left(Q_{\chi i} \vartheta - \chi_i \right) \dot{p} \tag{2.20}$$

where $(\dot{*})$ denotes the time derivative of a variable. Integration of this rate dependent equation for the backstress, with respect to the equivalent plastic strain, yields the following expression for the uniaxial state

$$\chi(p) = \sum_{i=1}^{n} \chi_i = \sum_{i=1}^{n} \vartheta Q_{\chi i} + \left[\chi_{0i} - \vartheta Q_{\chi i} \right] e^{-C_{\chi i}(p-p_0)} \tag{2.21}$$

In these equations, $Q_{\chi i}$ and $C_{\chi i}$ are the kinematic material hardening parameters and similarly to the isotropic term, they represent the total growth and the growth rate respectively. χ_{0i} is the initial backstress value for the current half cycle.

2.3   Cockcroft - Latham Fracture Criterion

To account for fracture in the finite element models, this thesis makes use of the ductile fracture criterion defined by Cockcroft and Latham [21].

$$\omega = \frac{1}{W_c} \int\limits_0^{p_f} \langle \sigma_I \rangle \, \mathrm{d}p \tag{2.22}$$

ω represents the damage ranging from 0 to 1, where 1 is full damage and 0 is none. W_c is the fracture parameter and represents the "plastic work" per unit volume for fracture. The quotation marks are due the first principle stress, σ_I, and not the equivalent stress, σ_{eq} being used here. However, in this thesis W_c will be approximated and calculated by the equivalent stress, σ_{eq}, which means that W_c is actually plastic work per unit volume for fracture. This will be further explained in Section 4.2.3. p_f is the equivalent plastic strain at fracture. $\langle \sigma_I \rangle$ is given by

$$\langle \sigma_I \rangle = \begin{cases} \sigma_I & \text{if } \sigma_I > 0 \\ 0 & \text{if } \sigma_I \leq 0 \end{cases} \tag{2.23}$$

For the cases presented in this thesis the fracture criterion will be used on shell elements, which are assumed to have a plane stress state. Further, for this thesis a Levy-Mises material is assumed, i.e. von Mises yield criterion, negligible elastic strains and associated flow rule [1]. The latter is defined as

$$\dot{\varepsilon}^p = \dot{\lambda} \frac{\partial f}{\partial \sigma} \tag{2.24}$$

where $\dot{\lambda}$ is the plastic parameter. This parameter is non-negative and larger than zero whenever the material is undergoing plastic loading. The principal stresses and principal strain rates are defined as [22]

$$\sigma_I > 0, \quad \sigma_{II} = \alpha \sigma_I, \quad \sigma_{III} = 0 \tag{2.25}$$

$$\dot{\varepsilon}_I > 0, \quad \dot{\varepsilon}_{II} = \beta \dot{\varepsilon}_I, \quad \dot{\varepsilon}_{III} = -\left(\beta + 1\right) \dot{\varepsilon}_I \tag{2.26}$$

Here $(\sigma_I, \sigma_{II}, \sigma_{III})$ are the principal stresses ordered so that the lower the subindex, the higher the value. $(\dot{\varepsilon}_I, \dot{\varepsilon}_{II}, \dot{\varepsilon}_{III})$ are the principal strain rates ordered in the same manner as the principal stresses. α and β are the stress ratio coefficient and the incremental strain ratio coefficient, respectively. α takes values in the range $-\infty < \alpha \leq 1$ while β takes values in the range $-2 < \beta \leq 1$. The coefficients have the following relationship by the assumption of a Levy-Mises material

$$\alpha = \frac{2\beta + 1}{\beta + 2}, \quad \beta = \frac{2\alpha - 1}{2 - \alpha} \tag{2.27}$$

The hydrostatic stress, σ_H, is defined here as the sum of the principal stresses and can be expressed with the incremental strain ratio by the following equation

$$\sigma_H = \frac{1}{3}(\sigma_I + \sigma_{II} + \sigma_{III}) = \frac{\beta + 1}{\beta + 2}\sigma_I \tag{2.28}$$

The von Mises equivalent stress, $\bar{\sigma}$, is defined as

$$\bar{\sigma} = \sqrt{\frac{1}{2}\left[(\sigma_I - \sigma_{II})^2 + (\sigma_{II} - \sigma_{III})^2 + (\sigma_{III} - \sigma_I)^2\right]} = \sqrt{3}\frac{\sqrt{\beta^2 + \beta + 1}}{\beta + 2}\sigma_I \tag{2.29}$$

The stress triaxiality, σ^*, is defined as the hydrostatic stress divided by the von Mises equivalent stress, yielding

$$\sigma^* = \frac{\sigma_H}{\bar{\sigma}} = \frac{1}{\sqrt{3}}\frac{\beta + 1}{\sqrt{\beta^2 + \beta + 1}} \tag{2.30}$$

where equation (2.28) and (2.29) have been used. In 1926 W. Lode [23] introduced the Lode parameter, μ, characterizing the deviatoric stress as

$$\mu = \frac{2\sigma_{II} - \sigma_I - \sigma_{III}}{\sigma_I - \sigma_{III}} \tag{2.31}$$

Given the plane stress state of the shell elements, the Lode parameter can be expressed as

$$\mu = \begin{cases} 3\frac{\beta + 1}{\beta - 1} & \text{for } -2 < \beta \leq -\frac{1}{2} \\ 3\frac{\beta}{\beta + 2} & \text{for } -\frac{1}{2} < \beta \leq 1 \end{cases} \tag{2.32}$$

In this stress state there is a one to one relationship between the Lode angle, θ_L, and the stress triaxiality, σ^*. The former is defined as

$$\theta_L = tan^{-1}\left(\frac{1}{\sqrt{3}}\mu\right) + \frac{\pi}{6} \tag{2.33}$$

Source	Si	Fe	Cu	Mn	Mg	Cr	Zn	Ti	Other	Al
ASM Committee (*)	0.3-0.6	0.1-0.3	0.1	0.1	0.35-0.6	0.05	0.15	0.1	0.15	Bal.
Westermann (**)	0.4	0.2	-	-	0.5	-	-	-	-	Bal.

Table 2.1: Chemical composition of AA6060 in wt% as given by ASM International Handbook Committee [26] (*) and the material used in this thesis, taken from Westermann et al. [27] (**)

For these definitions the Lode angle is defined to be in the range $0 < \theta_L \leq \frac{\pi}{3}$. For additional reading on this topic the reader is referred to Gruben et al. (2011) [22], which goes into details on the derivation for the plane stress and uniaxial stress state equations. The implementation of this theory is detailed in Section 4.2.3.

2.4 Aluminum and Strengthening Mechanisms

In its pure form aluminum is a lightweight, ductile and formable metal. Its density is $2700\,\mathrm{kg/m}^3$ and Poisson's ratio is $\nu = 0.33$ [24]. This pure form of the metal usually has a yield stress of 10 - 30 MPa [25], which can be improved immensely by introducing alloying elements and heat treatment. Doing so will alter the material properties significantly without compromising the low weight of the metal. For this thesis the alloy used is the aluminum alloy AA6060, also called AlMgSi [25].

2.4.1 AA6xxx Series

The main chemical compositions of the 6xxx alloy series are silicon and magnesium. This makes it possible to form magnesium silicide, Mg_2Si, which enables the alloys for heat treatment. Generally the alloys in the series have medium strength with good formability, weldability, machinability and corrosion resistance [26]. For the aluminum alloy AA6060, the chemical components measured in weight percent are specified in Table 2.1. The table details both the general chemical components of the alloy, and the specific material used in this thesis which were taken from Westermann et al. [27].

2.4.2 Heat Treatment and Tempers

The aluminum alloy used in this thesis underwent heat treatment by casting and then homogenization with a heat rate of 100 °C/h and a holding temperature of 585 °C for two and a half hours. After this the ingot was cooled at a rate of 300 °C/h and it was then spark eroded and machined into test specimens. They were subjected to a solution heat treatment of 520 °C for 15 minutes followed by water quenching. After 15 minutes of temporary storage in room temperature, the specimens were subjected to aging in oil as explained in the following paragraph. For a qualitative plot of the heat treatment with temperature, T, over time, t, after the casting, see Figure 2.4.

The "T" in the temper notation denotes that the alloy is solution heat treated. Tempers used in this thesis are defined hereunder:

- **T4**: Solution heat treated and naturally aged to a stable condition, also called underaged. Aged at room temperature.

- **T6**: Solution heat treated and artificially aged to peak strength. Aged at 175 °C for 8 hours.

- **T7**: Solution heat treated and artificially aged to be overaged. Aged at 175 ° for 11 days.

These three tempers have different material properties that make them useful for different applications. T4 is a more ductile temper with considerable work hardening, but lower yield stress than the other two tempers. The general consensus of these tempers are that the higher the temper number the less work hardening before tensile failure. T6 has the highest yield stress of the three tempers as this is peak aged, while the overaged T7 temper has a slightly lower yield stress.
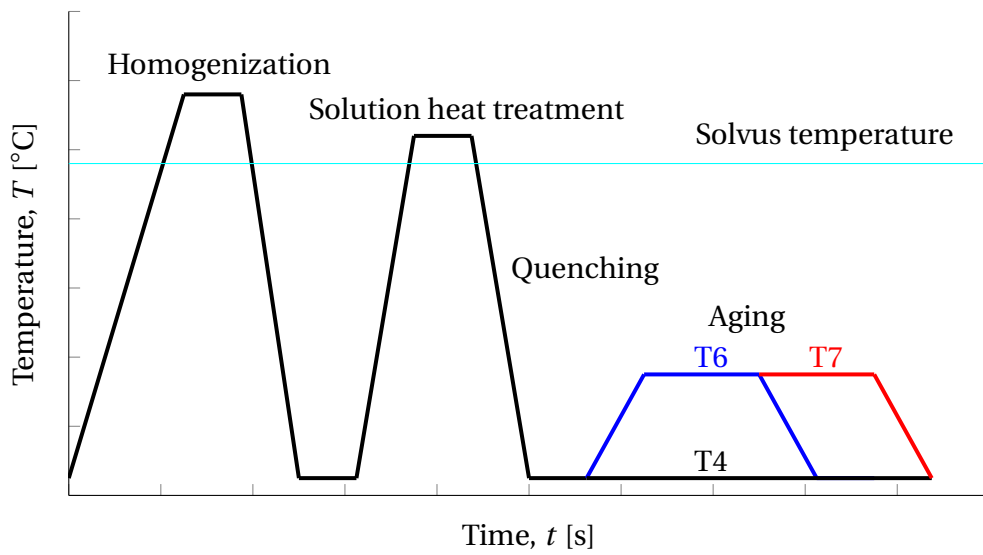
Figure 2.4: Qualitative plot of the heat treatment of AA6060 after casting

3 | Experimental Procedures

To calibrate the material model for both kinematic and isotropic hardening, uniaxial tensile tests were conducted for the three aluminum tempers described in Section 2.4.2. This chapter will first go into details about the material and its heat treatment. Next, the main focus of this chapter will be presented, detailing the experimental procedures of the tensile tests. This section presents details about preliminary calculations carried out before testing and the experimental setup is explained. Finally, the experimental results are presented.

3.1 Material

The 36 test specimens were spark eroded from a cast aluminum cylinder ingot and machined into the shape shown in Figure 3.1 and 3.2. The specific heat treatment for the specimens are described in Section 2.4.2. The heat treatment of the specimens was intended to follow the exact procedures described in Westermann et al. [28]. However, the observant reader will note that the solution heat treatment differs with the temperature of the solution being somewhat lower for the specimens used in this thesis, as described in Section 2.4.2. The actual effects of this difference are uncertain, nevertheless with the temperature difference being small and still above the solvus temperature it is not likely to cause any major differences in the material properties. However, this thesis will refrain from directly comparing results with Westermann's paper but rather follow its methods and use it as a verification tool for the material parameters.

3.2 Tensile Tests

The tensile tests were divided into twelve tests for each temper. To calibrate the material model of both the isotropic and kinematic hardening, the tests were divided into three stress
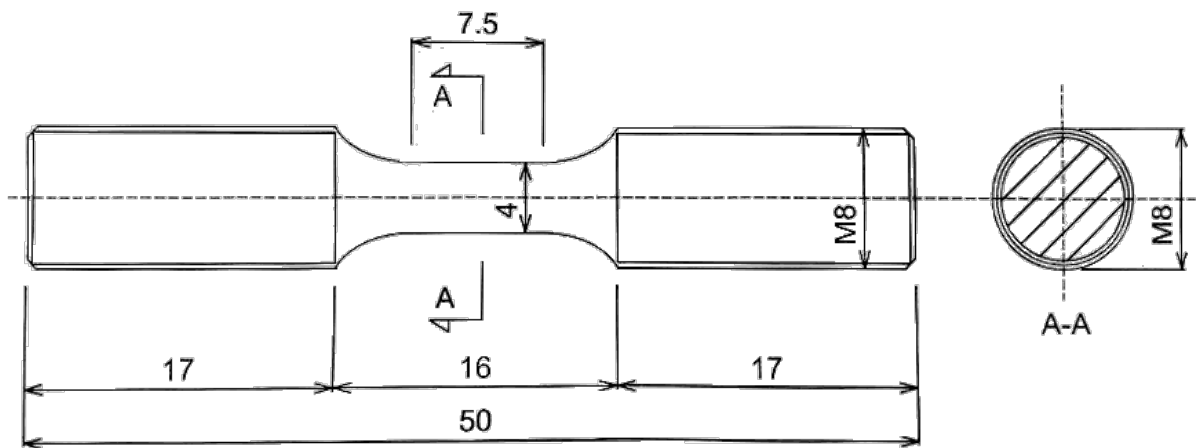
Figure 3.1: Cross sectional geometry of the tensile tests provided by Hydro Aluminium AS

Figure 3.2: Tensile test specimen

state patterns: pure tension, tension-compression, and compression-tension. This is detailed in Table 3.1, which shows the longitudinal strain levels, in percent, for the load reversal and the stopping point in the tension-compression case. In the table, "Fr" denotes the tensile test going to fracture. Both tension-compression and compression-tension tensile tests were performed to examine whether the loading sequence and type have any impact on the work hardening of the material. Two tensile test specimens after testing can be seen in Figure 3.3 with 3.3a showing the first pure tension T4 tensile test and 3.3b showing the T4 tension-compression tensile test no. 5 that was stopped at 6 % longitudinal strain in compression after going to 6 % longitudinal strain in tension before the load reversal.

| | | Tensile test type | |
No.	Tension	Tension-compression	Compression-tension
1	Fr	0.5% - 6.0%	0.5% - Fr
2	Fr	1.0% - 6.0%	1.0% - Fr
3	-	2.0% - 6.0%	2.0% - Fr
4	-	4.0% - 6.0%	4.0% - Fr
5	-	6.0% - 6.0%	6.0% - Fr

Table 3.1: Tensile test types and their strain reversal levels for each temper. "Fr" denotes the tensile test going to fracture

(a) Fractured tensile test

(b) Compressed tensile test
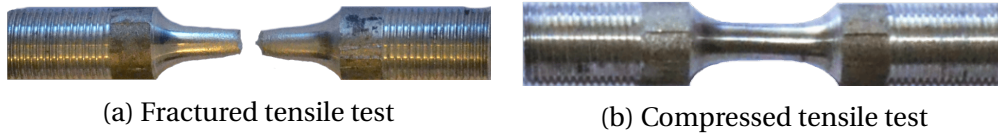
Figure 3.3: Tensile test specimens after experimental testing

3.2.1 Preliminary Calculations

Ten of the tensile tests were to have their load reversed at a specific longitudinal strain level. As previously stated the laser rig gave the current diameters of the minimal cross section. By using equation (2.9) for the longitudinal strain and solving this for the diameter, the load reversal point would be known. This nonlinear equation for the diameter used a Young's modulus, E, of 70 GPa, Poisson's ratio, v, of 0.33 [24] and the initial diameter, D_0, of the tensile test specimens were 4 mm. To find the current applied force, F, a tensile test was modeled in Abaqus/Implicit [29]. The mesh of the modeled tensile test is shown in Figure 3.4. The characteristic element size varied from 0.53 mm in the largest elements to 0.26 mm in the smallest elements, which were located in the minimal cross section of the gauge length. The tensile test was modeled with solid elements C3D8R without a fracture criterion. The displacing velocity was set to 2.25 mm/s, which corresponds to a nominal strain rate, $\dot{\varepsilon}$, of 0.141 s^{-1} with a gauge length of 16 mm by Equation (3.1).

$$\dot{\varepsilon} = \frac{v(t)}{L_0} \tag{3.1}$$

where $v(t)$ is the displacement velocity of the specimen and L_0 is the initial gauge length. Material parameters were taken from Westermann et al. [27] for T4 and from Westermann et al. [28] for T6 and T7. These parameters are detailed in Table 3.2 and were used in simulations to estimate the external force required to reach the different strain levels for both tension and compression. These material parameters were inserted into a material model in Abaqus in accordance with the Abaqus Theory Guide [30] and its formulas. An isotropic hardening model was inserted as a plastic material with isotropic hardening and tabulated values for the equivalent stress, σ_{eq}, and the equivalent plastic strain, p.

In compression a tensile test can buckle when subjected to significant applied force. The bucking phenomenon was analysed in Abaqus, and Figure 3.5 shows two buckling modes for the tensile test. Figure 3.5a shows the primary buckling mode of the tensile test as it was simulated with no sideways constraints at the top cross section, while Figure 3.5b shows the primary buckling mode when the top section was clamped. In the sideways free simulation, buckling was observed to initiate at approximatly 6 % strain for all tempers, while for the

(a) Top view

(b) Side view with cut plane through center line
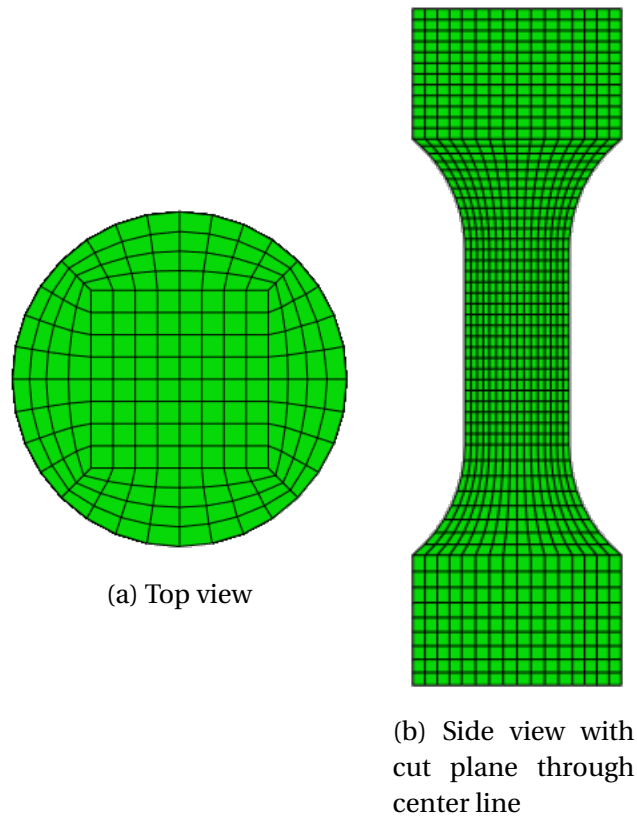
Figure 3.4: Mesh of the tensile test

Temper	σ_0 [MPa]	Q_{R1} [MPa]	C_{R1}	Q_{R2} [MPa]	C_{R2}
T4	66.26	62.00	32.36	126.46	4.21
T6	175.00	64.30	24.00	115.50	1.27
T7	193.40	42.30	35.50	77.10	0.87

Table 3.2: Material parameters for the simulated tensile test taken from Westermann et al. [27] and [28]

clamped simulation, the tensile test does not buckle at all. As the real constraints will be something in between the two, bucking is assumed to be initiated at a strain level higher than the proposed stopping criterion of 6 %. The longitudinal strain level, current applied force and diameter for each of the tempers are given in Table 3.3.

3.2.2   Experimental Setup

The tests were performed at the Department of Structural Engineering at NTNU in an Instron 5985 test machine with a 250 kN loading cell. An AEROEL XLS 13XY laser micrometer was used to continuously measure the current diameter. The full rig setup is shown in Figure 3.6a with annotations for the components described here. The rig was adjusted along the

Temper	Loading sequence	No.	Load reversal values		
			ε_l	F [N]	D [mm]
T4	Tension - compression	1	+0.005	935.68	3.99074
		2	+0.010	1060.47	3.98087
		3	+0.020	1265.32	3.96119
		4	+0.040	1541.88	3.92201
		5	+0.060	1705.64	3.88314
	Compression - tension	1	-0.005	-943.93	4.00828
		2	-0.010	-1080.58	4.01825
		3	-0.020	-1316.64	4.03827
		4	-0.040	-1669.32	4.07954
		5	-0.060	-1928.43	4.12037
T6	Tension - compression	1	+0.005	2224.48	3.99174
		2	+0.010	2299.97	3.98184
		3	+0.020	2427.41	3.96209
		4	+0.040	2604.46	3.92285
		5	+0.060	2708.68	3.88394
	Compression - tension	1	-0.005	-2241.24	4.00928
		2	-0.010	-2338.02	4.01825
		3	-0.020	-2515.26	4.03827
		4	-0.040	-2806.17	4.07868
		5	-0.060	-3028.66	4.11954
T7	Tension - compression	1	+0.005	2445.49	3.99191
		2	+0.010	2510.70	3.98200
		3	+0.020	2607.12	3.96223
		4	+0.040	2710.93	3.92293
		5	+0.060	2749.09	3.88397
	Compression - tension	1	-0.005	-2463.64	4.00811
		2	-0.010	-2550.95	4.01809
		3	-0.020	-2698.75	4.03813
		4	-0.040	-2915.78	4.07859
		5	-0.060	-3064.21	4.11952

Table 3.3: Load reversal values for tensile tests in all tempers and loading sequences

(b) Sideways clamped

(a) Sideways free
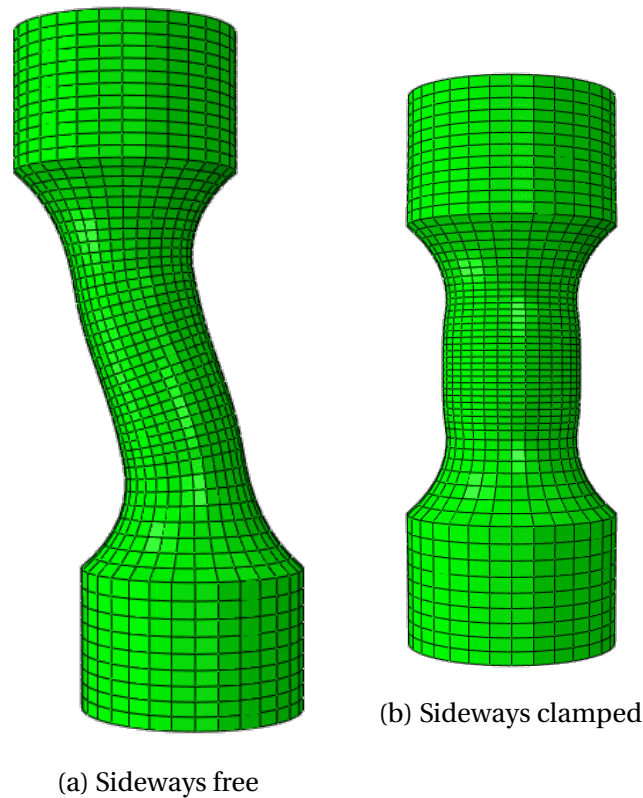
Figure 3.5: Buckling modes

vertical gauge length of the specimen during testing, to always measure the minimal diameter and thus the most critical. This diameter, together with the force from the test machine, were outputted at a rate of 10 Hz. Figure 3.6b shows a tensile test under testing where the orthogonal lasers can be seen measuring the diameter.

During the tensile test for T6 compression-tension no. 5, i.e. $\varepsilon_l = 6\%$ at the load reversal point, two minimal diameters were found on either side of the midpoint along the gauge length. The diameter with the slightly lesser value was thought to be the localization section. During the load reversal the two minimum diameter sections were inspected and it was found that the other diameter was the minimal and thus the most strained section. This will likely cause irregularities in the results for this specific test. The rate of displacement during the tests was set to 0.25 mm/ min due to the early load reversal point of the tests with longitudinal strain of 0.5 %, which corresponds to a reduction of the diameter of less than a quarter of a percent as seen in Table 3.2. To get consistency between the data, this displacement rate was used for all of the tests which, by Equation 3.1, gives a nominal strain rate of $2.6 \cdot 10^{-4} \, \text{s}^{-1}$. The displacement rate is significantly slower than that of the simulated Abaqus model. This can be a source of inertia forces in the simulation, but by analysing the simulated model with an energy check it was concluded that the inertia forces were insignificant for this model, as the kinematic energy was lower than one percent of the internal forces [31].

(a) Full rig setup. 1 - Loading cell connected to the bridge. 2 - Laser micrometer. 3 - Diameter display. 4 - Wheel for adjusting the laser position
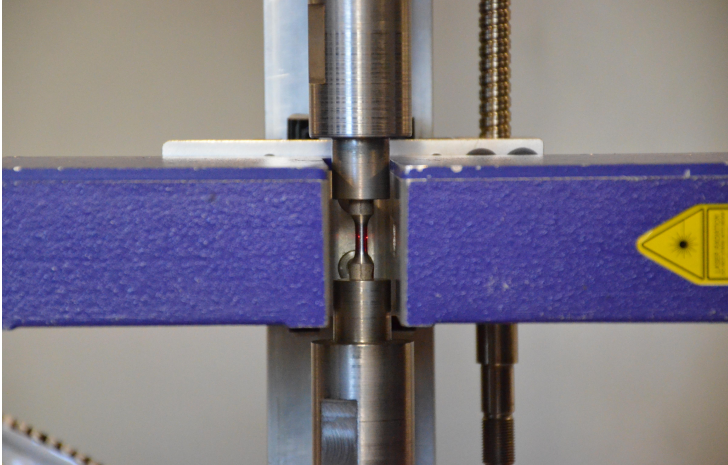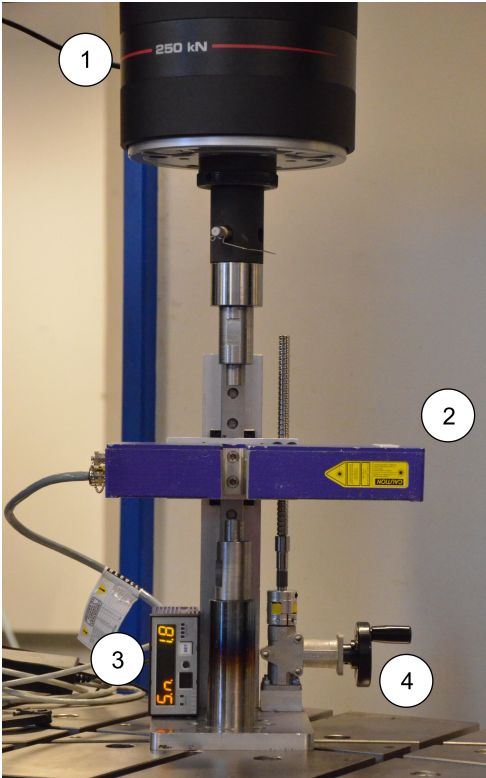
(b) Closeup of a tensile test specimen during testing

Figure 3.6: Tensile test experimental rig setup
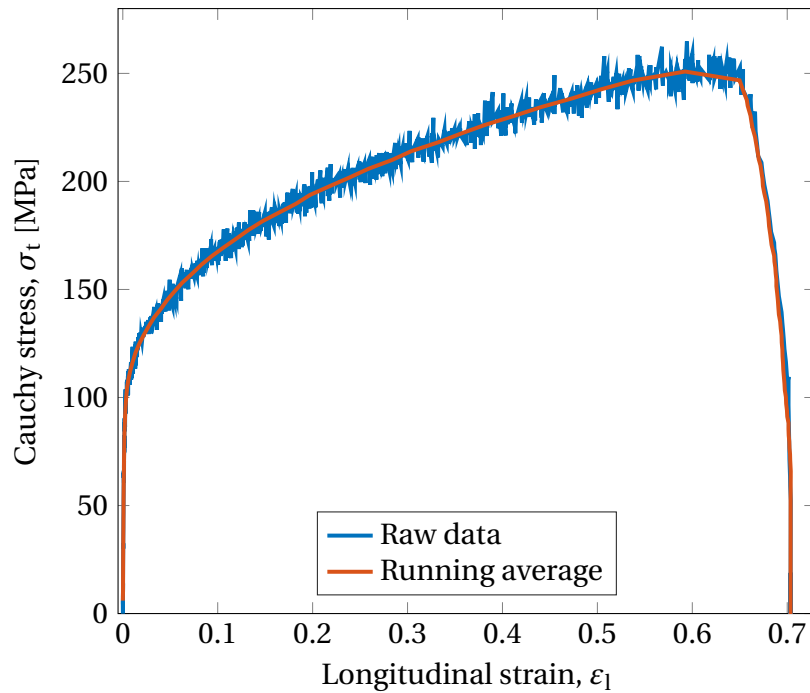
Figure 3.7: Plot comparing raw data and running average

3.2.3   Experimental Results

The raw data from the tensile tests, consisting of measured force and diameters in two per-
pendicular directions, were provided by the laser connected to the rig. The connection that
provided the force data used a signal amplifier causing amplified fluctuations. In most of the
provided plots in this thesis the data is therefore plotted as a running average, to ease the
comparison between the graphs. Figure 3.7 depicts this difference between the raw data and
the running average, highlighting the fluctuations, for the first T4 tension tensile test. Fig-
ure 3.8 shows the raw force data given by the Instron test machine and the amplified force
data from the laser micrometer. From this it becomes evident that it was the force data that
caused the fluctuations seen in Figure 3.7 from the Cauchy stress and not the Portevin-Le
Chatelier (PLC) effect [32], i.e. serrated yielding, which tend to cause the strain to have a
jerky and uneven curve. It is important to note that for the calculations detailed in Chapter
4 the raw data is used, not the running average.

The experimental results are presented for each temper and each of the different tensile test
types: tension, tension-compression, and compression-tension in Figures 3.9, 3.10 and 3.11.
The sub-figures are plots depicting each of the tensile test types, along with a detailed plot
for the compression-tension emphasising the differences in yield stress and the load reversal
points. For temper T4 the results show substantial work hardening in the pure tension plot.
Some difference in the yield stresses as well as tendencies to the Bauschinger effect can be
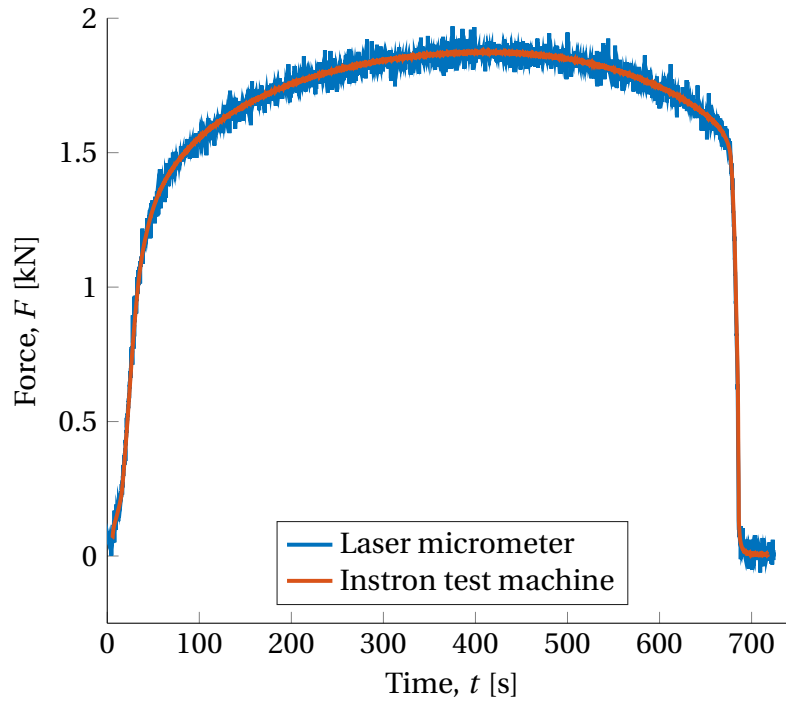
Figure 3.8: Plot comparing raw force data from laser micrometer and Instron test machine

seen in the different graphs of Figure 3.9. In the results for the T6 temper a higher yield stress can be observed as well as a steeper slope when the material work hardens, but lower fracture strain than temper T4. The individual difference in yield stresses can be seen for T6 as well. The reader should take note of T6 compression-tension tensile test no. 5, where the longitudinal strain around zero stress, i.e. during load reversal, is seen to decrease. This is due to the diameter irregularities described in the last paragraph of Section 3.2.2. For the final temper, T7, slightly lower yield stresses as well as a flatter slope when the material work hardens compared to T6 can be observed for the pure tension tensile tests. For T7 the yield stresses are seen to differ much less among the individual tensile test than for the other two, except for the two tests in pure tension.

(a) Pure tension

(b) Tension-Compression

(c) Compression-Tension

(d) Compression-Tension detailed
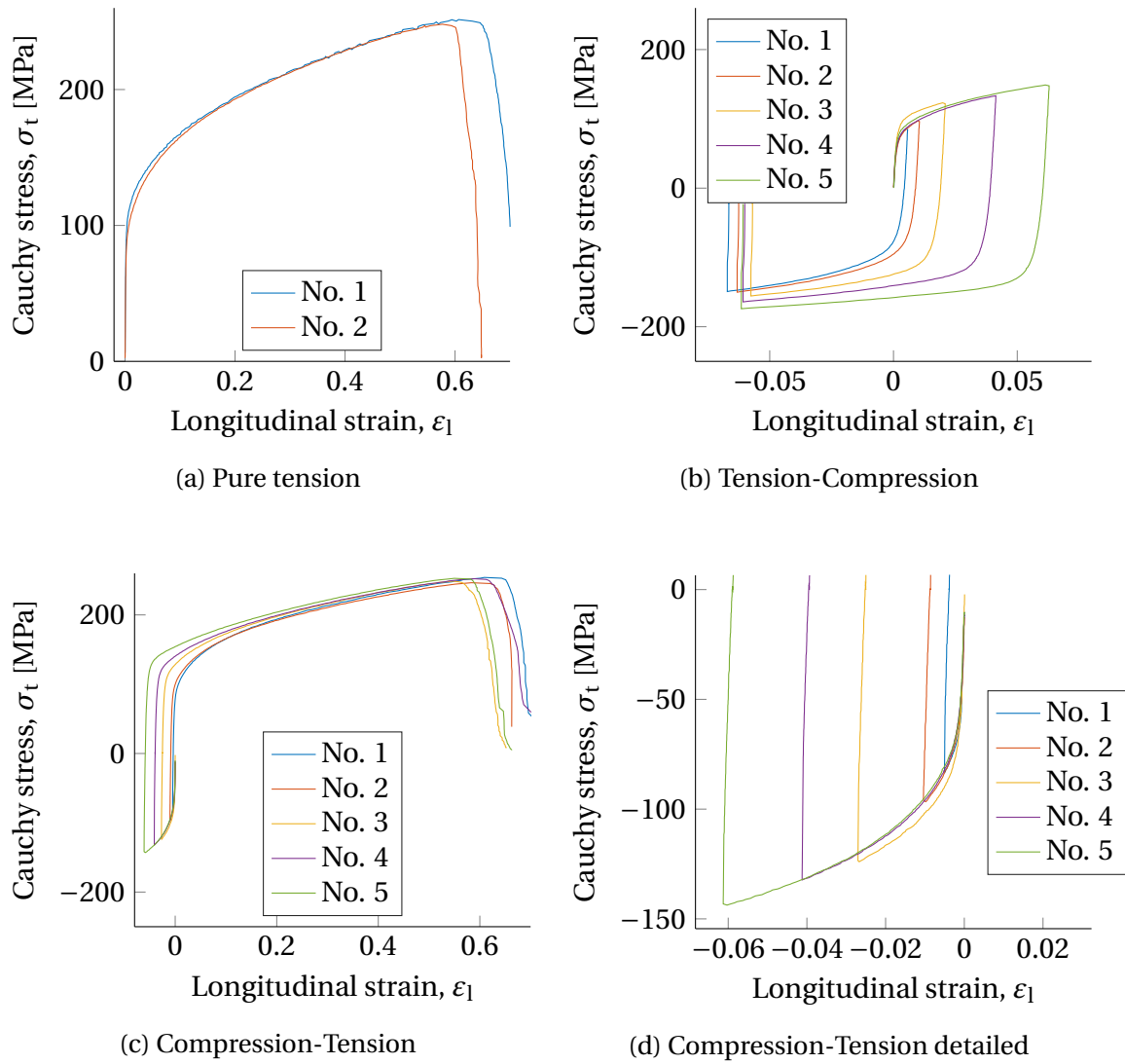
Figure 3.9: Tensile test results for temper T4
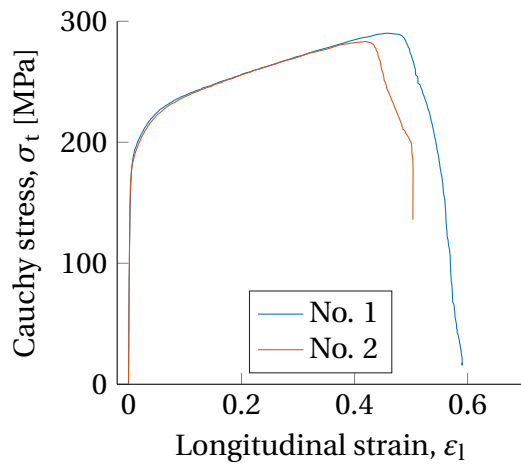
(a) Pure tension
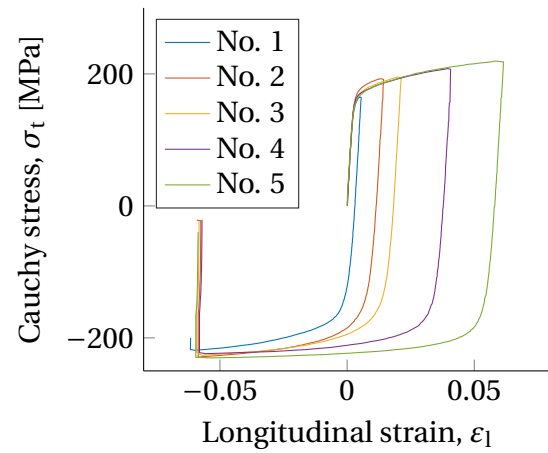
(b) Tension-compression
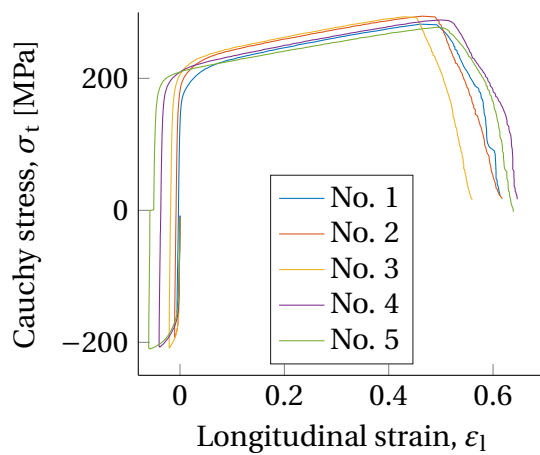
(c) Compression-tension
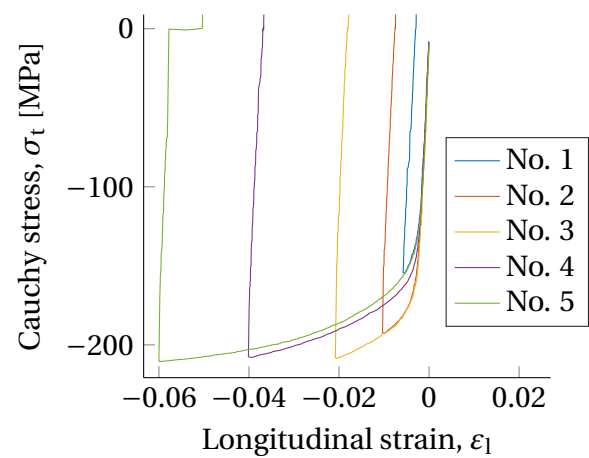
(d) Compression-tension detailed

Figure 3.10: Tensile test results for temper T6

(a) Pure tension

(b) Tension-compression

(c) Compression-tension

(d) Compression-tension detailed
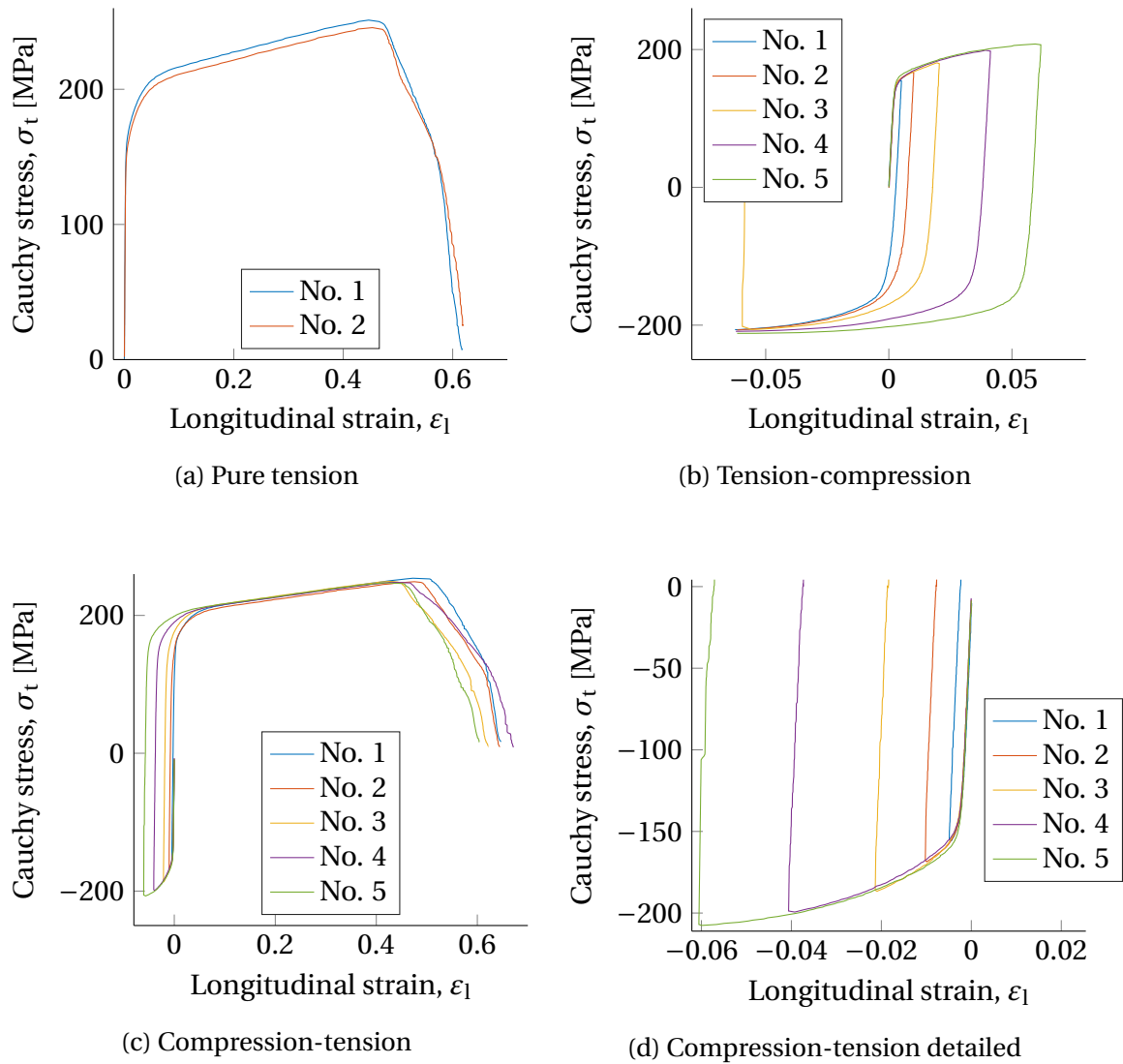
Figure 3.11: Tensile test results for temper T7

4 | Material Processing

As material mechanics are an important part of this thesis and due to unexpected experimental data from the laboratory material tests, this chapter is included to provide valuable insight into the methods used to process the experimental data. A section on material validation is included at the end of this chapter to validate the methods used to obtain the material parameters for an Abaqus simulation. All the following material processing and calculations were carried out in MATLAB [33].

4.1 Experimental Data

The force and diameters were imported from the experimental data for the tensile tests. The Cauchy's stress, longitudinal strain and plastic strain were calculated from these using Equations (2.1), (2.9) and (2.7), respectively. The equivalent stress, σ_{eq}, and equivalent plastic strain, p, were calculated from Equation (2.10) and (2.18). The reader should take note that the equivalent plastic strain is an accumulated strain measure. These two stress and strain measures were used in most of the material parameter calculations. Data after tensile failure and after final unloading were removed to enable curve fitting to the material models described in the following sections, based on theory in Chapter 2.

As previously stated, during the material tests the laser was adjusted to measure the minimal value of the diameter, which caused spikes in the diameter during adjustment. This anomaly in the data was refined by taking advantage of the fact that as long as the direction of the force is the same, the diameter should be strictly increasing or decreasing as a function of time. In tension this would be expressed as

$$A_{l+1} = min(A_l, A_{l+1}) \tag{4.1}$$

where l is the index of the current element in the list. The same equation was used for compression, where the list was traversed backwards from the end.

4.1.1   Discussion

From the experimental results in Section 3.2.3 it can be seen that the tensile tests showed considerable variation in their material behavior. In an attempt to identify this variation, the load sequence and type, i.e. tension-compression and compression-tension, were evaluated. Figure 4.1 shows a representative selection of different load reversal tests for T4 and T6. These plots show an abnormal amount of dispersion in the material data with results differing more than 20 MPa for the two load sequences at a given longitudinal strain. For all these plots a significant dispersion in the yield stress can be seen. However, this difference in yield stress does not explain the behavior seen in Figure 4.1b, as the tension-compression curve is higher for the first half cycle, but is almost identical to the compression-tension curve for the second half cycle. Notable difference in the work hardening can also be seen in the first half cycle for Figure 4.1c. No consistency was found in the hardening behavior for the load sequence or type and the reason for this is unknown, but might be due to the deviation in the heat treatment of the specimens from Westermann et al. [27].

As a conclusion of the experimental study it was found that the results from the tensile tests of this thesis did have significant dispersion of the yield stresses. In two occurrences the work hardening differs between the tension-compression and compression-tension load sequences. However, as no consistency was found towards the load sequence affecting the work hardening, it was concluded that for the tensile tests conducted in this thesis the load sequence did not affect the work hardening of the material.

4.2   Material Parameters

This section will present and discuss the conceptual methods used to calculate these parameters. The first section contains methods concerning the yield stress and the second section will focus on the calculation of backstress material parameters for the kinematic hardening. The calculation of significant material parameters were, as previously stated, done in MAT-LAB [33] and the complete code is found in Appendix B.

(a) T4 - 6% longitudinal strain

(b) T6 - 0.5% longitudinal strain

(c) T6 - 2% longitudinal strain
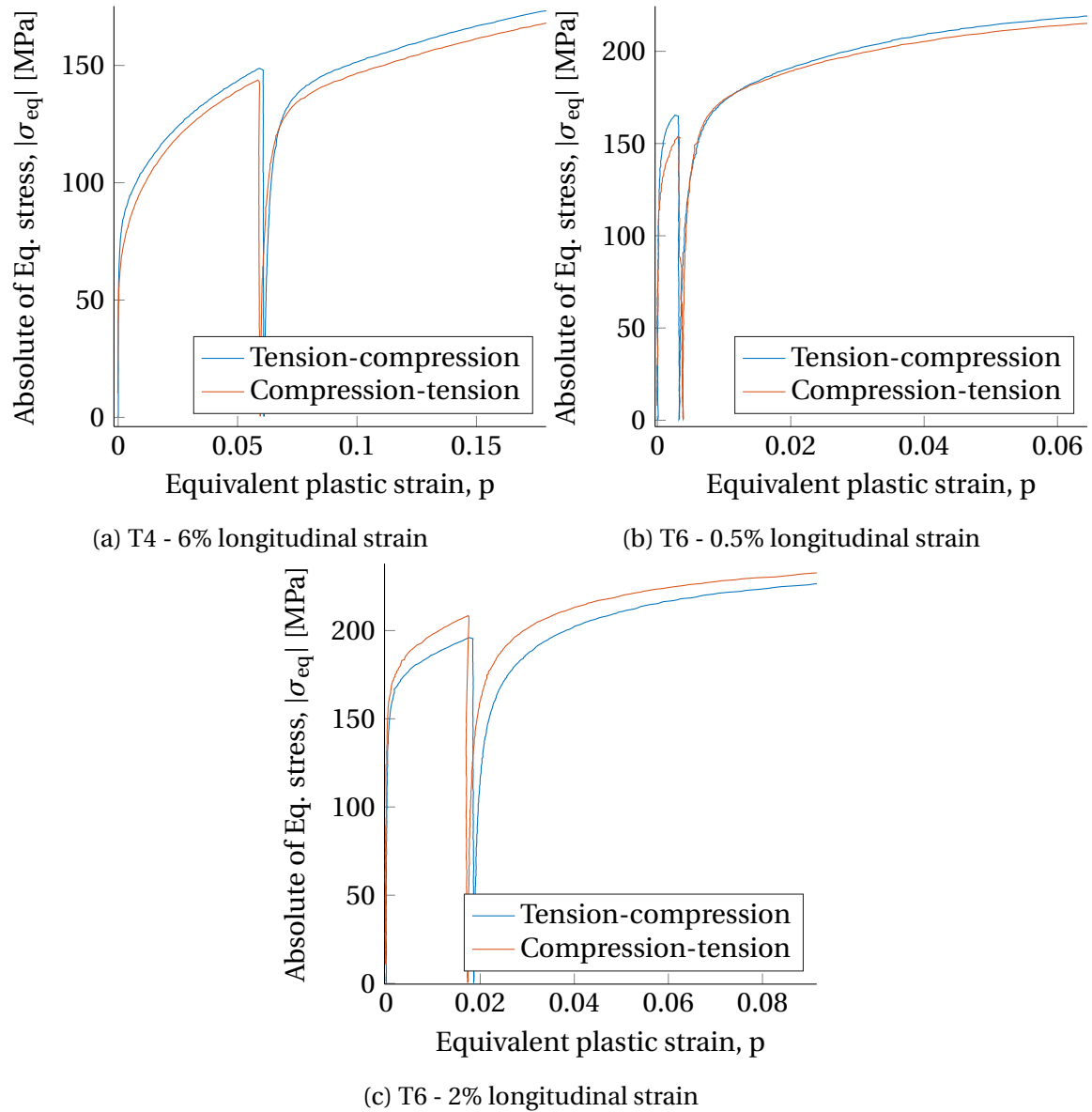
Figure 4.1: Comparison of the load sequence and type between load reversal tensile tests for the absolute value of the equivalent stress versus the equivalent plastic strain

Yield stress parameters	Method 1			Method 2			Method 3		
	T4	T6	T7	T4	T6	T7	T4	T6	T7
Average [MPa]	56.33	125.7	127.6	55.32	131.1	130.8	49.92	97.08	95.41
Standard deviation [MPa]	7.46	10.7	7.24	8.15	10.0	2.80	5.43	15.1	16.3

Table 4.1: Summarized yield stress values obtained with Method 1, 2 and 3 in Section 4.2.1

4.2.1   Yield Stress

As seen in the true stress-longitudinal strain plots presented in Figures 3.9, 3.10 and 3.11, the yield stresses show significant dispersion within each temper. To obtain the actual values of the yield stress for each tensile test, three methods were considered. Method 1 is a standard strain offset method, where the yield stress is set equal to the stress when the plastic strain is $\varepsilon^p = 0.025\%$.

Yield stress results from Method 2 were calculated by curve fitting the Voce Equation (4.2) to the individual material test data for the first half cycle.

$$\sigma_{eq} = \sigma_0 + \sum_{i=1}^{2} Q_i \left(1 - e^{-C_i p}\right) \tag{4.2}$$

where Q_i and C_i are material hardening parameters.

Method 3 was calculated by curve fitting the material equation from Voce and Armstrong-Frederick in a uniaxial stress state by inserting Equation (2.19) and (2.21) into (2.17). The data used in this curve fitting was the material data from the second half cycle and the ordinary data from the pure tension tests. All calculated results for the yield stresses are given in Appendix A.1 for each method and tensile test. The reader is encouraged to review the table as the values do have significant dispersion. Table 4.1 contains the average yield stress for each method and temper along with the standard deviation, to give a statistical picture of the actual dispersion. These summarized results reveal a high standard deviation in the yield stresses across all methods and tempers, except for temper T7 with Method 2. The results for Method 3 do not reflect the results shown in Figure 3.11 and appear to have severe difficulties curve fitting the load reversed tensile tests. This is suspected to be due to the complexity of the problem with nine material parameters to be determined. Method 3 has numerous occurrences of 45 MPa for T4 and 80 MPa for T6 and T7, as can be seen in Table A.1 in the appendix, which are the lower boundaries set for the curve fitting of each temper. Method 1 shows acceptable results overall, but due to the low standard deviation of T7 for Method 2, this method was used in all further calculations.

(a) All load reversal tensile tests   (b) Tension-compression no. 5
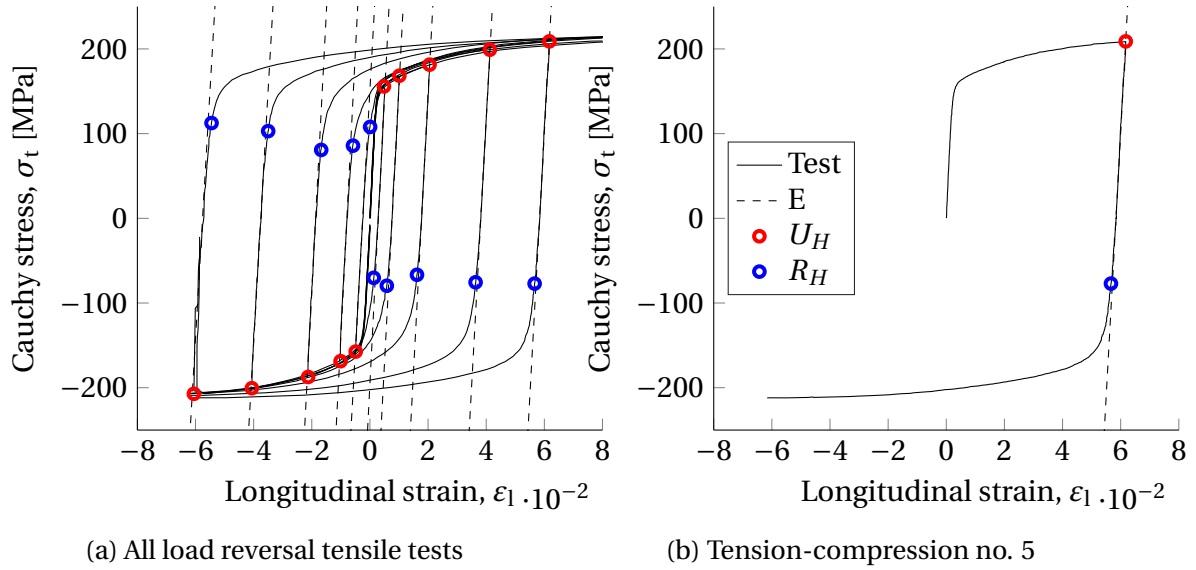
Figure 4.2: Conceptual plot for the backstress calculation Method A applied to temper T7

4.2.2 Backstress

The calculation of the backstress was done with two different methods. Method A follows the calculation methods described in Manes et al. [11], where the kinematic work hardening, σ_{KH}, and the isotropic work hardening, σ_{IH}, are calculated as

$$\sigma_{KH} = \frac{U_H + R_H}{2}, \qquad \sigma_{IH} = \frac{U_H - R_H}{2} \qquad (4.3)$$

Here U_H is defined as the ultimate stress before load reversal. R_H is defined as the yield point of the second half cycle and it is calculated at an offset to the longitudinal strain from the linear elastic unloading, which is set to $\varepsilon_{l,\text{off}} = 0.05\%$. The Young's modulus, E, was calculated by a linear regression from data between point U_H and the point of zero stress during load reversal. Figure 4.2 depicts these parameters for temper T7 for all tensile tests in Figure 4.2a, and tension-compression tensile test no. 5 is isolated in Figure 4.2b. Equation (4.3) yields one value per work hardening type for each of the material tests where the load was reversed. Using nonlinear regression on these isotropic and kinematic hardening values yields the material hardening parameters, σ_0, Q_R, C_R, Q_χ and C_χ, for the Voce Equation (4.2) and the backstress Equation (2.21). The resulting material hardening parameters are presented in Table 4.2. The kinematic nonlinear regression for each temper can be seen in Figure 4.3 for the tension-compression, compression-tension and both of them combined and the isotropic nonlinear regression can be seen in Figure 4.4. The 6% compression-tension tensile test was omitted in the regression for temper T6, due to irregularities caused by the diameter, as described in Section 3.2.2.

(a) T4

(b) T6. The rightmost compression-tension value is omitted in the regressions

(c) T7
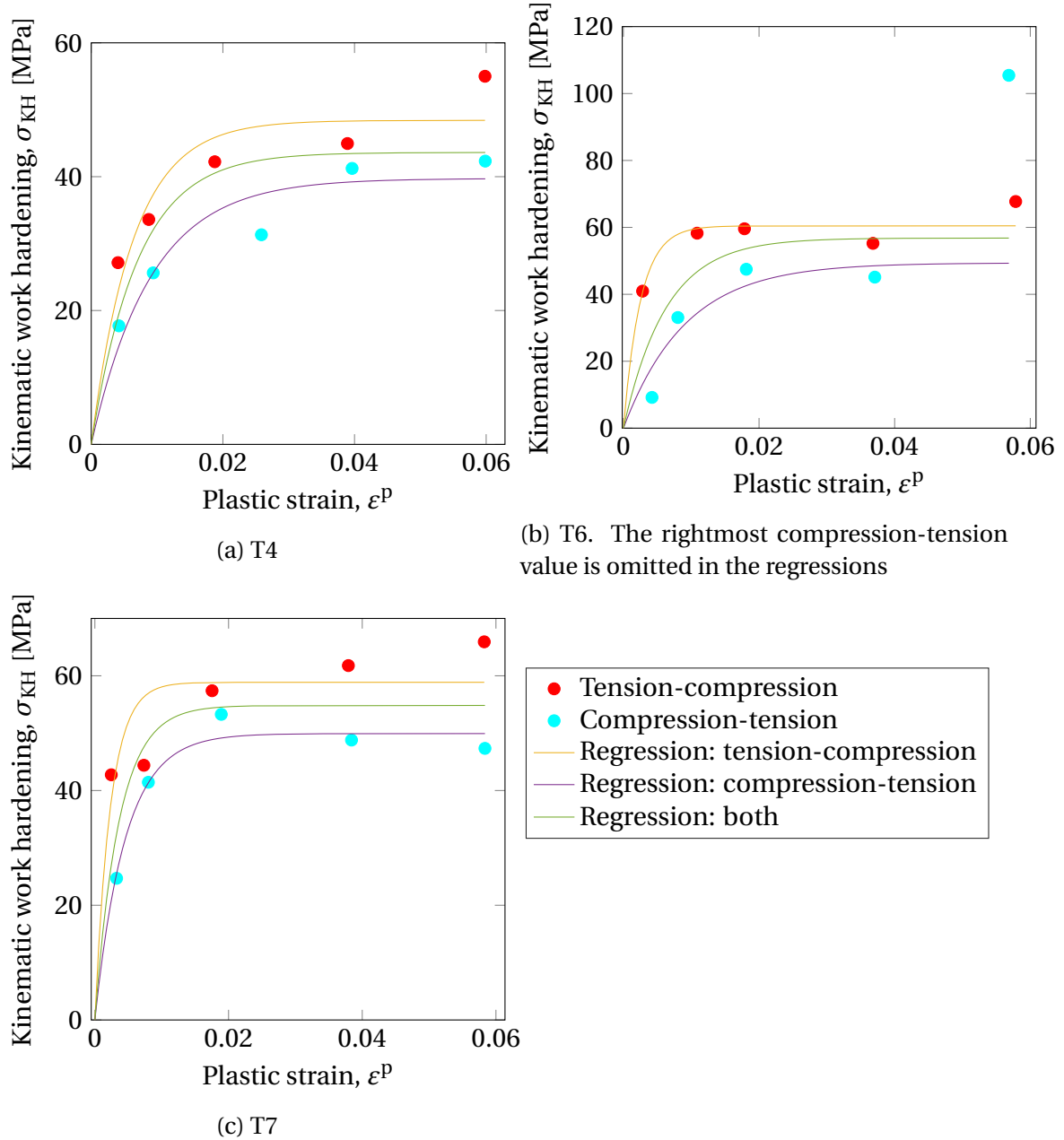
Figure 4.3: Plot of the backstress regression calculation result obtained with Method A

Parameters	Tension-compression			Compression-tension			Both		
	T4	T6	T7	T4	T6	T7	T4	T6	T7
σ_0 [MPa]	49.12	121.1	113.2	58.20	0.000	126.2	53.32	0.000	120.0
Q_R [MPa]	2668	1497	941.4	1913	89211	588.7	2317	99965	690.3
C_R	58.75	41.83	23.52	41.54	549.4	0.000	50.70	657.8	8.017
Q_χ [MPa]	48.42	60.46	58.86	39.73	49.38	49.93	43.62	56.81	54.83
C_χ	156.5	395.7	428.7	110.0	109.4	220.2	141.1	159.2	276.2

Table 4.2: Combined isotropic-kinematic hardening parameters for backstress calculation Method A

(a) T4

(b) T6. The rightmost compression-tension value is omitted in the regressions

(c) T7
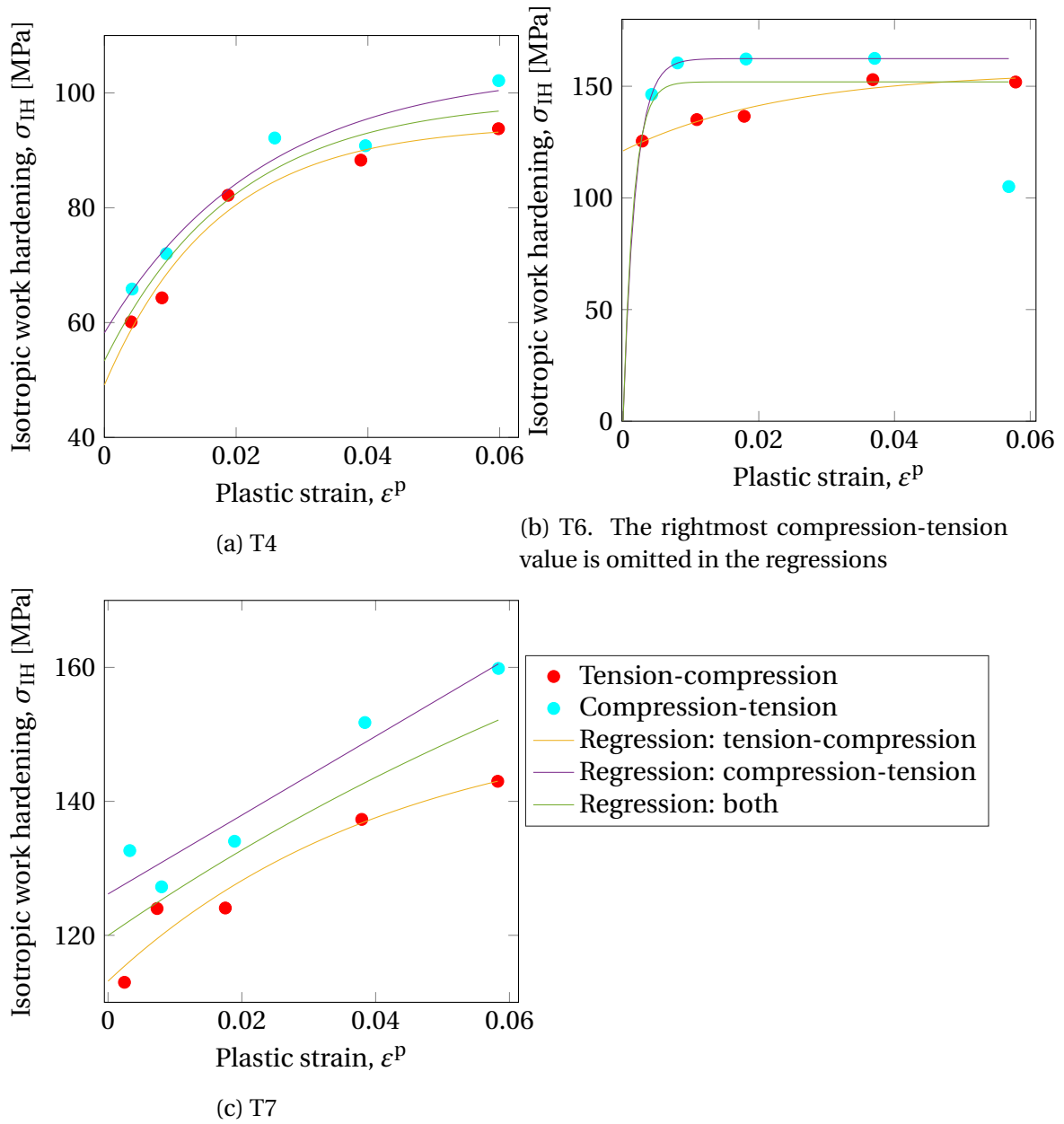
Figure 4.4: Plot of the isotropic regression calculation result obtained with Method A

(a) Yield stress normalization process   (b) Material parameter estimation process
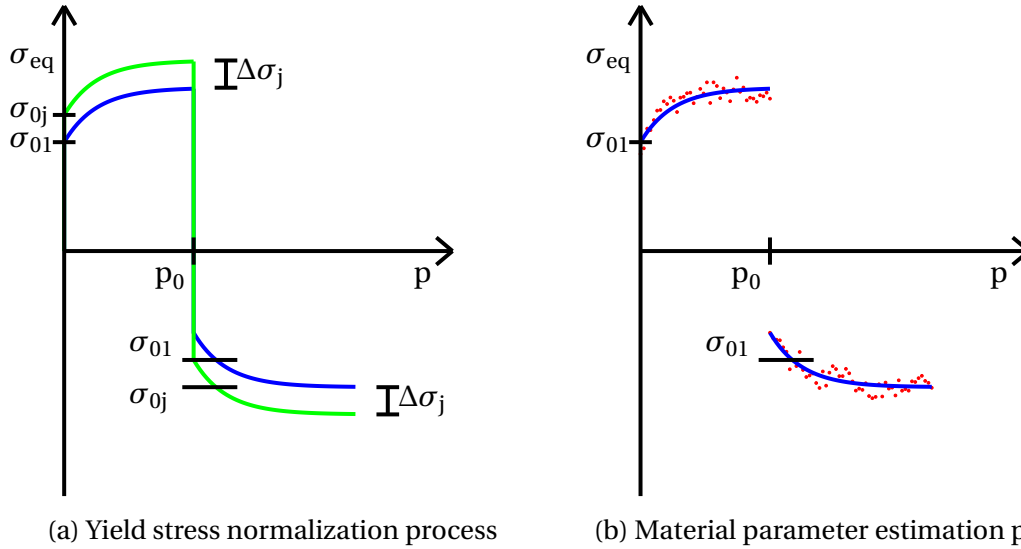
Figure 4.5: Qualitative plot of the normalization and estimation process for the backstress calculation Method B

Due to the wide dispersion in the yield stress for the individual tensile tests, the Voce equation was manipulated by a stress differential, $\Delta\sigma_j$, to normalize the individual differences and forcing the data to a specific yield stress for all tensile tests. Figure 4.5a illustrates this yield stress normalization concept as the green graph will be normalized to the blue graph. The individual stress differential is defined as

$$\Delta\sigma_j = \sigma_{01} - \sigma_{0j} \tag{4.4}$$

where the index j is the current tensile test and σ_{01} is the yield stress of the first pure tension test, which was used as a reference. Inserted into the Voce Equation (4.2) this yields

$$\sigma_{eq} = \sigma_{01} - \Delta\sigma_j + \sum_{i=1}^{3} Q_i(1 - e^{-C_i p}) \tag{4.5}$$

This Voce equation gives the total work hardening with a normalized yield stress.

Method B was initially supposed to curve fit tensile tests within each temper with two Voce terms and two Armstrong-Frederick terms, but considering the difficulty obtaining good estimates for the yield stress it was desirable to use a method with less complexity. Method B was therefore taken from Tarigopula et al. [10], as this method involves an initial curve fitting to a three term Voce Equation (4.5), and then assigning isotropic and kinematic material parameters based on the initial fit. This reduced-parameters method proved advantageous considering the complexity of the problem.

Temper	σ_0 [MPa]	Q_1 [MPa]	C_1	Q_2 [MPa]	C_2	Q_3 [MPa]	C_3	η_1	η_2	η_3
T4	55.32	31.09	580.6	24.27	33.98	103.0	4.56	0.973	0.133	0
T6	131.1	36.07	859.5	46.46	37.17	52.62	3.11	0.700	0.461	0
T7	130.8	21.14	1192	53.83	43.65	81.35	0.607	0.440	0.622	0

Table 4.3: Combined isotropic-kinematic hardening parameters for the backstress calculation Method B

To obtain individual material parameters for the isotropic and kinematic hardening components the following constraints were introduced

$$Q_{\chi_i} = \eta_i Q_i \, ; \qquad C_{\chi_i} = C_i \tag{4.6}$$

$$Q_{R_i} = (1 - \eta_i) Q_i \, ; \qquad C_{R_i} = C_i \tag{4.7}$$

where η_i is a combined hardening constraint coefficient. Inserting these constraints into the isotropic and kinematic material hardening equations (2.19) and (2.21) yields

$$R_i = Q_{R_i} \left(1 - e^{-C_{R_i} p}\right) = (1 - \eta_i) Q_i \left(1 - e^{-C_i p}\right) \tag{4.8}$$

$$\chi_i = \vartheta Q_{\chi_i} + \left[\chi_{0i} - \vartheta Q_{\chi_i}\right] e^{-C_{\chi_i}(p - p_0)} = \vartheta \eta_i Q_i + \left[\chi_{0i} - \vartheta \eta_i Q_i\right] e^{-C_i(p - p_0)} \tag{4.9}$$

Using MATLAB's [33] nonlinear least squares solver yields an optimal set of material parameters, which described how the initial Voce equation parameters were partitioned into isotropic and kinematic hardening terms. If a combined hardening constraint coefficient from Equations (4.6) and (4.7), η_i, is equal to one, the term will be fully kinematic, and if it is zero it will be fully isotropic.

The initial material hardening parameters, Q_i and C_i, were sorted based on the values of the latter ranging from maximal to minimal for increasing indices. This arrangement was done so that the third term of the constraint coefficients could be forced to zero, $\eta_3 = 0$, for all tempers and load sequences. The motivation for doing so was that the kinematic hardening of a metallic material tends to exert its work hardening capabilities and saturate at significant lower strains than the isotropic hardening, which will still work harden the material up to large strains [34, 35]. By letting the minimal value of the material parameter, C_3, be a fully isotropic hardening term, a more realistic work hardening was hoped to be achieved.

The material parameters presented in Table 4.3 are optimal values based on all load reversed tensile tests for each temper. The conceptual method for a material parameter estimation is depicted in Figure 4.5b, where the nonlinear regression, in blue, and the raw data points, in
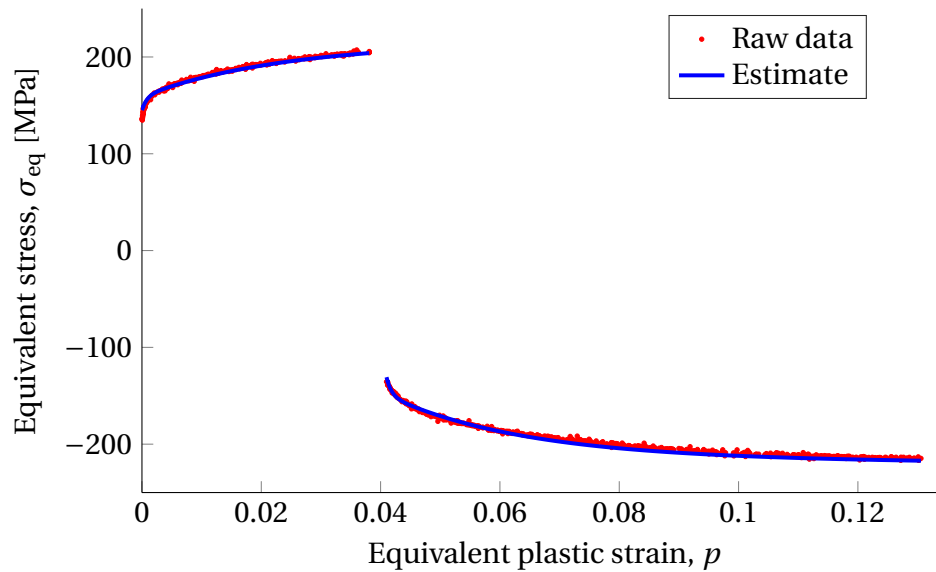
Figure 4.6: Plot of the raw data and the material parameter estimate by backstress calculation Method B for the tensile test T7 tension-compression no. 4

red are shown. In this figure the valid range of the material hardening model is shown, i.e. the elastic regions are removed from the data. The actual estimated material parameters and the raw data for temper T7 tension-compression tensile test no. 4 is shown in Figure 4.6. This shows an accurate fit to the data. For all the individual tensile test estimation comparisons see Section A.2 of the appendix.

Figure 4.7 shows isotropic and kinematic hardening components of the combined material hardening model for the first pure tension tensile test of each temper. In accordance with the speculation about isotropic and kinematic contributions to the work hardening, the figure clearly shows the steep slope of the kinematic hardening contribution compared to the more gradual isotropic hardening. The reader should take note that the contribution from the kinematic hardening is more gradual as the temper number increases. This is in good agreement with material theory on the microscopic level, described in more detail by Zhao and Holmedal [3], Proudhon et al. [34] and Fribourg et al. [35].

Results from Method A were dissatisfactory, as can be seen by the nonlinear regressions to the isotropic work hardening, in Figure 4.4. It shows acceptable results for temper T4, but the results for T6 are fundamentally flawed as the yield stress was found to be zero for two of the regressions. The figure reveals somewhat flawed results for T7, as the tension-compression regression appears to be linear. The material hardening parameters shown in Table 4.2 emphasize this as some values can be seen to be zero, which was the lower boundary set for these regressions. Backstress calculation Method B appears to be the better calibration method, being more robust and accurate in its estimates. Method A is, however, a

(a) T4

(b) T6

(c) T7
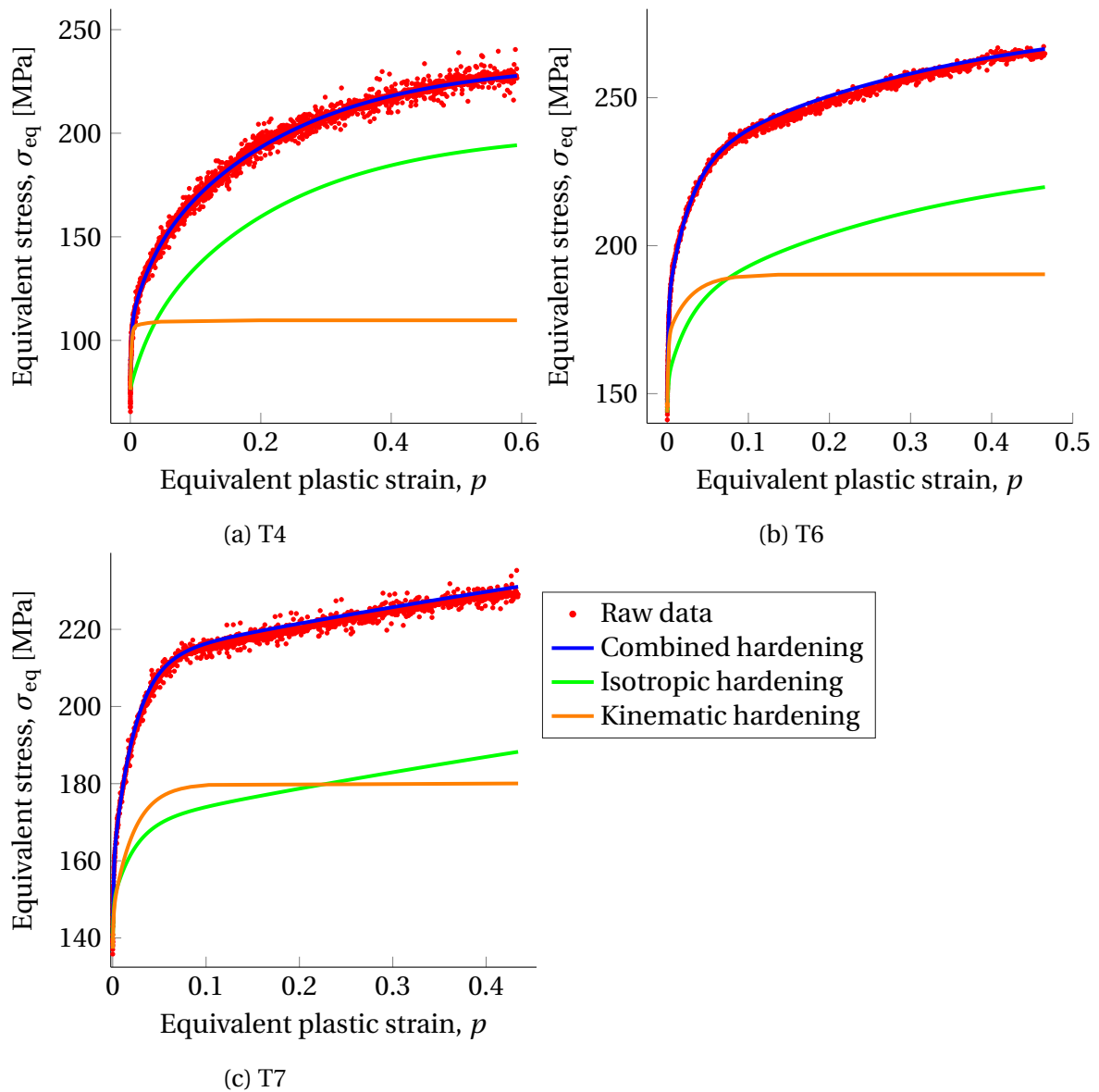
Figure 4.7: Plot of the raw data and the material parameter estimate by backstress calculation Method B for the first pure tension tensile test of each temper with isotropic and kinematic components of the combined material hardening model

simpler solution to implement and would be recommended if a higher number of tensile tests were conducted, as this would make the accuracy of this method statistically viable. If tensile test data are scarce, Method B is the preferred method to calculate both isotropic and kinematic material hardening parameters. This thesis will therefore use material parameters obtained with Method B, given in Table 4.3, for each temper. It is important to note that the isotropic material hardening model also uses these material parameters without the added constraints, i.e. $\eta_i = 0$.

4.2.3   Implementation of the Cockcroft-Latham Criterion

To implement a fracture criterion in Abaqus without the use of a user-subroutine, tabulated values of the equivalent plastic fracture strain, p_f, stress triaxiality, σ^*, and equivalent plastic strain rate, $\dot{p}$, are needed. The strain rate was set to zero as AA6060 can be considered strain rate insensitive [15]. The equivalent plastic fracture strain can be expressed as a function of the stress triaxiality, as will be shown in this section. The following paragraphs contains the calculation of the fracture parameter, W_c.

As stated in Section 2.3, β is defined ranging from -2 to 1. Equations (2.30), (2.32) and (2.33) are used to calculate the stress triaxiality, Lode parameter and Lode angle, respectively. In the general equation for the Cockcroft-Latham the first principle stress, σ_I, is used. The first principle stress can be related to the equivalent stress, σ_{eq}, with the stress triaxiality, σ^*, and Lode parameter, μ, as [36]

$$\sigma_I = \left(\sigma^* + \frac{3 - \mu}{3\sqrt{3 + \mu^2}} \right) \sigma_{eq} \tag{4.10}$$

In generalized tension, which was the stress state present in the uniaxial tensile tests, the second and third principal stresses are equal, i.e. $\sigma_{II} = \sigma_{III}$. Using this in Equation (2.31) for the Lode parameter, the following deduction can be made

$$\mu = \frac{2\sigma_{II} - \sigma_I - \sigma_{II}}{\sigma_I - \sigma_{II}} = \frac{\sigma_{II} - \sigma_I}{\sigma_I - \sigma_{II}} = -\frac{\sigma_I - \sigma_{II}}{\sigma_I - \sigma_{II}} = -1 \tag{4.11}$$

This equation is inserted into Equation (4.10) and the stress triaxiality was set to $\frac{1}{3}$ due to the uniaxial tension. This yields

$$\sigma_I = \left(\frac{1}{3} + \frac{3 - (-1)}{3\sqrt{3 + (-1)^2}} \right) \sigma_{eq} = \sigma_{eq} \tag{4.12}$$

It is important to note that this is only valid for a uniaxial tension stress state, i.e. before

Fracture parameter	Tempers		
	T4	T6	T7
p_f	0.5174	0.4020	0.4234
W_c [MPa]	89.35	93.68	89.97

Table 4.4: Cockcroft-Latham fracture parameters for all tempers

necking. Inserting this into the Cockcroft-Latham fracture criterion when fracture occurs, i.e. when the damage is equal to one, yields

$$\omega = \frac{1}{W_c} \int_0^{p_f} \sigma_{eq} \mathrm{d}p = 1, \quad W_c = \int_0^{p_f} \sigma_{eq} \mathrm{d}p \tag{4.13}$$

Using the Voce Equation (4.2) with three terms to calculate the equivalent stress yields the following expression for the fracture parameter.

$$W_c = \int_0^{p_f} \left[\sigma_0 + \sum_{i=1}^{3} Q_i \left(1 - e^{-C_i p} \right) \right] \mathrm{d}p \tag{4.14}$$

The equivalent plastic fracture strain, p_f, was taken as the minimum equivalent plastic strain at fracture of the two pure tension tensile tests for each temper. This and the calculated fracture parameter for each temper is given in Table 4.4.

With all fracture parameters calculated in the uniaxial tension stress state, an equivalent plastic fracture strain can be calculated as a function of the stress triaxiality and the Lode parameter. This is achieved by taking the expression for the damage criterion when the damage is equal to one and solving it for the equivalent plastic fracture strain. The assumption of plane stress and a constant incremental strain ratio, results in the stress triaxiality and Lode parameter becoming constants.

$$\omega = 1 = \frac{1}{W_c} \int_0^{p_f} \left(\sigma^* + \frac{3 - \mu}{3\sqrt{3 + \mu^2}} \right) \left[\sigma_0 + \sum_{i=1}^{3} Q_i \left(1 - e^{-C_i p} \right) \right] \mathrm{d}p \tag{4.15}$$

$$\frac{W_c}{\left(\sigma^* + \frac{3 - \mu}{3\sqrt{3 + \mu^2}} \right)} = \int_0^{p_f} \left[\sigma_0 + \sum_{i=1}^{3} Q_i \left(1 - e^{-C_i p} \right) \right] \mathrm{d}p \tag{4.16}$$

Solving the integral and setting the equation equal to zero yields

$$-\frac{W_c}{\left(\sigma^* + \frac{3 - \mu}{3\sqrt{3 + \mu^2}} \right)} + \sigma_0 p_f + \sum_{i=1}^{3} Q_i \left(\frac{1 - e^{-C_i p_f}}{-C_i} + p_f \right) = 0 \tag{4.17}$$

The stress triaxiality takes values of $-\frac{1}{3} \leq \sigma^* < \frac{2}{3}$, calculated from Equation (2.30) with the incremental strain ratio having values of $-2 \leq \beta < 1$. Values for the Lode parameter is calculated from Equation (2.32). Solving Equation (4.17) for the equivalent plastic fracture strain yields all parameter values needed for a fracture criterion in Abaqus, i.e. σ^* and p_f.

4.2.4 Material Validation

This section aims to validate the isotropic and kinematic material hardening parameters provided in Section 4.2.2 by modeling a tensile test in Abaqus/Implicit [29] and simulating some of the tensile tests, namely those with 0.5% and 4% longitudinal strain at load reversal. The Abaqus model is explained in detail in Section 3.2.1 with the difference being that the material parameters used in this section were the calculated ones described in this chapter and the simulation includes load reversal. This simulation model also included the combined material hardening model. This hardening model was inserted as a plastic material with combined hardening and a parametric formulation with two backstress terms. The following material parameters were inserted: the yield stress, σ_0, the product of the two kinematic material hardening parameters, $Q_i C_i$, and the kinematic hardening parameter, C_i. A suboption was chosen to insert the isotropic hardening by choosing cyclic hardening and inserting the tabulated values of σ_{eq} and p for the isotropic part of the total work hardening.

Figure 4.8 shows some of the results from the material parameter validation for one tensile test for each temper. For all material parameter validation plots, the reader is referred to Section A.3 of the appendix. Figure 4.8a shows the material parameter validation for tensile test T4 compression-tension no. 4. This figure shows that the total work hardening is not properly reproduced by the material parameters. The reason for this is probably the significant dispersion of the experimental material data. Another possibility might be that it is due to a negative side-effect of the yield stress normalization process. When altering the yield stress for a specific test result the whole curve will be adjusted and therefore also affect the work hardening. Whether this is affecting the validation results is speculative. However, the kinematic hardening is well described for this temper, as all the graphs coincide after load reversal. The material parameter validation for tensile test T6 compression-tension no. 4 is shown in Figure 4.8b. It shows the same traits as the T4 tensile test, although these are toned down; the total difference in work hardening is smaller and the kinematic hardening is not as well described.

In Figure 4.8c it can be seen that the Abaqus simulation result is translated compared to the MATLAB estimate. This is probably due to the fact that the material parameters were

(a) T4 compression-tension no. 4

(b) T6 compression-tension no. 4

(c) T7 tension-compression no. 4
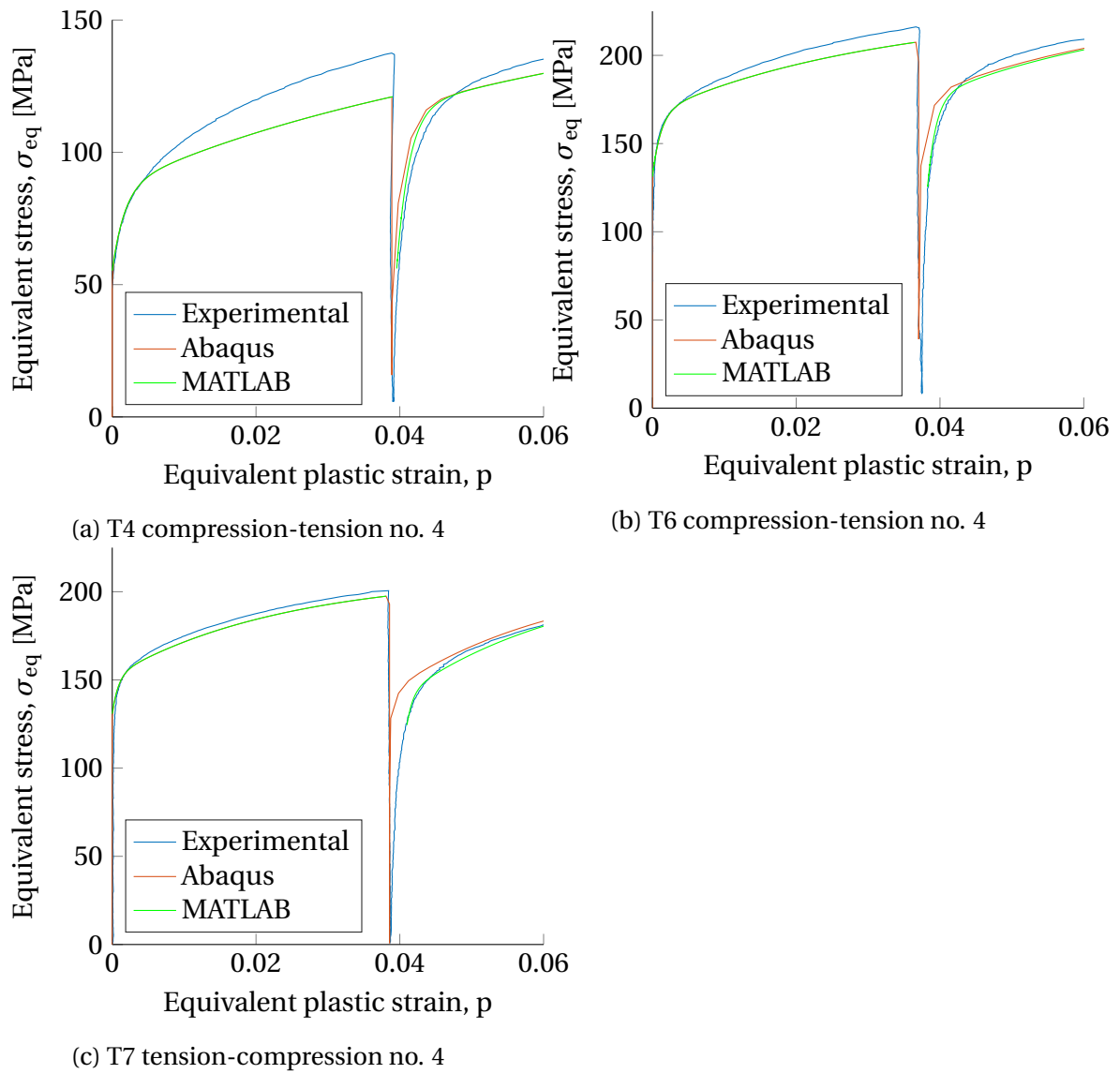
Figure 4.8: Validation of the combined isotropic-kinematic material hardening parameters

		Tempers		
Origin	Fracture parameters	T4	T6	T7
Calculated	W_c [MPa]	89.35	93.68	89.97
Inverse modeled	W_c [MPa]	95.16	103.88	102.69

Table 4.5: Comparison of calculated and inverse modeled values of the fracture parameter for all tempers

fit to an initial Voce equation. This locked the C_i-material parameters before the kinematic hardening was allocated and would therefore not be able to describe a material behavior of an early re-yielding and a rapidly increasing kinematic hardening, i.e. a large value of $C_{\chi i}$. This may lead to a smaller kinematic contribution than what is actually the case, which may in turn result in a reduced difference between the two hardening models. However, the translation causes limited strain differences, with an average of about 0.001 and a maximum of 0.002 in the material parameter validation plots where this anomaly was present.

An inverse modeling in Abaqus was performed to validate the fracture parameter, W_c, previously found by calculations described in Section 4.2.3. This was done by integrating the first principal stress, σ_I, over the equivalent plastic strain, p, both of which was taken from Abaqus for all tempers. As seen in Table 4.5, the inverse modeled values for the fracture parameter were higher than the calculated values. This is due to the fact that in the fracture criterion calculations presented in this thesis it was assumed that the first principle stress, σ_I, can be set equal to the equivalent stress, σ_{eq}, for a uniaxial stress state. This assumption is not valid after the necking of the specimen, where the first principle stress will be higher than the equivalent stress, and the inverse modeled fracture parameters will therefore be higher than the ones calculated. This means that the calculated values for the fracture parameter, W_c, are a conservative approximation, and will be used for the cases in this thesis.

5 | Case Studies

This chapter presents the numerical case studies performed in this thesis. For each case the following will be given: a short introduction, the numerical modeling procedures, the results and a discussion.

The case studies have been performed to evaluate the effect of including both isotropic and kinematic hardening in a material hardening model, as opposed to purely isotropic hardening. The cases given in this thesis are axial crushing of two aluminum profiles commonly used by Hydro Aluminium AS, forming limit diagram (FLD) for a metal sheet, impact loading on two stiffened plates and blast loading on a clamped plate. These cases have been simulated in Abaqus [29] with both isotropic and combined isotropic-kinematic material hardening models. All cases were modeled using S4R shell elements, since this is a versatile element and can be used for most purposes [37]. It offers reduced computational time compared to S4 due to its reduced integration. No strain dependent behavior were modeled, due to the indications of strain rate insensitivity for AA6060 with temper treatment by Chen et al. [15] and Figure 2.1. The isotropic material hardening model was modeled in Abaqus as described in Section 3.2.1 and the combined material hardening model as described in Section 4.2.4. The tabulated values inserted to Abaqus were calculated from the material parameters given in Table 4.3. η_1, η_2 and η_3 were set equal to zero for the purely isotropic model. Abaqus/Explicit was used for all cases except FLD, which used Abaqus/Standard.

5.1 Axial Crushing

Axial crushing of aluminum profiles can be used to simulate the behavior of a crash box in a vehicle during an impact. Important properties of a crash box include high energy absorption potential and high structural integrity, both of which are fundamental to ensure vehicle safety. In the paper by Hoang et al. [12], aluminium profiles of alloy AA6060, in tempers T6 and T7, were crushed experimentally and then simulated numerically. Following the meth-
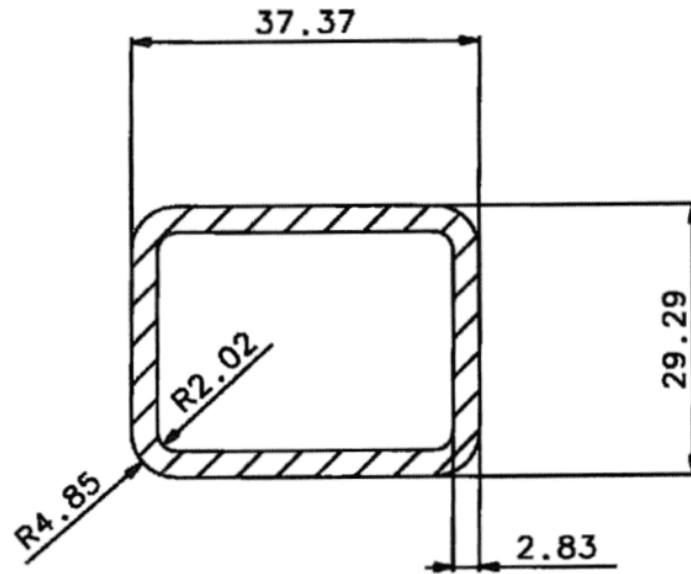
Figure 5.1: Geometry of the single chamber profile

ods of Hoang et al. [12], axial crushing of two aluminum profiles were simulated: a single chamber profile and a triple chamber profile. When crushing these kinds of profiles, the sides often tend to fold in a smooth way causing a build up in the crushing force when each fold is initiated and a decline when the fold is formed.

5.1.1   Modeling

The aluminum profiles were modeled in Abaqus from cross sectional drawings provided by Hydro. The geometries are shown in Figure 5.1 and 5.2 and the extruded lengths were 100 mm and 300 mm for the single and triple chamber profile, respectively. The radius of the corners in the triple chamber profile were set to 2 mm. The profiles were crushed by a plane analytical surface with a constant displacement rate of 10 m/s, to simulate a dynamic crushing. The Cockroft-Latham fracture criterion, as described in Section 2.3 and 4.2.3, was included due to the large strains commonly achieved in this kind of deformation. The simulation used a friction coefficient of 0.3, in accordance with Hoang et al. [12]. However, as opposed to Hoang et al. [12] where one analytical surface was modeled in each end of the profile, the lower part of the profiles in this thesis were clamped to trigger deformation in the free end. The profiles were clamped for the first 15 mm and 50 mm for the single and triple chamber profiles, respectively.
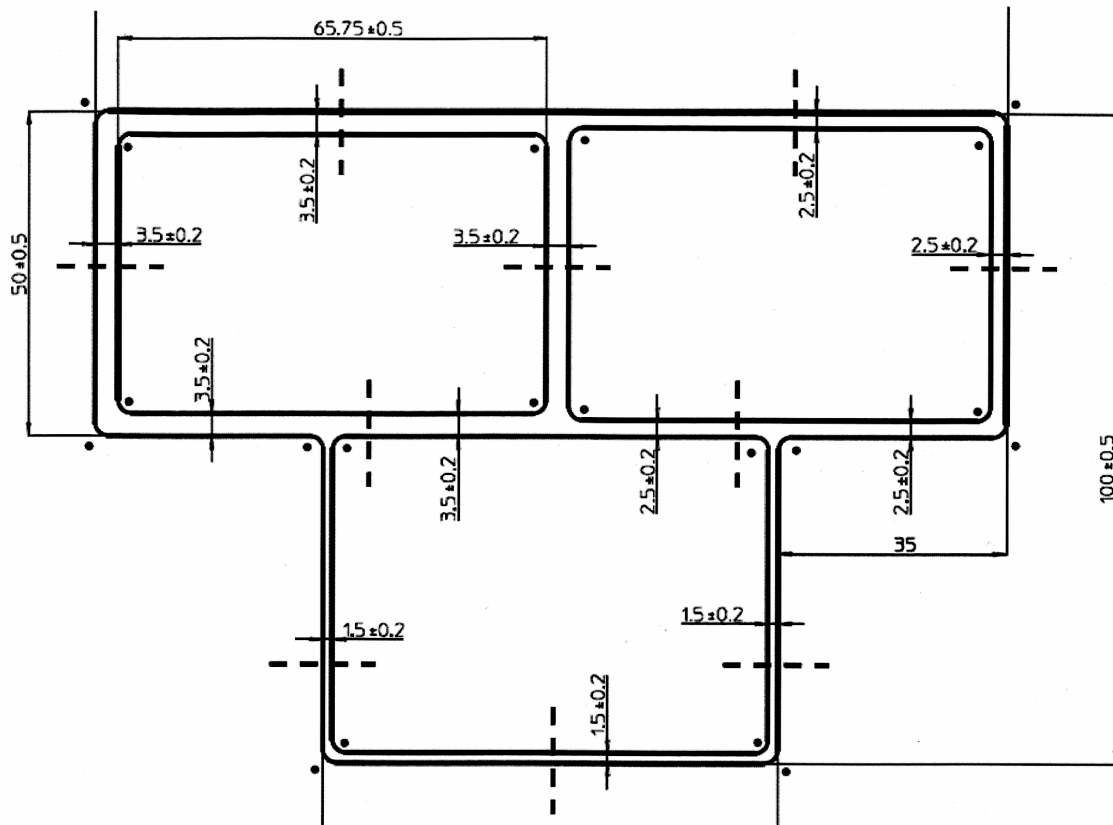
Figure 5.2: Geometry of the triple chamber profile

Imperfections were introduced to the single chamber profile using the first five eigenmodes, to initiate the same deformation pattern as seen in the experimental results of Hoang et al. [12]. Eigenmodes represent the various buckling modes of a system, and are ranked in order of energy required to initiate them, with the least amount of energy required for the first eigenmode. The model for the single chamber profile was meshed using 2 mm shell elements and the whole mesh is shown in Figure 5.3.

The triple chamber profile was modeled with zero, 5 and 20 eigenmodes to examine the effect of imperfections. The mesh was modeled with 4 mm shell elements, shown in Figure 5.4, to keep the computational time within reasonable limits while maintaining as much detail in the model as possible.

5.1.2   Single Chamber Profile

Results for the single chamber profile are presented and compared here. The comparison has emphasis on tempers and material hardening models. Plots of the crushing force versus displacement are provided to show the global response of the system. The included mean
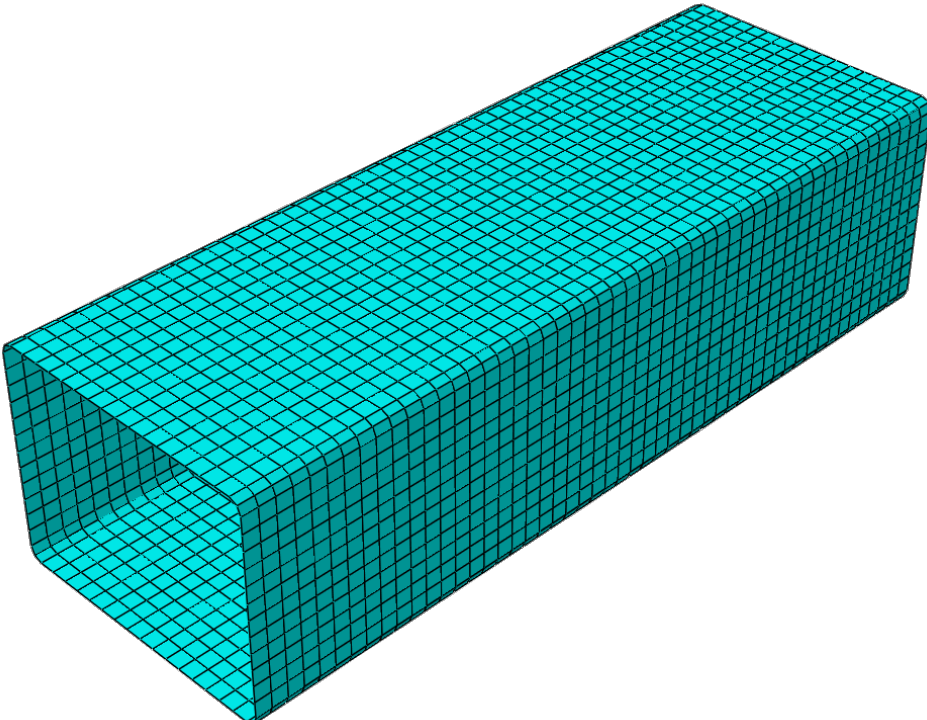
Figure 5.3: Mesh of the single chamber profile
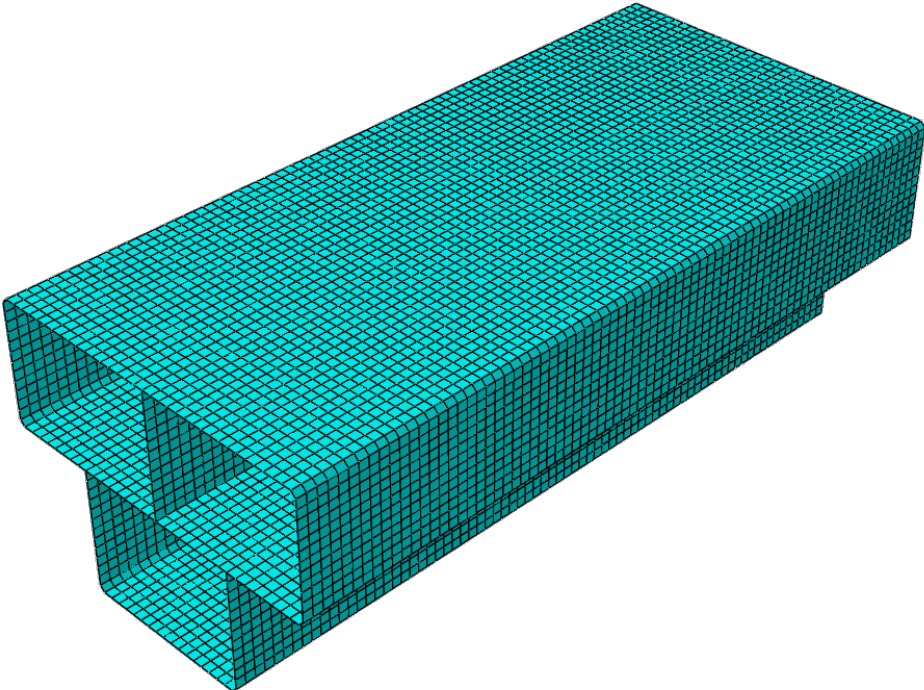
Figure 5.4: Mesh of the triple chamber profile

	Number of fractured elements	
Temper	Isotropic hardening	Combined hardening
T4	None	None
T6	2	2
T7	1	2

Table 5.1: Fractured elements in the single chamber profile

force versus displacement plots are a good measure for the amount of energy absorbed by the system. The mean force, F_m, is given by the following equation, taken from Seitzberger et al. [38]

$$F_m(u) = \frac{\int_0^u F(\tilde{u})d\tilde{u}}{u} \tag{5.1}$$

where u is the displacement and $\tilde{u}$ is the displacement integration variable. The equivalent plastic strain field of the final deformed shape, denoted PEEQ in the figures, is displayed in Figure 5.5 for T4 with combined hardening. This figure reveals that the profile has high strain concentrations in corners where folds from two adjacent sides meet. The final deformed shapes for the other simulations are shown in Figure A.9 in Section A.4.1 of the appendix. After thorough inspection of the simulation models, fracture was found in a few elements for some tempers, listed in Table 5.1. In Abaqus, fractured elements were deleted from the simulation model.

The force plots in Figures 5.6a, c and e show that T6 and T7 have a similar structural response, while T4 have a softer response. T6 and T7 also absorb more energy than T4, as shown in Figures 5.6b, d and f. From the force plots it can clearly be seen when each fold was initiated from the force build up, and these peaks have roughly the same characteristic shape as seen in Figure 5.7, taken from Hoang et al. [12].

As seen from the mean force plots, the simulations with the isotropic hardening model absorbes slightly more energy than the combined model for all tempers. No other significant difference can be seen between the hardening models on the global level for force or mean force versus displacement.

As Hoang et al. [12] had a geometrically different profile, their exact results were not expected to equal the plots in Figure 5.6. However, the material and two of the tempers coincide, as both use AA6060 T6 and T7. The overall shape of the curves are similar, but Figure 5.6 c seems to have a slightly steeper slope at the beginning of each peak than what is seen for T6
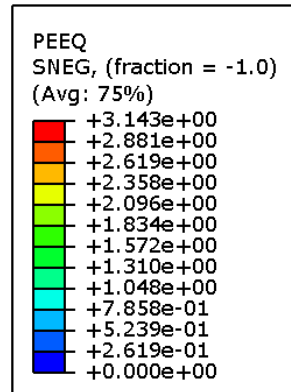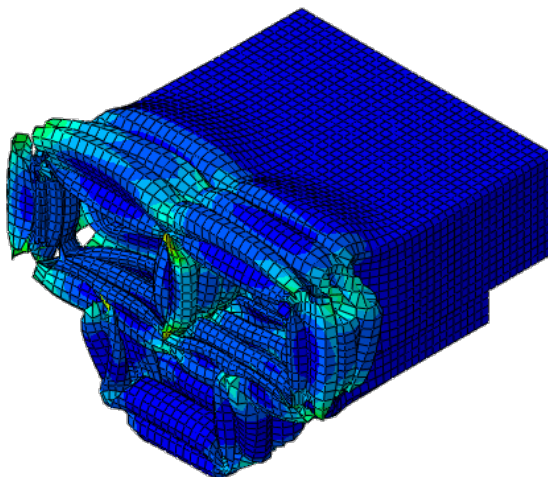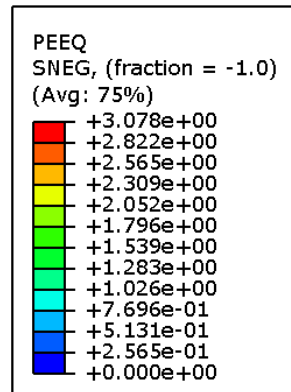
(a) T4

(b) Color scheme for T4

(c) T6

(d) Color scheme for T6

(e) T7
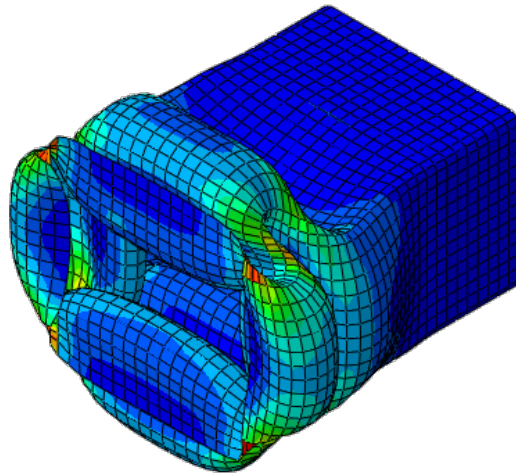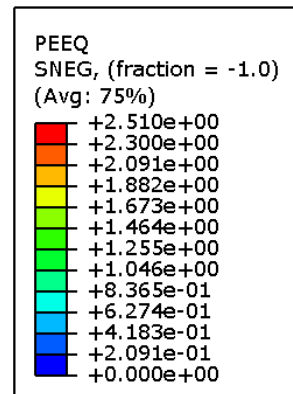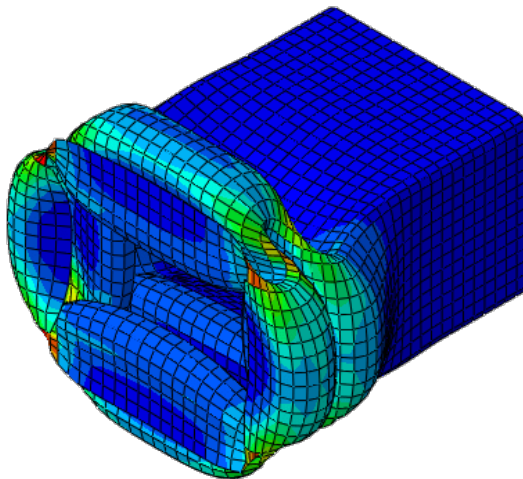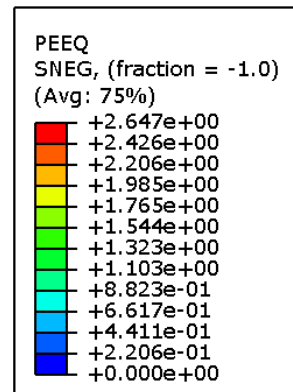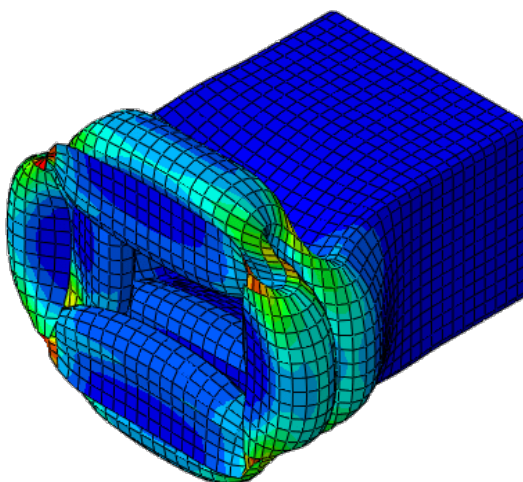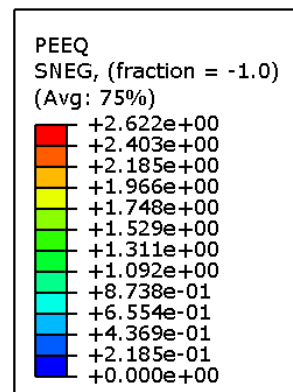
(f) Color scheme for T7

Figure 5.5: The equivalent plastic strain field for the final deformed state for the single chamber profile with combined hardening
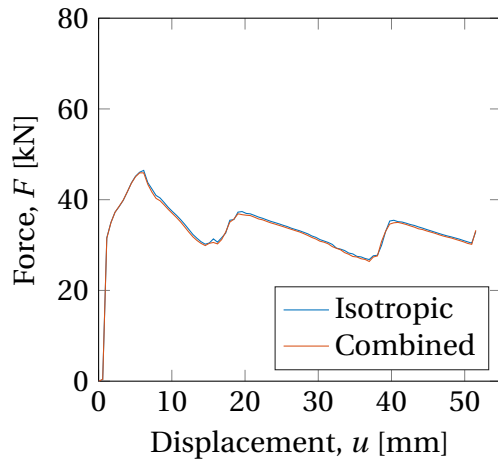
(a) T4 crushing force
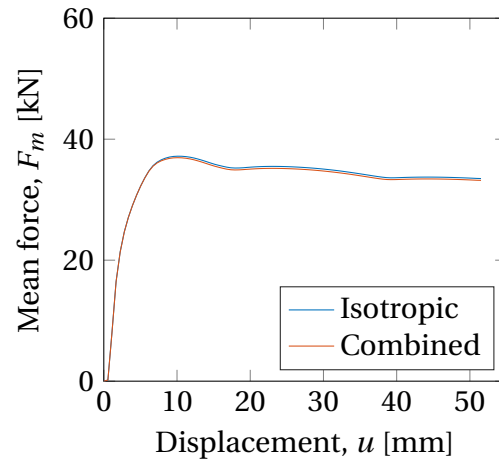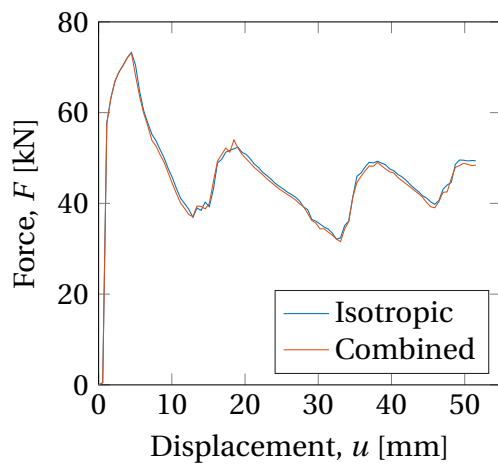
(b) T4 mean force
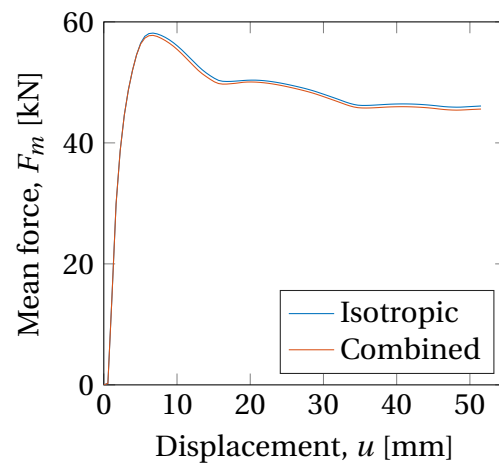
(c) T6 crushing force
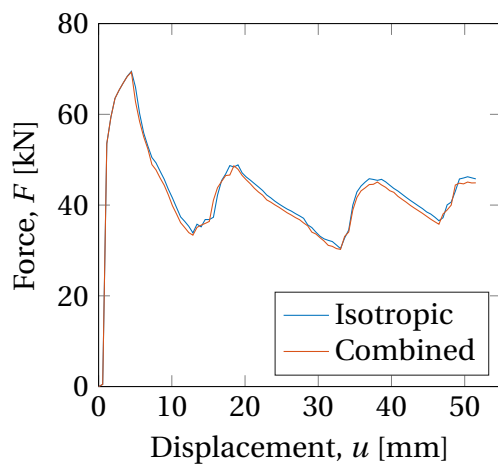
(d) T6 mean force
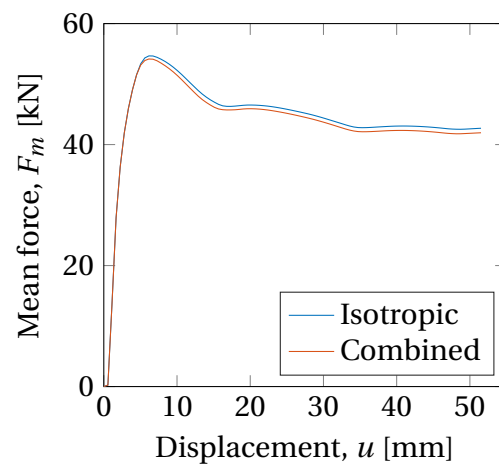
(e) T7 crushing force

(f) T7 mean force

Figure 5.6: Crushing force (left) and mean force (right) versus time for the single chamber profile with isotropic and combined material hardening models
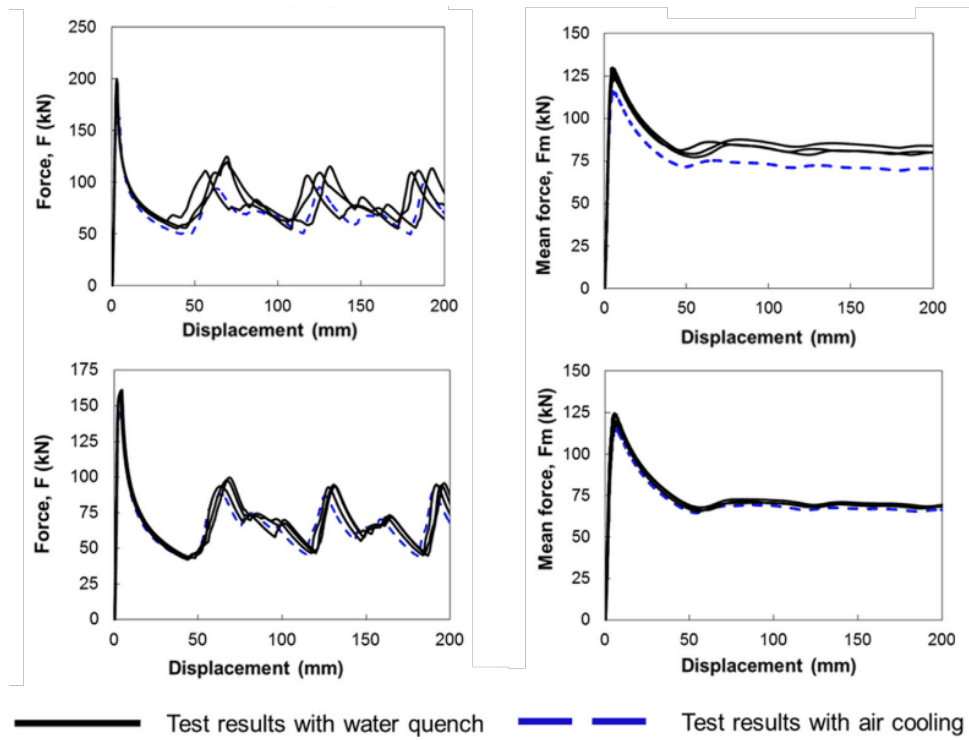
Figure 5.7: Results taken from Hoang et al. [12] for AA6060-T6 (upper) and AA6060-T7 (lower)

	Si	Fe	Mg	Al
Hoang et al. [12]	0.44	0.22	0.47	Bal.
Westermann et al. [27]	0.4	0.2	0.5	Bal.

Table 5.2: Comparison of the chemical composition of AA6060 in wt% from the tensile tests used in this thesis, taken from Westermann et al. [27], and from Hoang et al. [12]

in Hoang et al. [12]. Compared to this thesis, the material in Hoang et al. [12] has a slightly different chemical composition, seen in table 5.2, and the temper aging was carried out with slightly higher temperatures for shorter durations than what was used for this thesis, as seen in Table 5.3.

	Temper aging	
Temper	This thesis	Hoang et al. [12]
T6	175 °C for 8 hours	185 °C for 5 hours
T7	175 °C for 11 days	185 °C for 7 days

Table 5.3: Comparison of temper aging for tensile tests in this thesis and in Hoang et al. [12]

5.1.3   Discussion

The results show negligible variation between the two material hardening models for the single chamber profile. This may be attributed to the fact that most elements are not subjected to much cyclic or fluctuating loading. Some unloading is seen after the initiation of each fold, but this seems to have no significant impact on the distinction between material models.

In regards to comparison between the tempers, T4 has no fracture, as opposed to T6 and T7. This is most likely caused by the lower yield stress and higher work hardening for T4 which leads to greater distribution of the strain and higher ductility. The higher distribution of the strain means the chance of fracture lessens, which is an advantage if the material is to be used in a crash box. Another desirable trait for a crash box is high energy absorption potential, which would make T6 and T7 more suitable. To reach a conclusion regarding ductility versus energy absorption, additional experiments would be need to be performed.

5.1.4   Triple Chamber Profile

The results for the triple chamber profile are presented as plots depicting force versus displacement and mean force versus displacement. The strain field is presented for the final deformed shape, where fractured elements are deleted.

After comparing the final deformed shape of the simulations with pictures from a previous in-house SIMLab laboratory experiment using the same profile, it was concluded that using eigenmodes gave an unwanted unsymmetrical shape compared to the experiment. The simulations were therefore carried out without imperfections. The comparison is shown in Figure 5.8, where it is evident that the bottom chamber is considerably distorted when eigenmodes were included. Even though some sides did not fold the same way in the simulations as the experiment, abandoning eigenmodes did recreate the symmetrical shape of the bottommost side. The experiment used another aluminum alloy, namely AA6082.26, but since the two alloys belong to the same aluminum series and the same geometry was used, the experiment was considered an indication of what to expect.

As seen in Figures 5.9c and e the lack of imperfections gives a large force spike when initiating the first fold for T6 and T7, but this should not play a crucial role on the response once this fold is formed. It does however, affect the magnitude of the mean force in Figures 5.9d and f, since an increased amount of energy is needed to deform the profile.
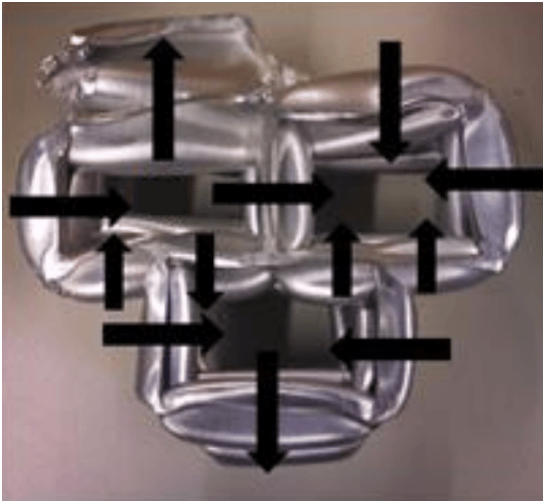
(a) Picture from a previous in-house SIMLab experiment using aluminum alloy AA6082.26. The arrows symbolize which way each side initially folded
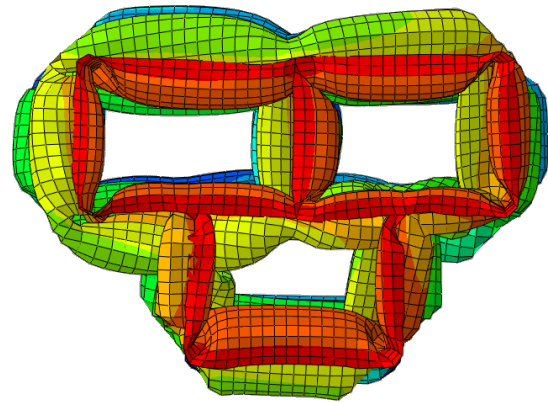
(b) Model with 0 eigenmodes and T4 with isotropic hardening
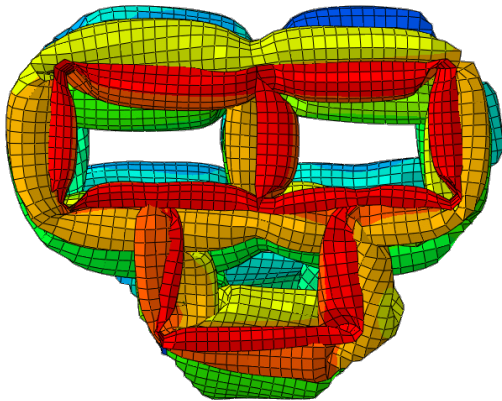
(c) Model with 5 eigenmodes and T4 with isotropic hardening
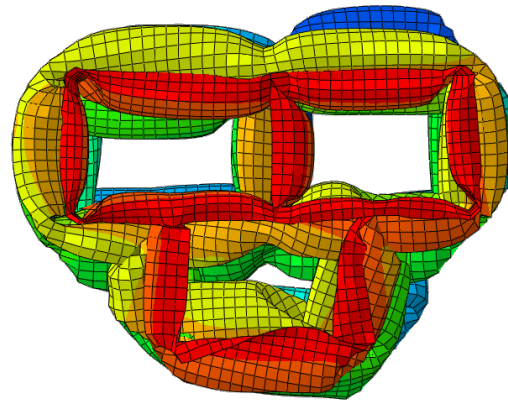
(d) Model with 20 eigenmodes and T4 with isotropic hardening

Figure 5.8: Deformed state for triple chamber profile. The color scheme represent total displacement to make it easier to distinguish different folds
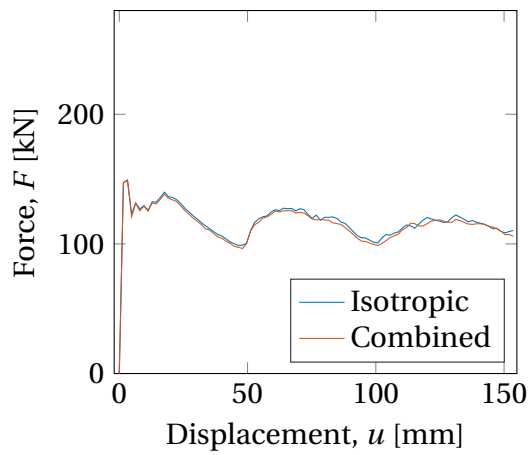
(a) T4 crushing force
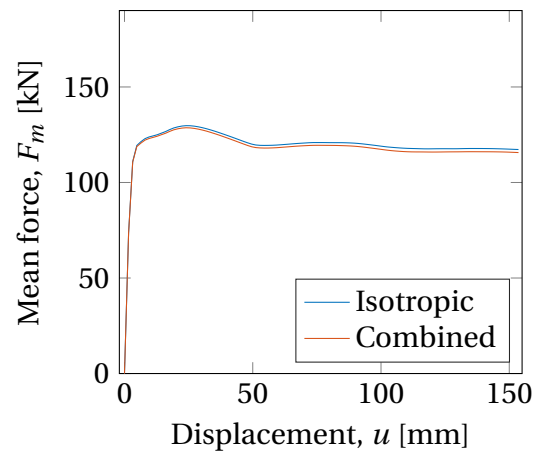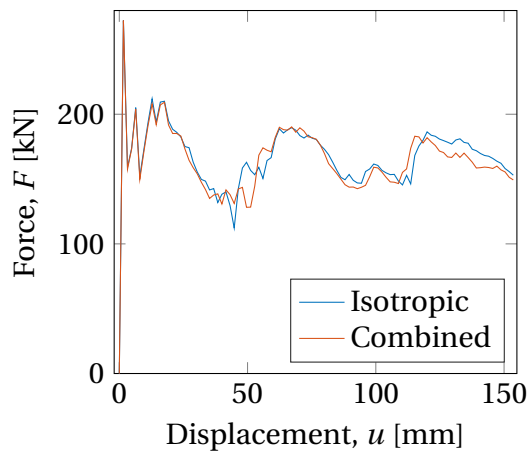
(b) T4 mean force
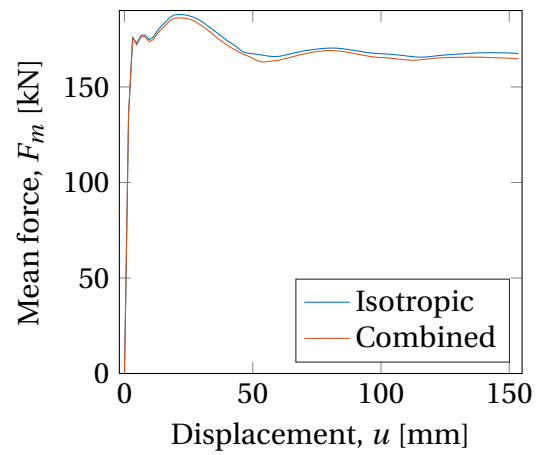
(c) T6 crushing force
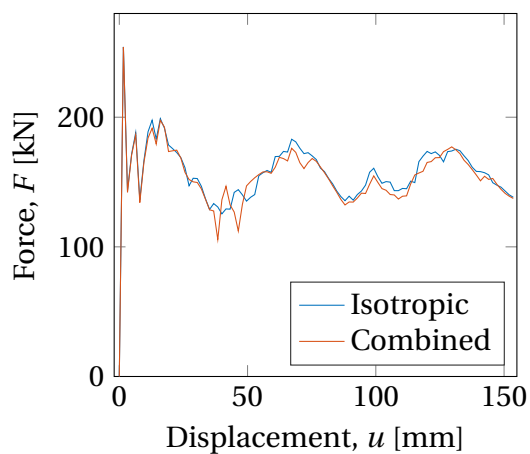
(d) T6 mean force
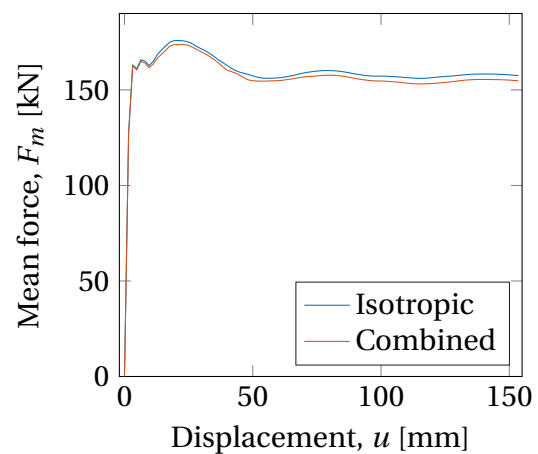
(e) T7 crushing force

(f) T7 mean force

Figure 5.9: Crushing force (left) and mean force (right) versus time for the triple chamber profile with isotropic and combined material hardening models

| | Maximum equivalent plastic strain, p | |
Temper	Isotropic hardening	Combined hardening
T4	2.751	2.753
T6	3.215	3.143
T7	3.488	3.078

Table 5.4: Maximum equivalent plastic strain in the model for the final deformed shape for the triple chamber profile

The equivalent plastic strain field in the final deformed shape for the triple chamber profile with a combined hardening model is shown in Figure 5.10. It reveals that fracture occurs in the corners of the upper left chamber for tempers T6 and T7, but not for T4. The final deformed shapes for the remaining simulations are shown in Figure A.10 in Section A.4.1 of the appendix. The maximum equivalent plastic strain, p, for all tempers and hardening models are listed in Table 5.4. It reveals lower strain for T4 than T6 and T7. Figure 5.9 shows that T4 differs from the other tempers in the force plots. It does not have a large force spike like the other tempers and therefore has a lower mean force. It also has a smoother response with less oscillations than T6 and T7.

As with the single chamber profile, the isotropic material hardening model takes up slightly more energy than the combined model for all tempers. This is expected since the isotropic model gives a larger yield surface than the combined model, as explained in Section 2.2.2, meaning it will require more work to obtain the same deformation. For the triple chamber profile, tempers T6 and T7 reveals a noticeable difference between the hardening models in the force-displacement plots, while this is not the case for T4. This may be caused by the complexity of the triple chamber profile, which may lead to an increased number of stress states for each element throughout the simulation.

5.1.5 Discussion

The triple chamber profile displays a noticeable, but still small, difference between the two material hardening models. This could be caused by the fact that the profile has a complex geometry which might cause a more fluctuating stress state during the crushing. The fact that fracture occurs in both T6 and T7 will further increase the variation of the stress state on neighbouring elements. Another possibility is that this difference is caused by the oscillating forces at the first fold from the lack of imperfections. This would explain why T4 shows almost no difference between isotropic and combined hardening models, as it has no fracture and it is not as affected by the lack of imperfections.

(a) T4

(b) Color scheme for T4

(c) T6

(d) Color scheme for T6

(e) T7
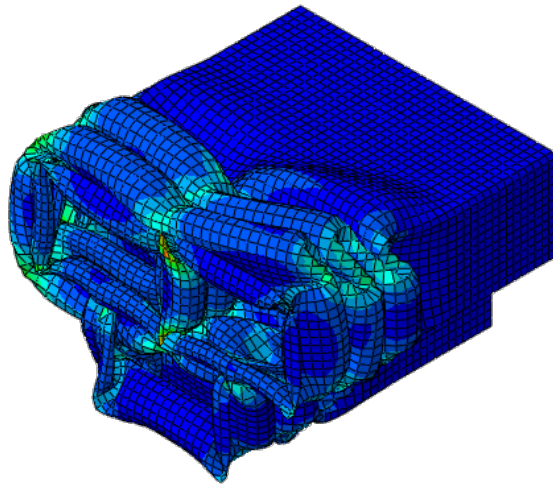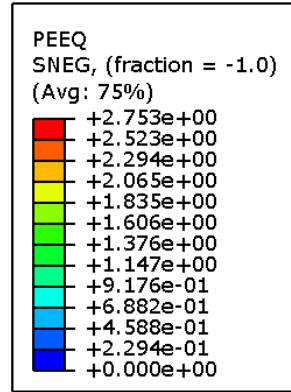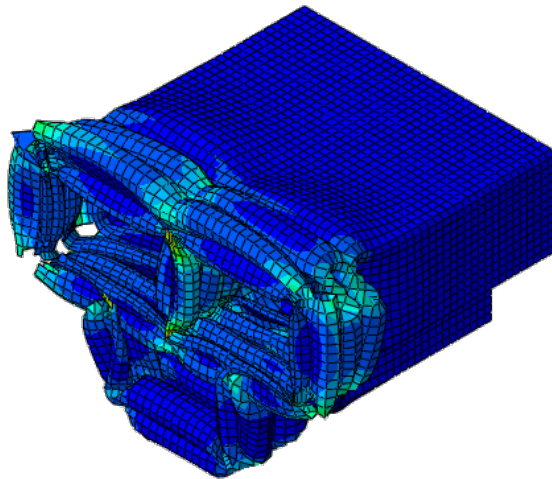
(f) Color scheme for T7

Figure 5.10: The equivalent plastic strain field for the final deformed state for the triple chamber profile with combined hardening

Temper T4 has a lower maximum equivalent plastic strain than T6 and T7, and shows no sign of fracture. This may be caused by the lower yield stress and higher work hardening. This will lead to a greater distribution of the strain which leads to higher ductility and a decreased risk of fracture.

5.2   Forming Limit Diagram

A forming limit diagram (FLD) denotes how much strain a sheet of metal can sustain for various strain states and it can be made with either experimental or numerical data. When a numerical calculation is used to estimate the FLD, a square patch of the elements is considered. One or several elements are set to be slightly thinner than the rest of the sheet. Two opposite sides are defined as the major sides and these are given a constant strain rate for all strain states. The two remaining sides are defined as the minor sides and are given strain rates ranging from 0 % to 100 % of the major sides' strain rate. The maximum capacity for each strain state is taken as the strain when localization occurs in the thinner elements. By creating this diagram, the importance of kinematic hardening for metal sheets in several strain states can be investigated. This chapter will present both an ordinary study and a pre-strained study. A normal FLD was created in the ordinary study, while the pre-strained study altered the yield surface before the FLD was created.

5.2.1   Modeling

A FLD was generated in the ordinary study, using a sheet where the center element was given a thickness equal to 99.8 % of the other elements of the sheet. The height and width of the sheet were set to 51 times the sheet's general thickness, resulting in a mesh consisting of 51x51 elements as seen in Figure 5.11 were the thin element is highlighted. The sheet sides were given various constant displacement rates. This was done for 11 strain states, ranging from pure uniaxial strain to pure biaxial strain. The points in the forming limit diagram were extracted when the strain increment through the thickness for the center element exceeded ten times the average strain increment through the thickness for the rest of the elements. This is visualized in Figure 5.12 for T4 with combined hardening and in Figure A.11 and A.12 in Section A.4.2 of the appendix for the additional tempers and hardening models.

The pre-strained study was carried out by giving the sheet a predefined plastic strain in the major direction of approximately $\varepsilon^p = 2\,\%$, while the boundaries of the minor direction were
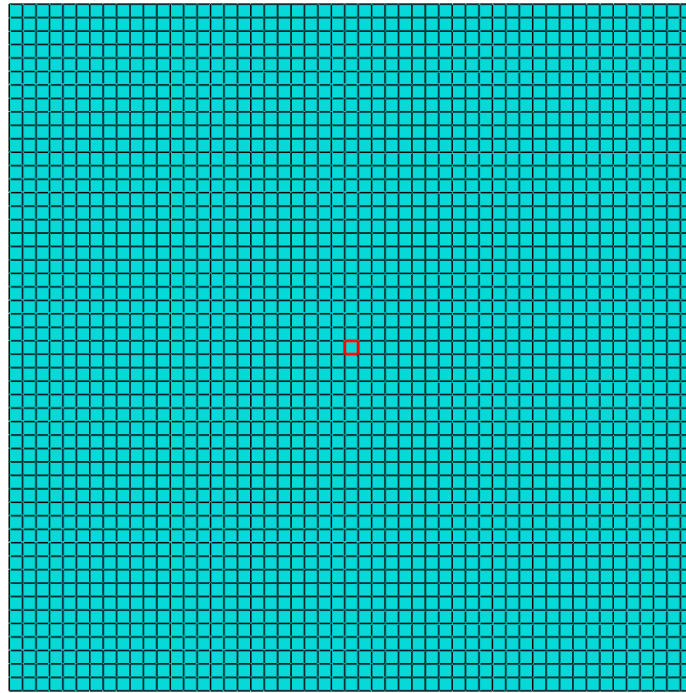
Figure 5.11: FLD mesh with highlighted center element
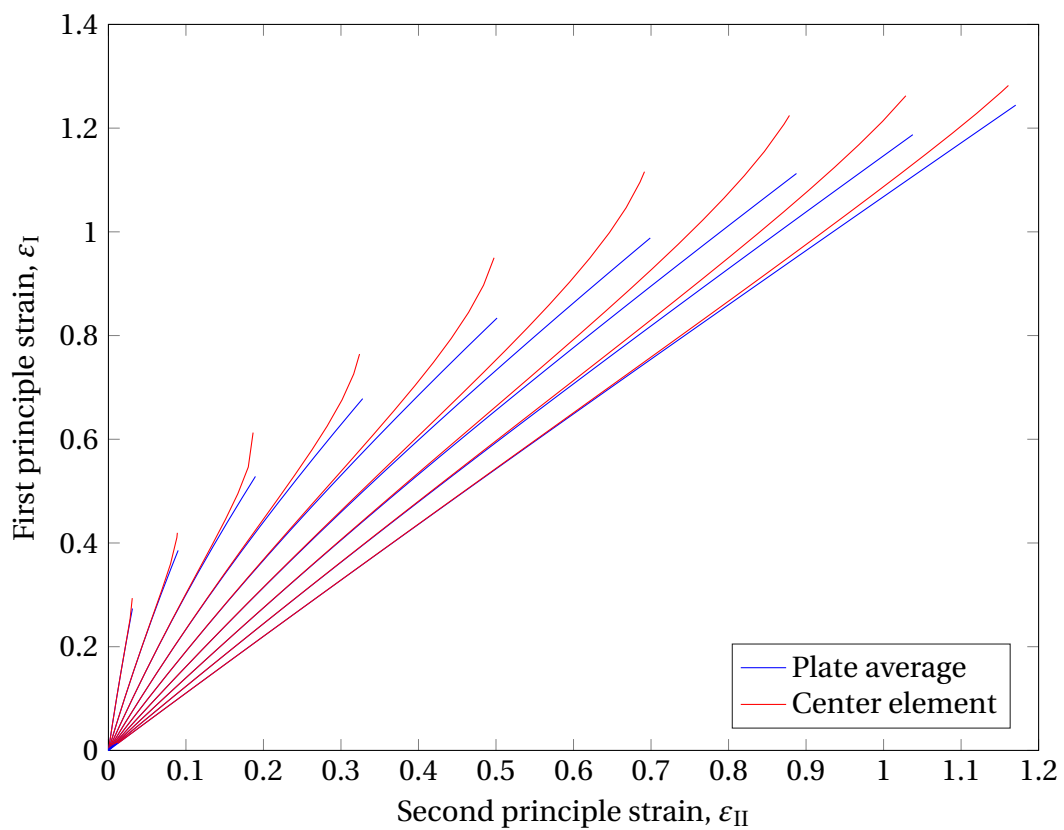
Figure 5.12: Plot showing the relationship between the principal strains for T4 with combined hardening

kept free. By creating a forming limit diagram after this predefined stretching, the different hardening models would have unique yield surfaces initially which may lead to a difference in the results.

5.2.2   Results

The forming limit diagrams for both the ordinary and the pre-strained study are shown in Figure 5.13, and in Figure 5.14 the two studies are compared. $\varepsilon_{II} = 0$ denotes pure uniaxial strain, while the dotted line denotes where the strain is biaxial. Each circle symbolizes one numerical simulation, and the lines are linearly interpolated between these points. As seen in Figure 5.14, the sheets in the pre-strained study can take higher strain before localization than the sheets in the ordinary study.

If the tempers T4 and T6 are compared, shown in Figure 5.15, it becomes evident that T4 can take higher strains than T6 before localization occurs in all strain states. The figure also shows that the strain level for temper T7 is almost identical to T6 in the uniaxial end of the diagram, but along the biaxial line T7 is similar to T4.

For T4 the differences between the hardening models are more distinct for increased biaxial strain, while for the pre-strained study there are larger differences towards the uniaxial end, $\varepsilon_{II} = 0$, of the diagram. The FLDs for T6 show that this temper is almost unaffected by the material hardening model for both the ordinary and the pre-strained study. For both studies, T7 shows a small, almost constant, difference between hardening models for most of the 11 strain states. Even though small differences are noticeable in the plots, the different hardening models seem to have limited influence on the results overall.

An interesting observation is that whenever the isotropic hardening model differs from the combined model it can take higher strains before localization occurs, except for the pre-strained T4 case shown in Figure 5.13b. This anomaly may be caused by the especially steep slope of the kinematic hardening for T4, seen in Figure 4.7a, which would lead to a considerable work hardening at low strains. Further work is needed to be able to conclude on this matter.
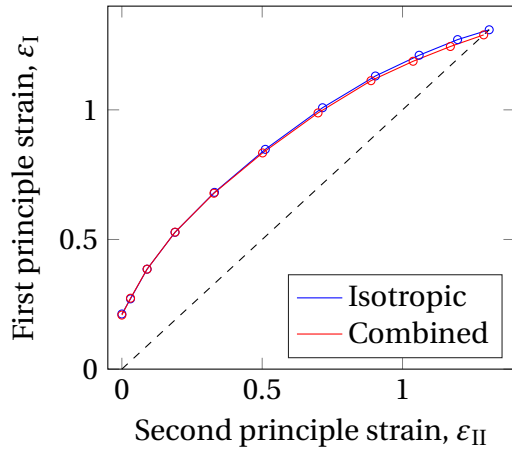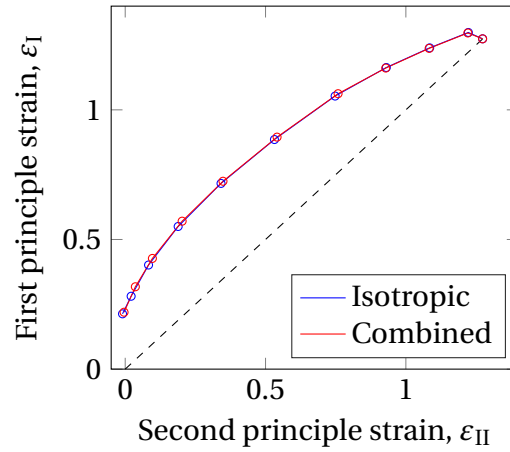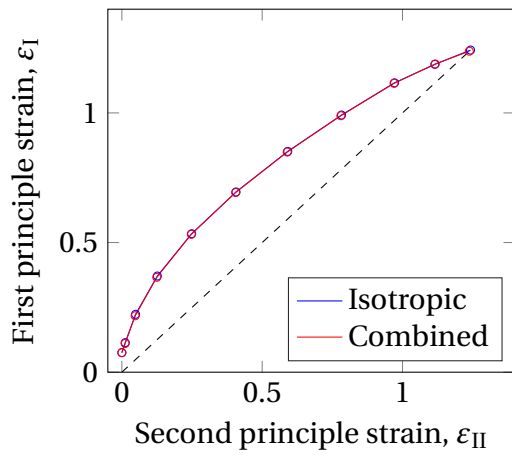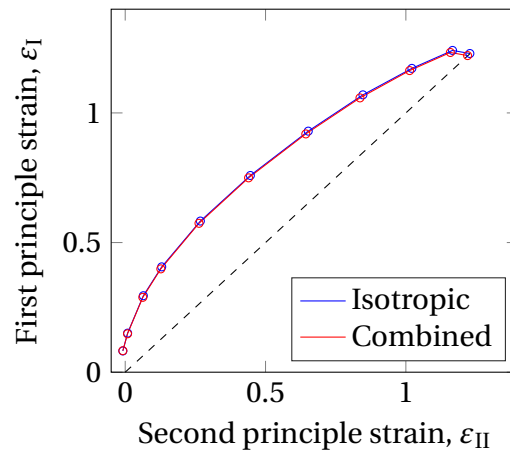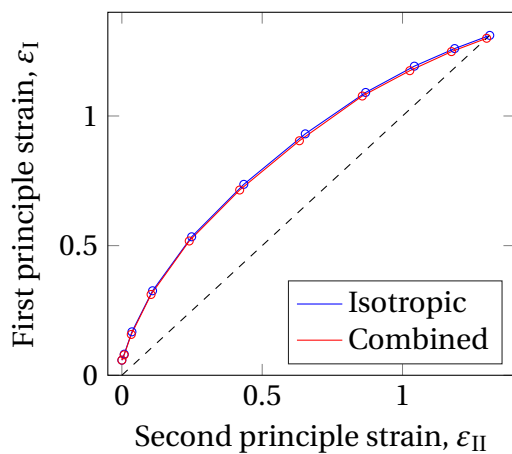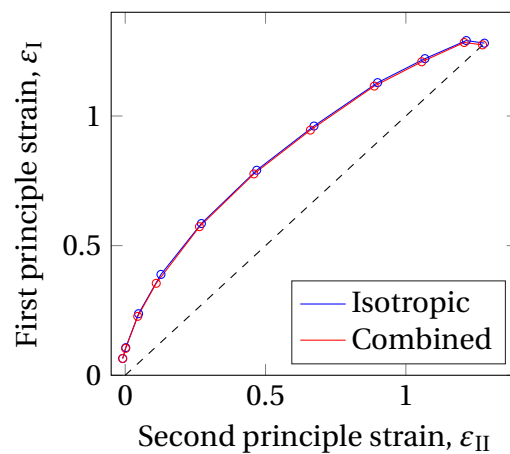
Figure 5.13: FLDs showing the relationship between the two principal strains at localization for the ordinary (left) and pre-strained study (right) with isotropic and combined hardening models

(a) T4

(b) T6

(c) T7
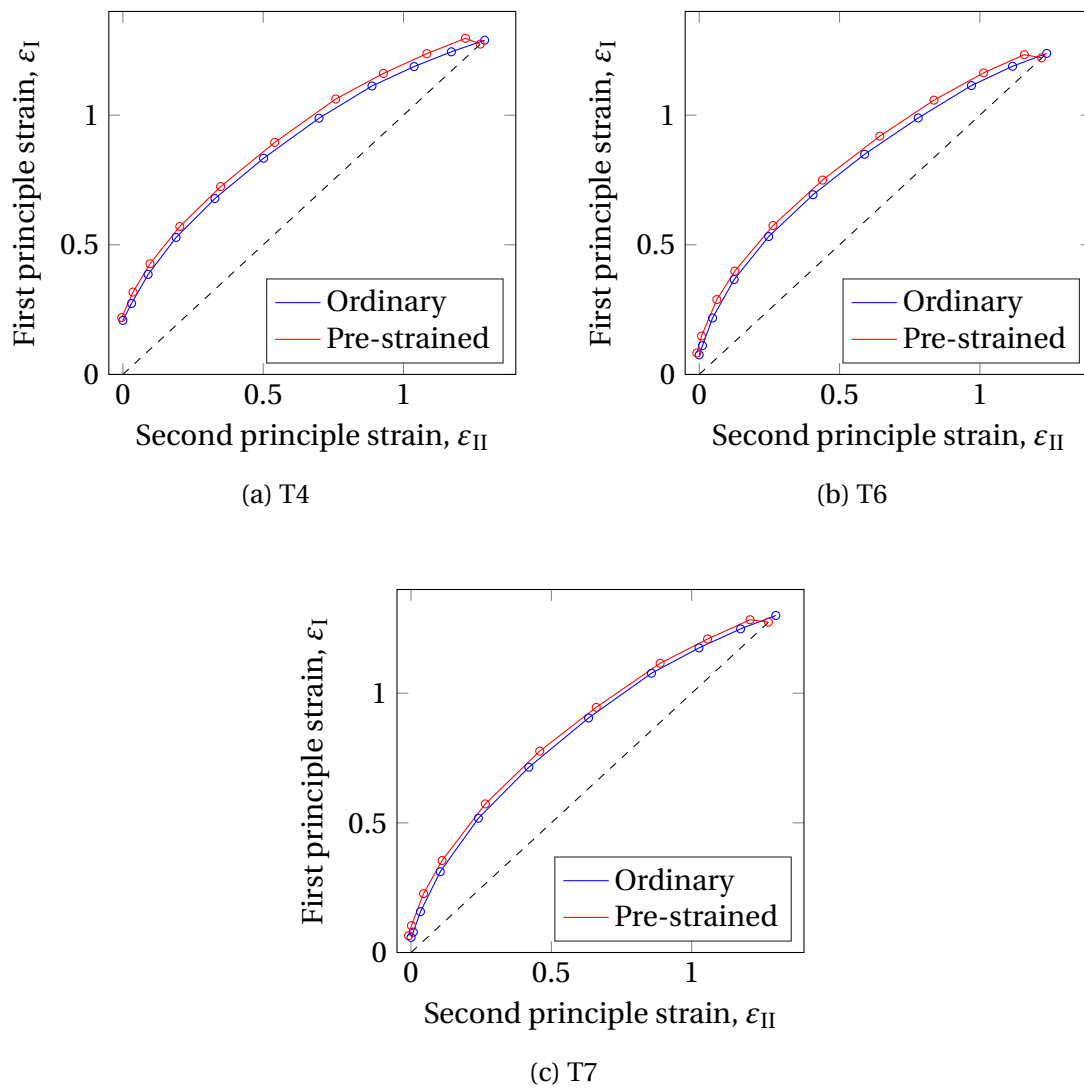
Figure 5.14: FLDs comparing the ordinary and pre-strained study with the combined hardening model
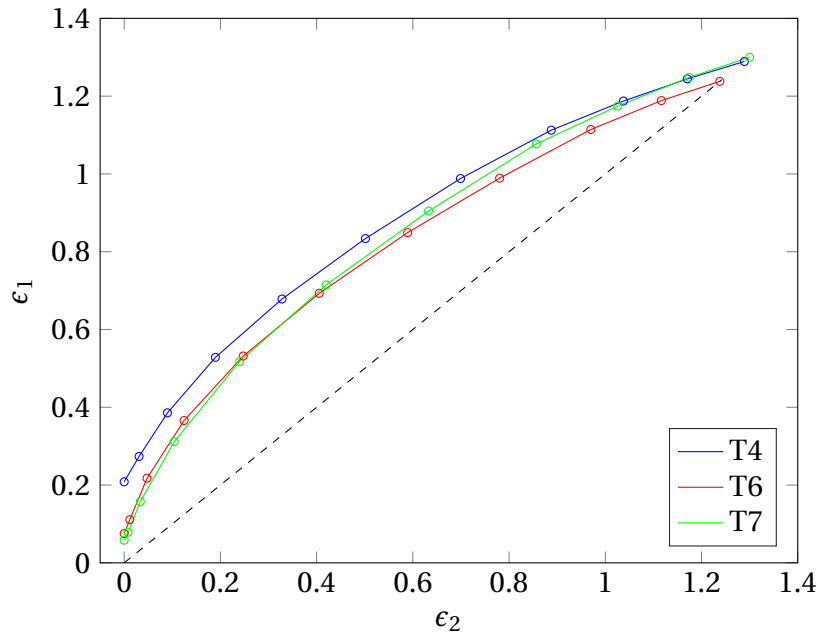
Figure 5.15: FLD comparing the three tempers for the ordinary study with the combined hardening model

5.2.3 Discussion

The FLDs show little difference between the material hardening models since tension is the only stress state present, and as both of the material models were initially fitted to the same uniaxial tension data.

The increased strain level required for temper T4 compared to T6 is most likely caused by the lower yield stress and higher work hardening. This would lead to yielding in most of the sheet before localization occurs, meaning it can take higher accumulated strains.

5.3 Impact Loading on Plates

This case is based on three test series described in Langseth et al. [13]. The paper studies the effect of impact loading on stiffened plates to simulate the effect of dropped objects on offshore structures. The three test series are denoted E1, E2 and DM. E1 and E2 are two test series of the same pinned plate with bisymmetrical stiffeners where the plate thickness and projectile velocity were varied, while DM is a clamped plate with unsymmetrical stiffeners.

(a) Plates E1 and E2   (b) DM plate
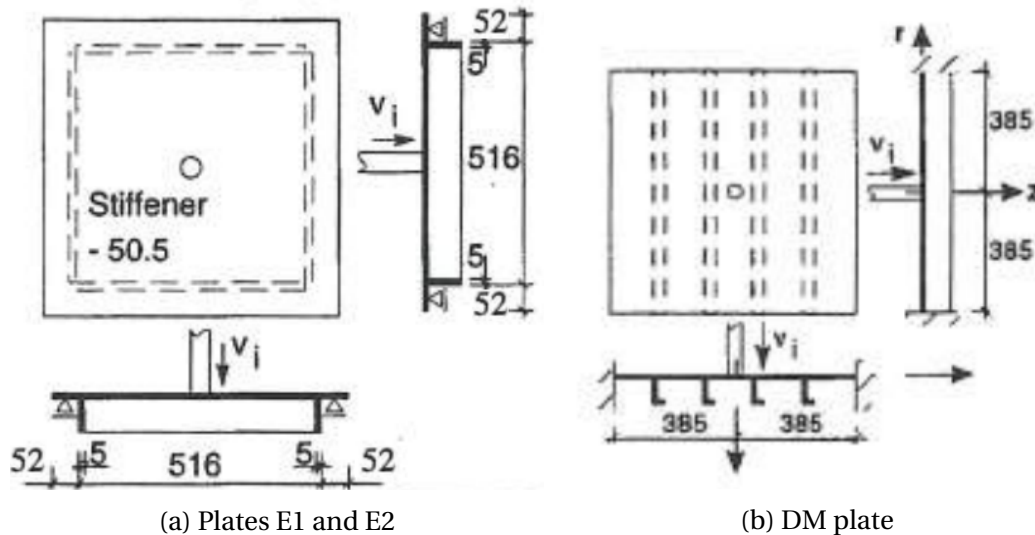
Figure 5.16: Geometry for plates subjected to impact loading from Langseth et al. [13]

Test series	Plate thickness [mm]	Projectile velocity [m/s]
E1	6.03	8.26
E2	9.96	9.47
DM	4.40	9.22

Table 5.5: Plate thickness and projectile velocity for E1, E2 and DM

5.3.1   Modeling

The geometries of the plates were taken from Langseth et al. [13] and are given in Figure 5.16a
for E1 and E2 and in Figure 5.16b for DM. The cross section of the stiffeners for the DM case
have measures 3 mm x 50 mm and 22 mm x 3 mm for the vertical part and the horizontal part,
respectively. The dropped projectile was modeled as an analytic cylinder with a diameter of
36.5 mm and a point mass of 49.54 kg. Gravity was included in the simulation because the
projectile was deemed likely to bounce off the plates after impact [13]. The plate thickness
and projectile velocity were based on empirical data from Langseth et al. [13], is listed in
Table 5.5. The meshed plates are shown in Figures 5.17 and 5.18 and the elements used have
a size of 13 mm for E1 and E2 and 10 mm for DM.
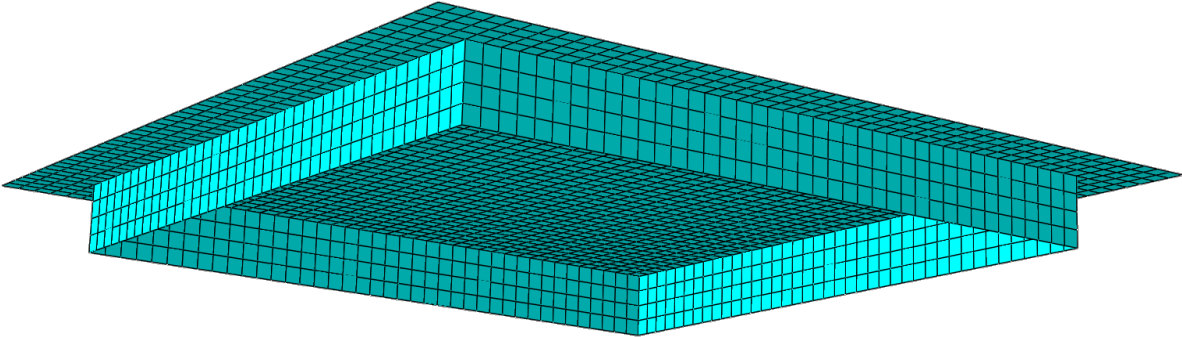
Figure 5.17: Mesh of the pinned plate with stiffeners, E1 and E2
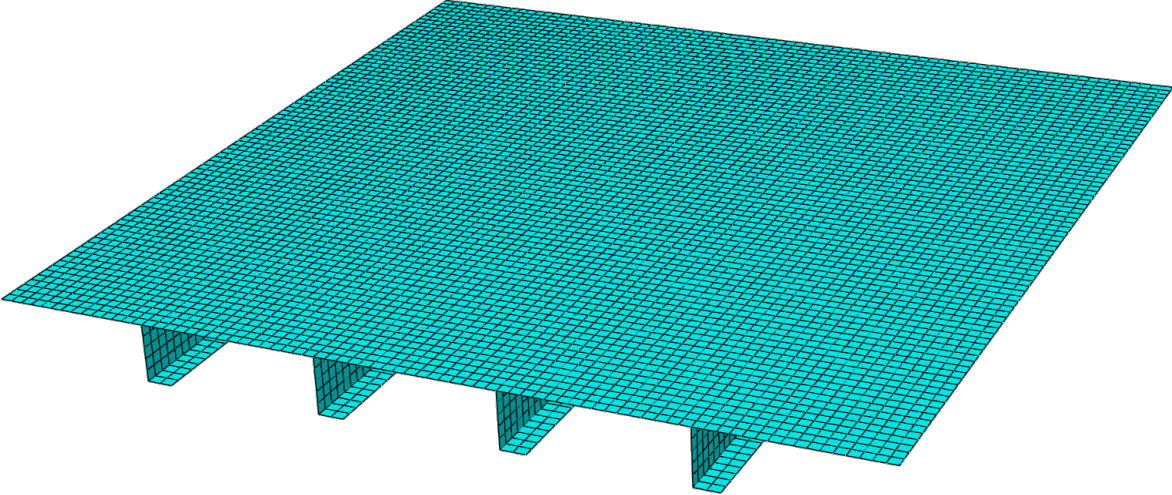
Figure 5.18: Mesh of the clamped plate with stiffeners, DM

		Maximum equivalent plastic strain, p	
Test series	Temper	Isotropic hardening	Combined hardening
	T4	0.3970	0.3981
E1	T6	0.3587	0.3606
	T7	0.3911	0.3964
	T4	0.2874	0.2874
E2	T6	0.2598	0.2609
	T7	0.2747	0.2759
	T4	0.3696	0.3712
DM	T6	0.4325	0.4381
	T7	0.5352	0.5431

Table 5.6: Maximum equivalent plastic strain in the simulation models for the final deformed shape for impact loading

5.3.2   Results

This section includes figures of the equivalent plastic strain field for the final deformed state of the plates to visualize the global response and the equivalent plastic strain throughout the plates. Results are depicted in plots of total reaction force and displacement of the center node versus time. These plots give good understanding of both the global displacement of the plates and the forces causing the response.

The deformed state of the plates are shown in Figures 5.19, 5.20 and 5.21 for E1, E2 and DM respectively. Even though E2 has a higher projectile velocity, E1 has a higher equivalent plastic strain because it is a thinner plate. All three plates have undergone plastic deformation only in the center area where the projectile hit, for all tempers and material hardening models. This is shown in all final deformed figures with a detailed cut view. For the simulations with the isotropic hardening model, the final deformed state plots are given in Figures A.13, A.14 and A.15 in Section A.4.3 of the appendix.

The maximum equivalent plastic strain in the models are listed in Table 5.6 for all test series, tempers and material hardening models. It is seen that the combined hardening model has slightly more equivalent plastic strain compared to the isotropic model for all test series and tempers. If the tempers are compared, it becomes evident that T6 has lower equivalent plastic strain than T4 and T7 for test series E1 and E2. The DM test series on the other hand, has lower equivalent plastic strains for T4 than the other two tempers.

The force and displacement plots for E1, E2 and DM are shown in Figure 5.22, 5.23 and 5.24, respectively. They show no significant difference between temper T6 and T7 for neither force nor displacement versus time for any test series. T4 has lower maximum force and more
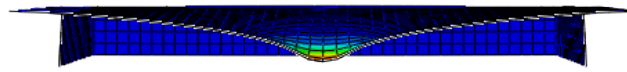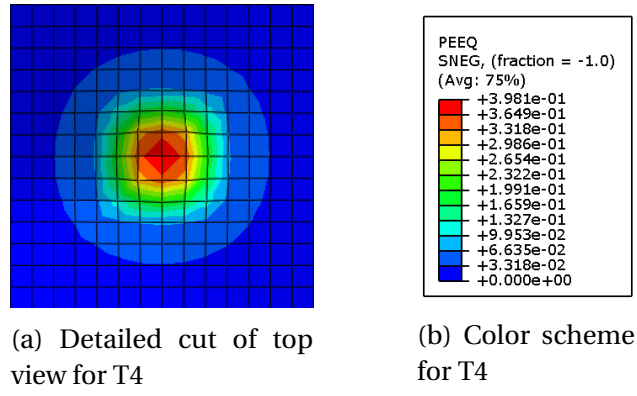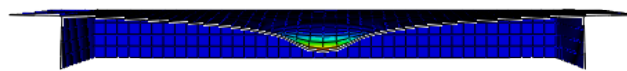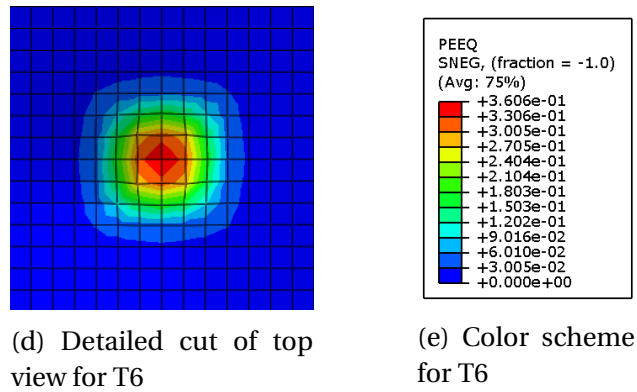
(a) Detailed cut of top view for T4

(b) Color scheme for T4

(c) Side view for T4 with cut through center line

(d) Detailed cut of top view for T6

(e) Color scheme for T6

(f) Side view for T6 with cut through center line

(g) Detailed cut of top view for T7

(h) Color scheme for T7
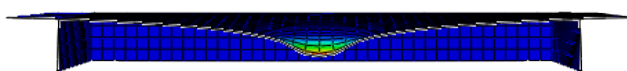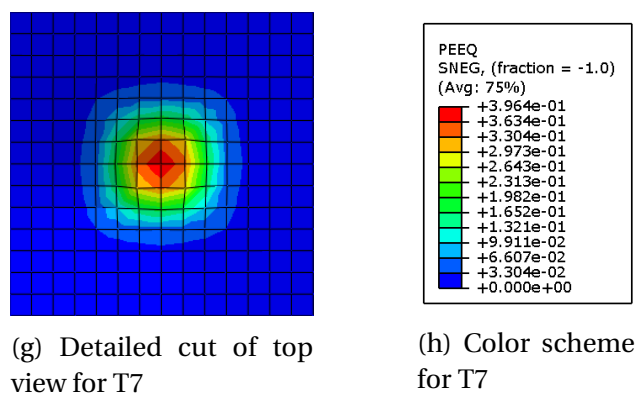
(i) Side view for T7 with cut through center line

Figure 5.19: The equivalent plastic strain field in the final deformed shape of the E1 test series with the combined hardening model

(a) Detailed cut of top view for T4

(b) Color scheme for T4

(c) Side view for T4 with cut through center line

(d) Detailed cut of top view for T6

(e) Color scheme for T6

(f) Side view for T6 with cut through center line

(g) Detailed cut of top view for T7

(h) Color scheme for T7

(i) Side view for T7 with cut through center line
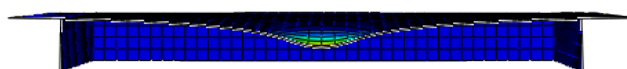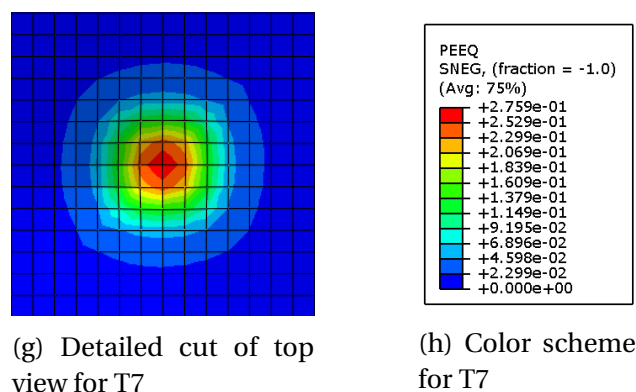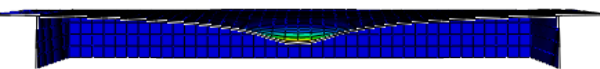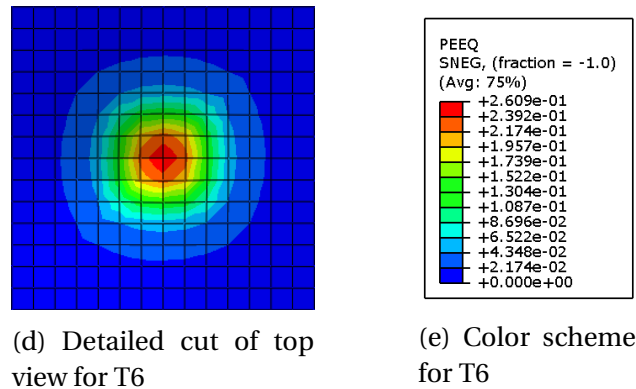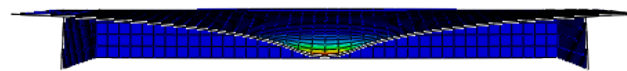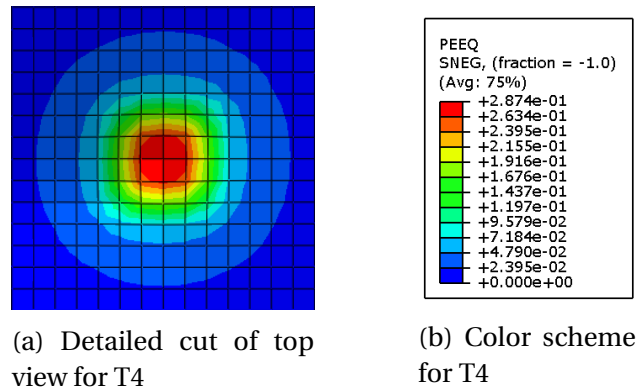
Figure 5.20: The equivalent plastic strain field in the final deformed shape of the E2 test series with the combined hardening model
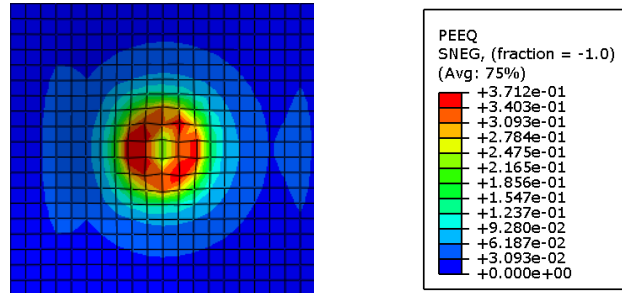
(a) Detailed cut of top view for T4

(b) Color scheme for T4
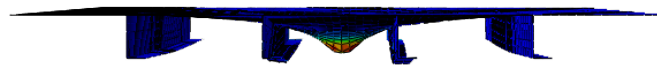
(c) Side view for T4 with cut through center line
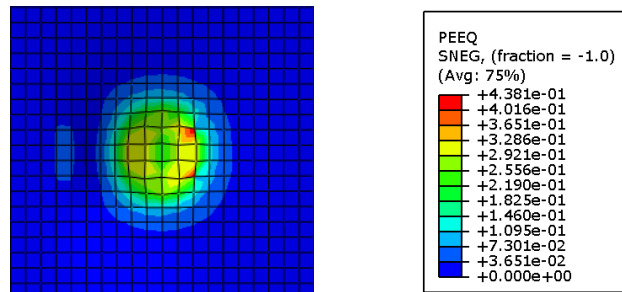
(d) Detailed cut of top view for T6

(e) Color scheme for T6
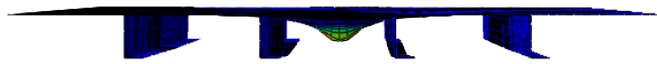
(f) Side view for T6 with cut through center line
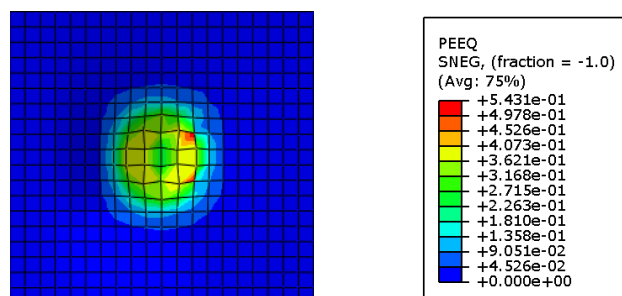
(g) Detailed cut of top view for T7

(h) Color scheme for T7
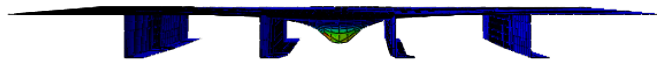
(i) Side view for T7 with cut through center line

Figure 5.21: The equivalent plastic strain field in the final deformed shape of the DM test series with the combined hardening model

displacement than T6 and T7, and it also has larger force oscillations when the force drops down to zero after the impact for test series E1 and E2.

There is a phase difference between the two material hardening models when the force oscillates around zero for test series E1, E2 and DM in temper T4. This phase difference is also present for T6 and T7 in test series DM, seen in Figures 5.24c and 5.24e. It is possible to distinguish the two material models in several points in test series E1 for T6, shown in Figure 5.22c, but the difference was concluded to be insignificant.

Both the E1 and E2 test series show larger force oscillations than seen in Figure 5.25a taken from Langseth et al. [13]. They also have less difference between the maximum displacement and the permanent displacement, which may be caused by the fact that Langseth et al. [13] used different aluminum alloys, namely AA5083 H112 for E1 and AA6082 T6 for E2. The force versus time plot for the DM test series has a similar shape as the plot in Figure 5.25b taken from Langseth et al. [13]. It does however, show less force and more displacement. This is as expected since the paper used steel instead of aluminum, which makes the two results not directly comparable. The paper uses aluminum for the E1 and E2 test series, but it is unclear if the results, shown in Figure 5.25a, apply to either E1 or E2, since the paper has presented the same results for both series.

5.3.3   Discussion

The main difference in material hardening models is observed when the force oscillates about zero. The difference is particularly noticeable for T4 which might be caused by the lower yield stress, resulting in more plastic strain which contributes to amplifying the difference between isotropic and combined hardening models. Tempers T6 and T7 show similar behavior in both the E2 and the DM test series. Neither show any difference between the isotropic and combined hardening models for E2 and both show only minor difference for DM. However, this is not the case for E1, where T6 shows a distinct difference while T7 does not. This suggests that the impact does not trigger a different structural response for the different material hardening models, but the oscillations caused by the impact do.

T4 has both more equivalent plastic strain and a greater distribution of strain than T6 for test series E2. This suggests that the higher yield stress of T6 leads to less strain. For the DM test series, T4 has lower maximum equivalent strain and a greater strain distribution than T6. This is probably attributed to the distribution of strain to the middle stiffeners, since it was not observed for test series E1 or E2.

(a) T4 force

(b) T4 displacement

(c) T6 force

(d) T6 displacement

(e) T7 force
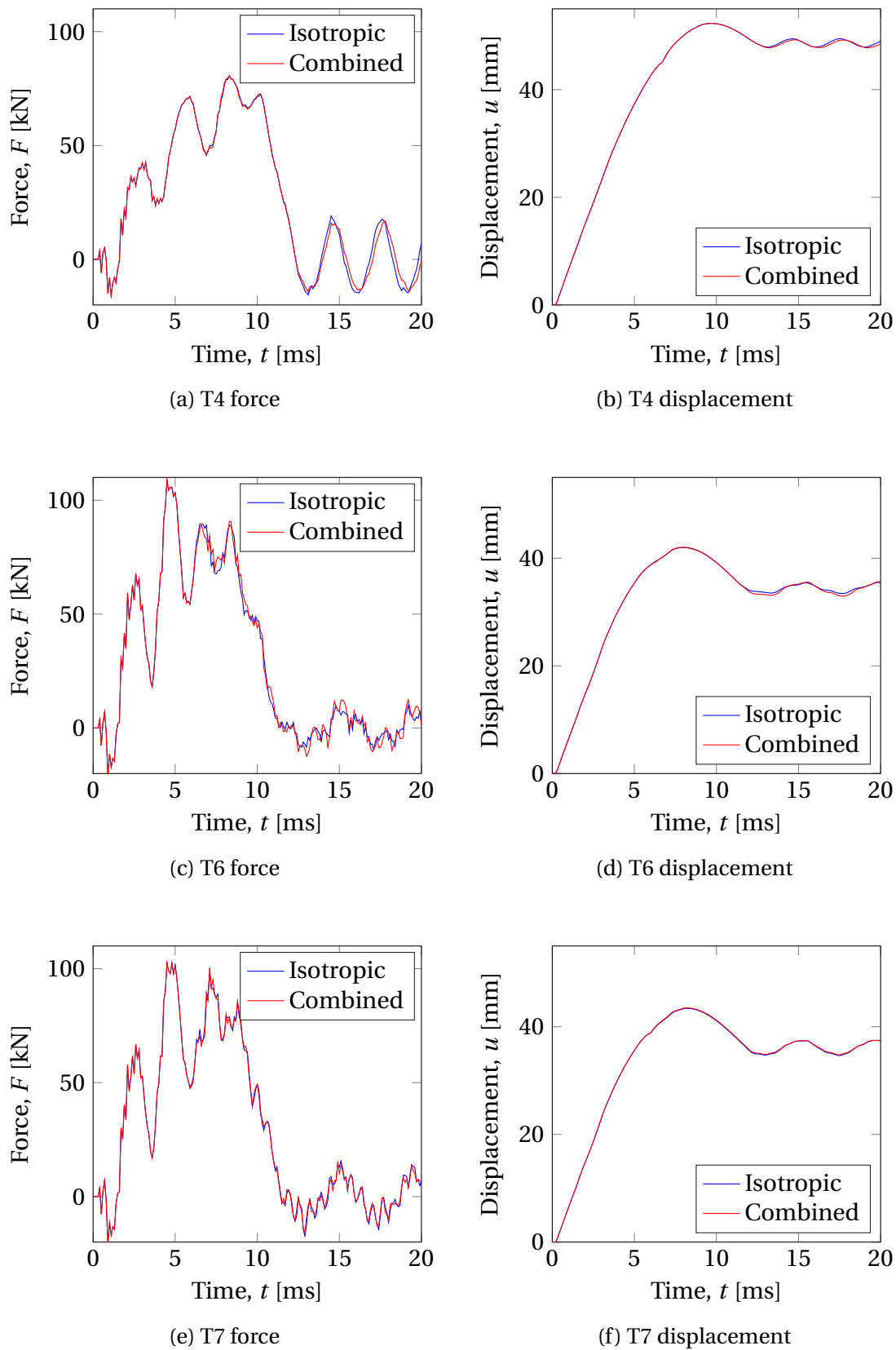
(f) T7 displacement

Figure 5.22: Impact loading on plate for test series E1. Total reaction force (left) and displacement of center node (right) versus time with isotropic and combined hardening models

(a) T4 force

(b) T4 displacement

(c) T6 force

(d) T6 displacement

(e) T7 force
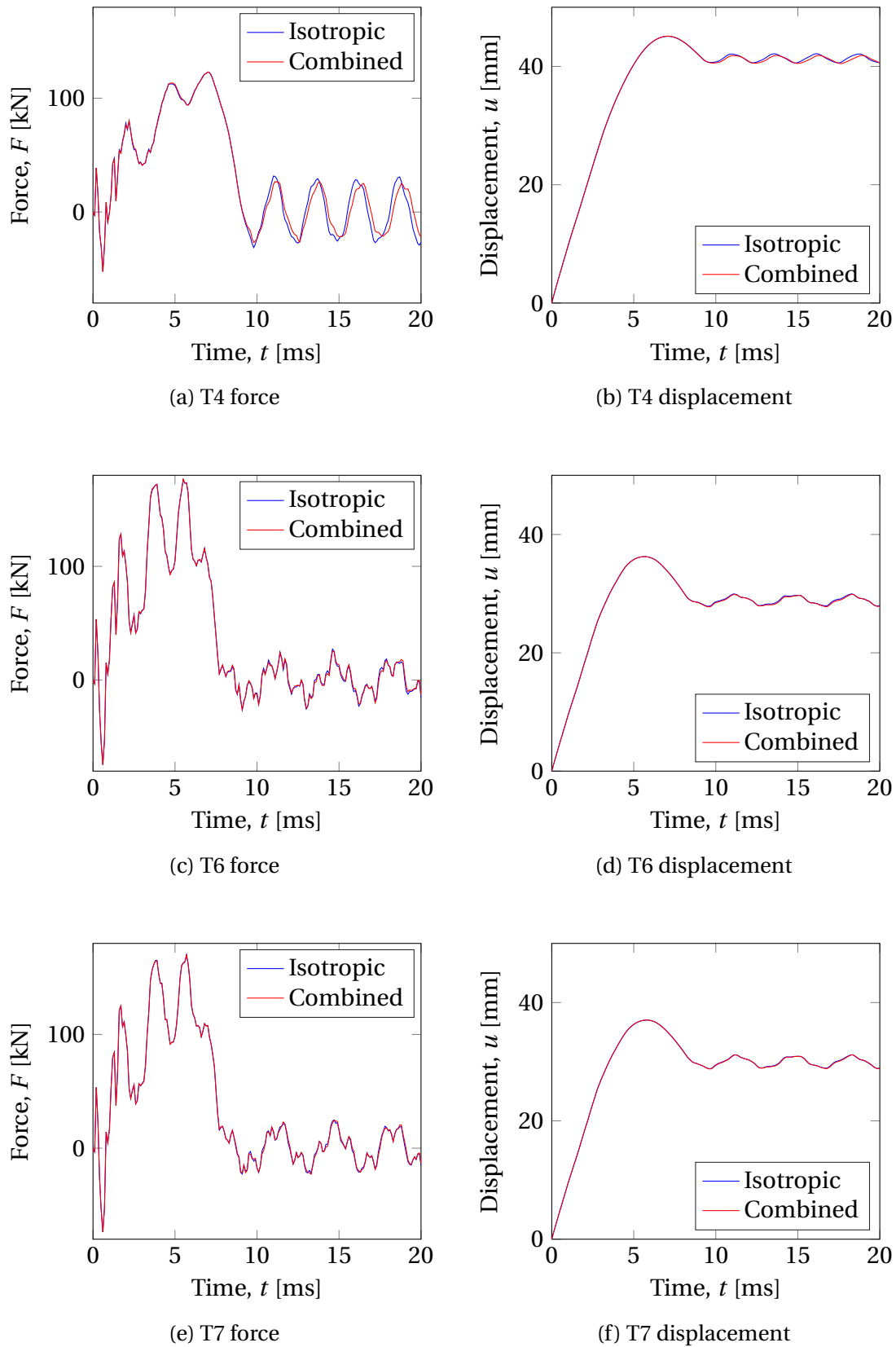
(f) T7 displacement

Figure 5.23: Impact loading on plate for test series E2. Total reaction force (left) and displacement of center node (right) versus time with isotropic and combined hardening models
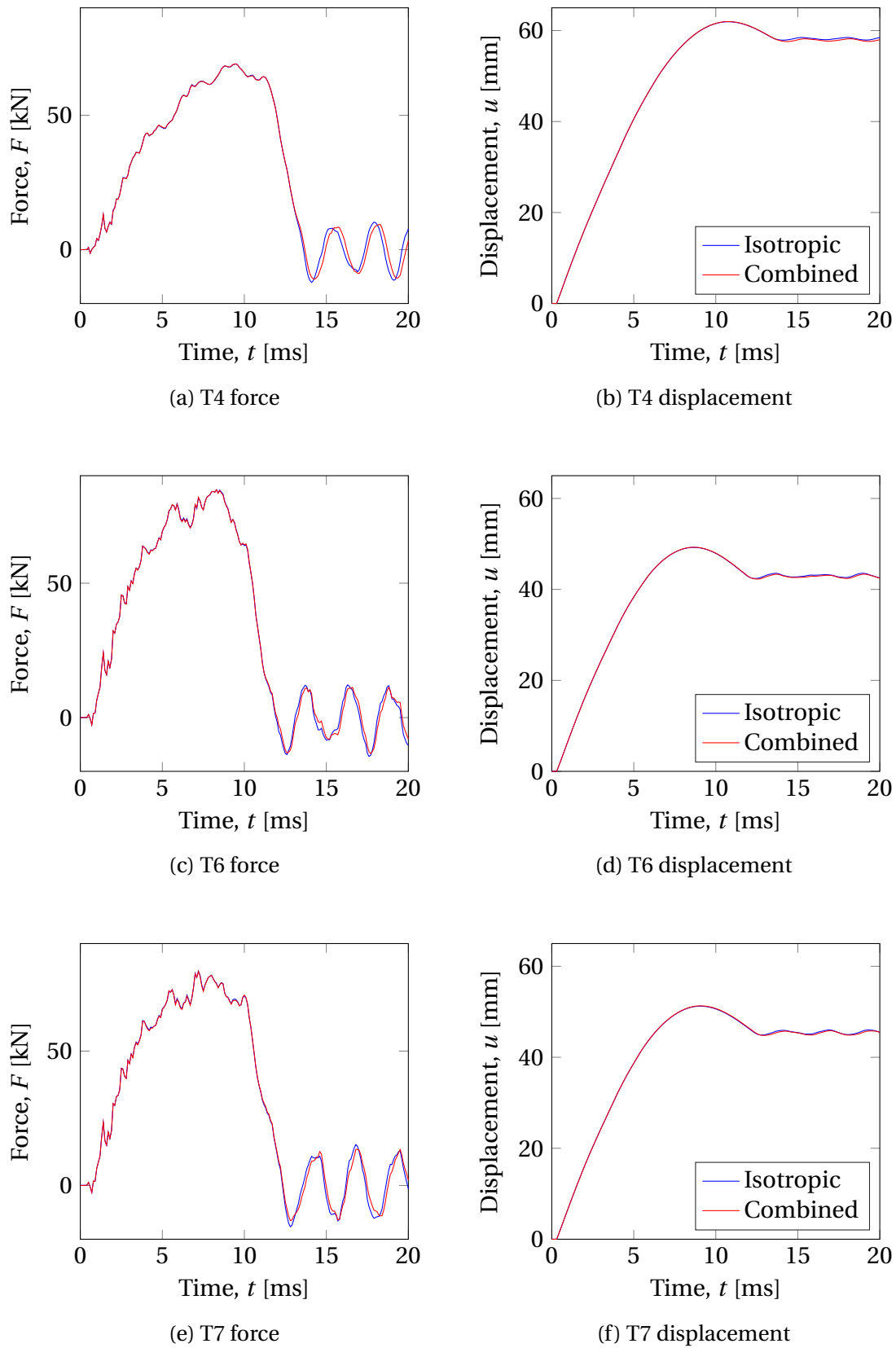
Figure 5.24: Impact loading on plate for test series DM. Total reaction force (left) and displacement of center node (right) versus time with isotropic and combined hardening models
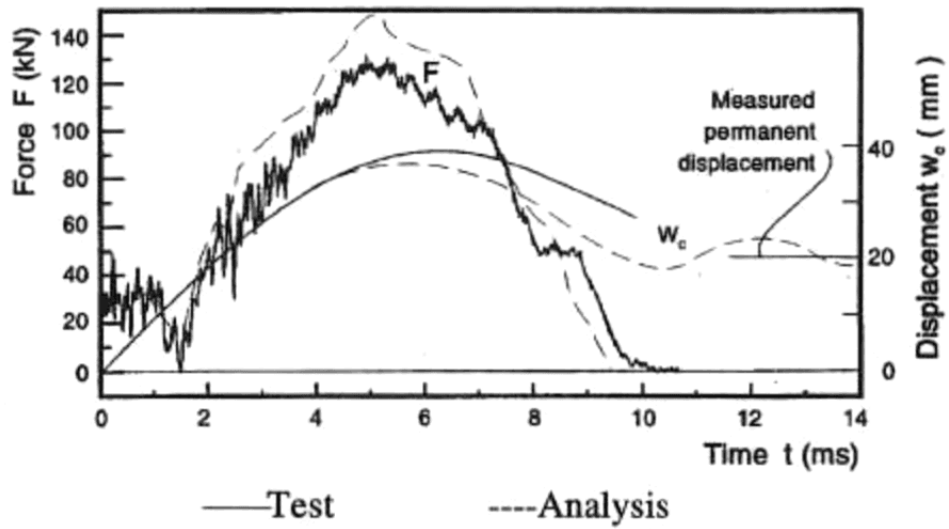
(a) Results for E1 and E2
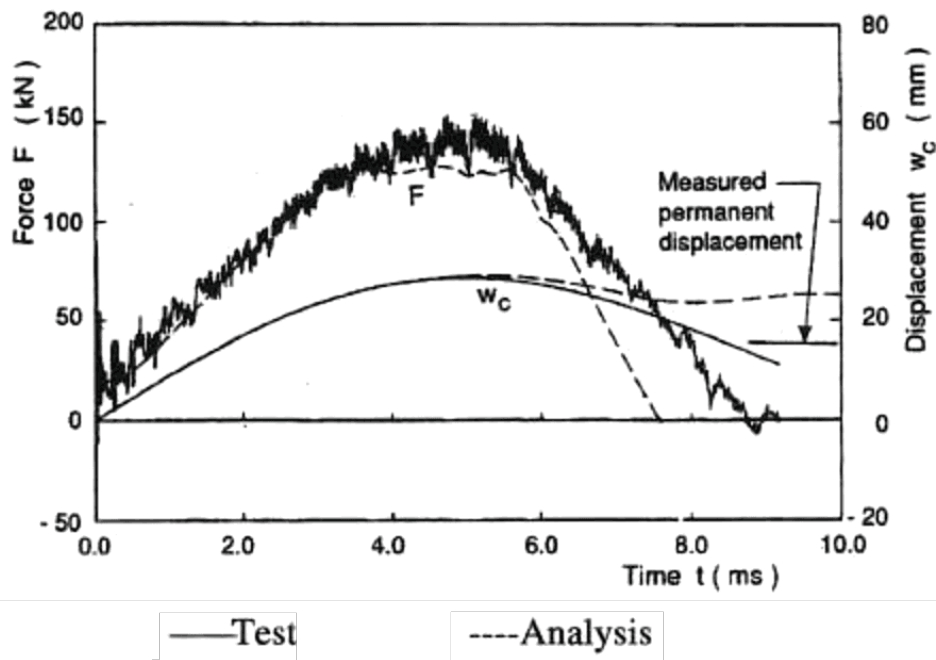
(b) Results for DM

Figure 5.25: Experimental and numerical results for E1, E2 and DM. Taken from Langseth et al. [13]

Height [mm]	Width [mm]	Thickness [mm]
300	300	0.8

Table 5.7: Dimensions of the simulated plate subjected to blast loading

Test series	Blast load distance [mm]
A1x	375
A2x	500
A3x	625

Table 5.8: Blast load distances for test series A1x, A2x and A3x

5.4 Blast Loading on Plates

This case was modeled and simulated after experimental tests A1x, A2x and A3x in Aune et al. [14], where an explosive load of C4 was placed at various distances from a thin, clamped plate. Both steel and aluminum were used in the paper, but only the results from the aluminum plates will be considered in this thesis. By modeling this experiment with both an isotropic and a combined material hardening model, this case study hopes to reveal the consequence of involving kinematic hardening in a simulated blast loading.

5.4.1 Modeling

The plate was given the dimensions shown in Table 5.7 and clamped boundary conditions. It was meshed with 5 mm elements and the mesh is shown in Figure 5.26. The explosion was modeled as an air blast with the Conventional Weapons Effects Program (ConWep) function in Abaqus [39], to accurately simulate the experimental tests. Figure 5.27 shows a typical pressure, P, history used in the ConWep function, as measured at a standoff distance, i.e. measured at a distance from the explosion [39]. The figure depicts the delay from the detonation until the blast reaches the measuring point. It also shows the pressure from the explosion which consists of a large positive phase, reaching its maximum value at P_{max}, with exponential decline, followed by a negative phase. P_{atm} is the atmospheric pressure. The explosives were modeled as 41.2 g of TNT (40.2 g for the explosives and 1 g for the fuse) at the standoff distances listed in Table 5.8, for each test series.
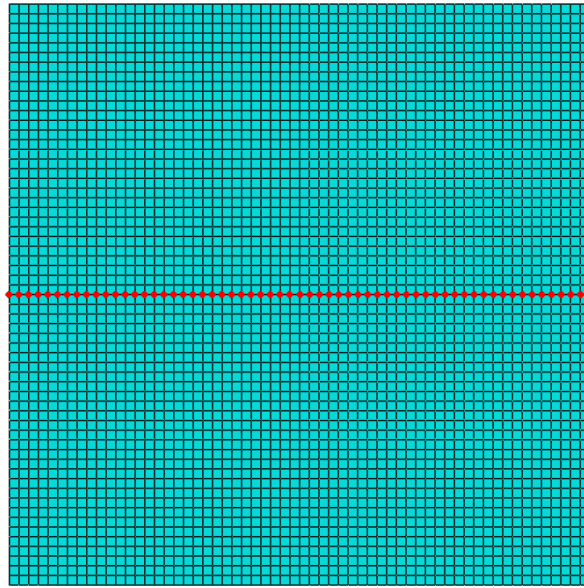
Figure 5.26: Mesh of plate subjected to blast loading with highlighted center line
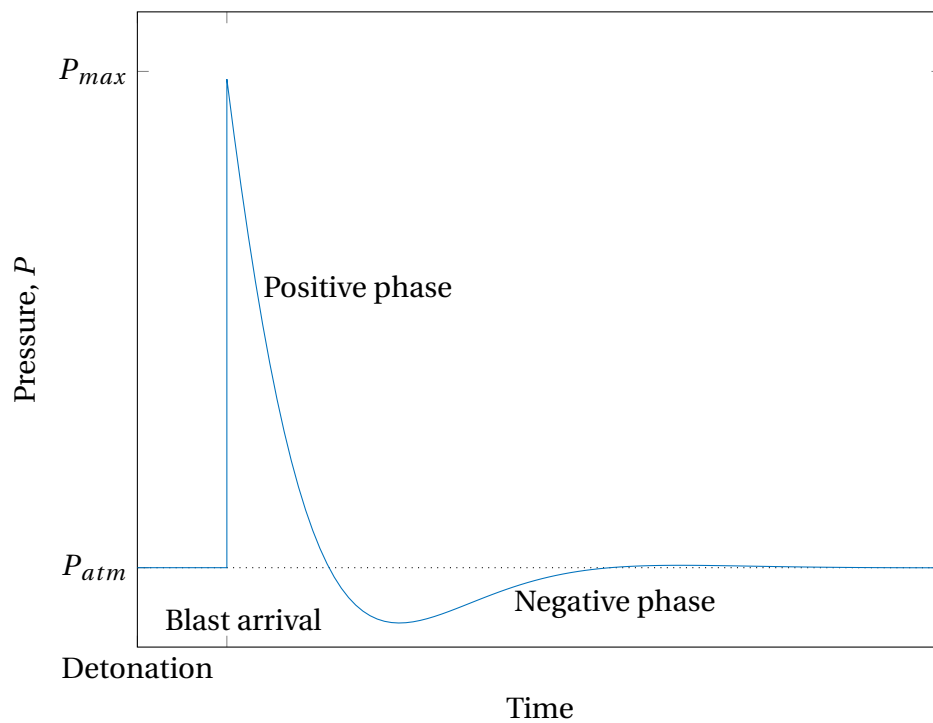
Figure 5.27: Plot showing the typical pressure history at a standoff distance for the ConWep function [39]

5.4.2 Results

The results in this case are presented as plots of displacement versus time for the center node in the plates as this is a good representation of the general response of the system. The displacement history is plotted for the entire x-axis to give better understanding of the overall shape of the plate during the blast. Figures from Abaqus depicting the equivalent plastic strain field of the final deformed shape are presented, to visualize the difference for tempers and material hardening models.

A typical displacement history of the center line in the plate during the positive phase of the explosion is shown in Figure 5.28. The center line is visualized in Figure 5.26. Each line in the plot represent the shape of the plate at specific times, from right after the arrival of the blast wave and until the negative phase has started. The traversing yield line can be observed traveling from the edge to the center of the plate in the figure. The same plot for the negative phase is shown in Figure 5.29 for test series A3x T6 with combined hardening, since this test has a unique response during this phase of the explosion. This figure shows how the center line of the plate is deformed when it is pulled back by the negative phase.

The maximum equivalent strain for the final deformed state is tabulated in Table 5.9 for all test series, tempers and material hardening models. These results show that T4, T6 and T7 have similar strain levels at a short standoff distance, while T4 has more strain than T6 and T7 at shorter distances. The equivalent plastic strain for the final deformed shape of A1x is shown in Figure 5.30, where it is evident that almost the entire plate has plastic deformation for all tempers. It is also evident that even though the maximum equivalent plastic strain in the center element are similar for all tempers, T4 has significantly more strain in the rest of the plate. The equivalent plastic strain for the final deformed state for all test series are shown in Section A.4.4 of the appendix.

Table 5.9 shows limited dispersion for equivalent plastic strain between the two hardening models. An exception is test series A1x T7, seen in Figures 5.30e and f, where the center element has considerable more equivalent plastic strain for the combined hardening model compared to the isotropic. The two material models have similar strain fields overall for T7 in this test series, but in the center of the plates the difference is 28 %. The maximum equivalent plastic strain is consistently higher for the combined hardening model compared to the isotropic model for temper T4. It is the exact opposite for tempers T6 and T7, where the isotropic model has the most equivalent plastic strain for all test series.
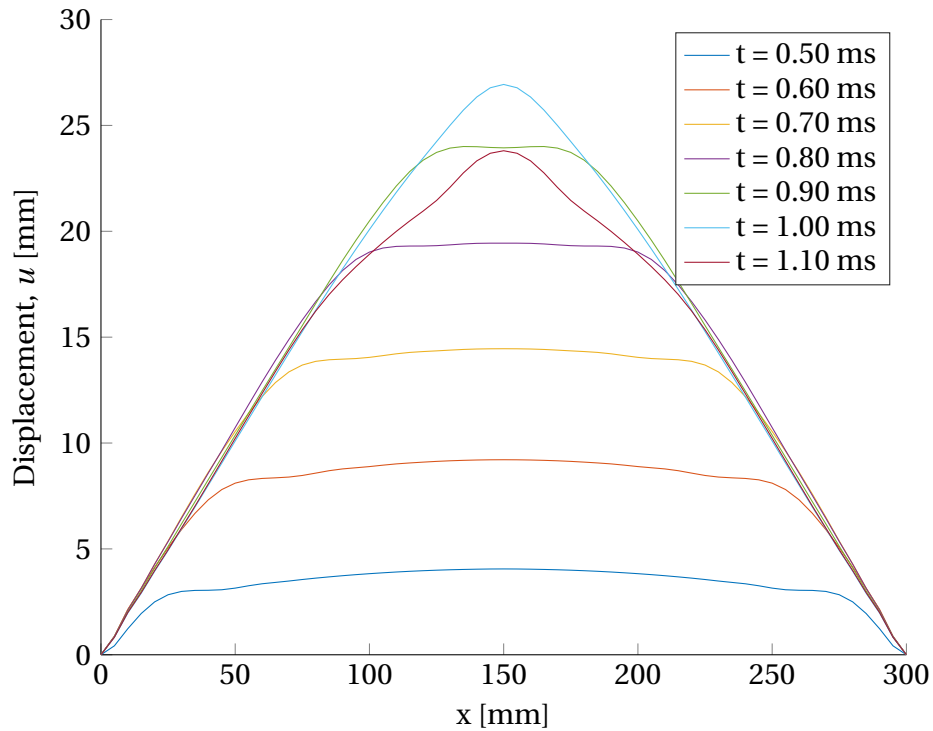
Figure 5.28: Deformation of the plate's center line along the x-axis at specified times for A2x T6 with combined hardening until the displacement starts to decrease
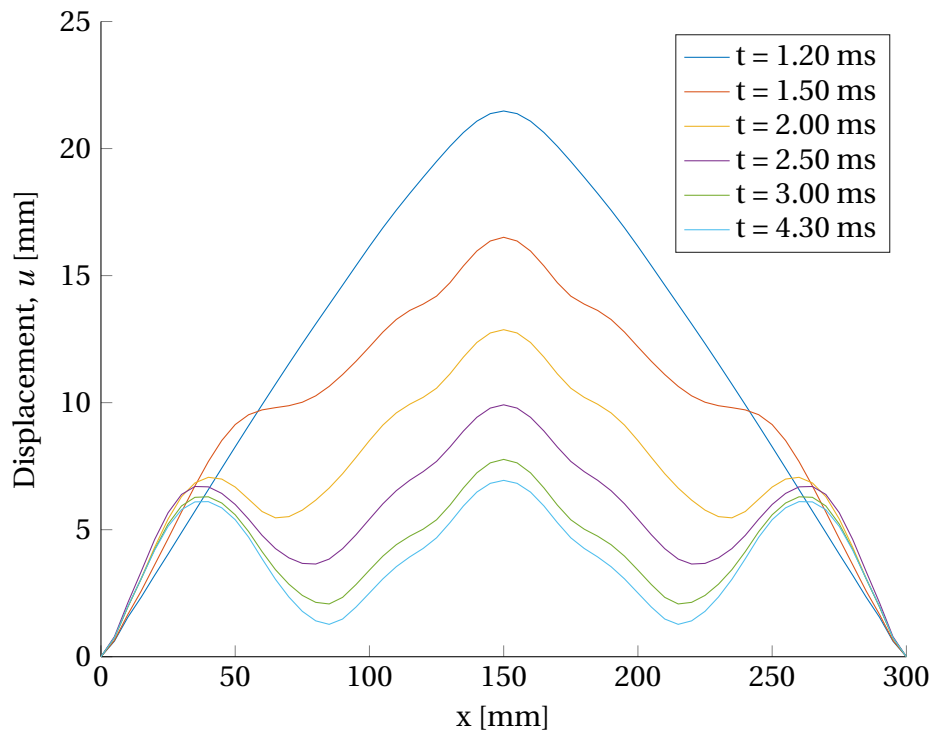
Figure 5.29: Deformation of the plate's center line along the x-axis at specified times for A3x T6 with combined hardening from displacement maximum at 1.2 ms to displacement minimum at 4.3 ms
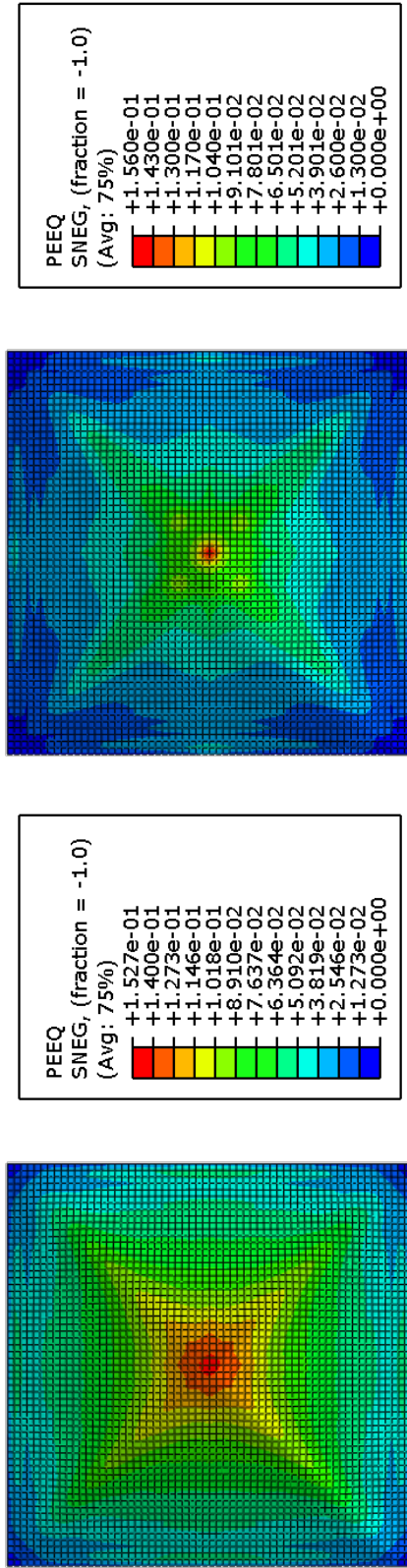
(a) T4 with combined hardening

(b) Color scheme for T4
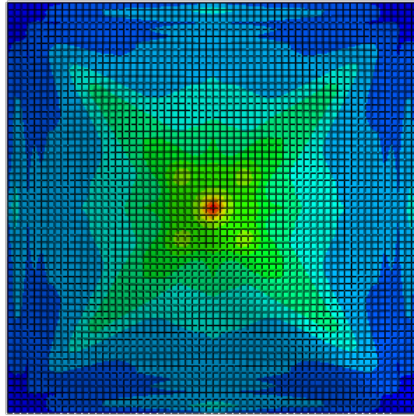
(c) T6 with combined hardening

(d) Color scheme for T6
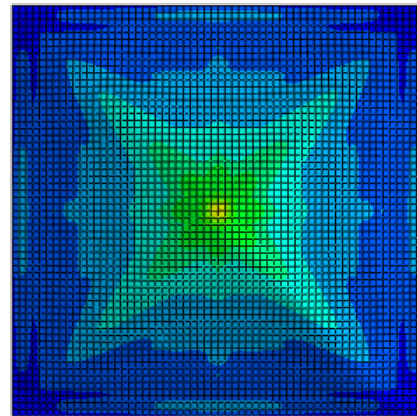
(e) T7 with isotropic hardening
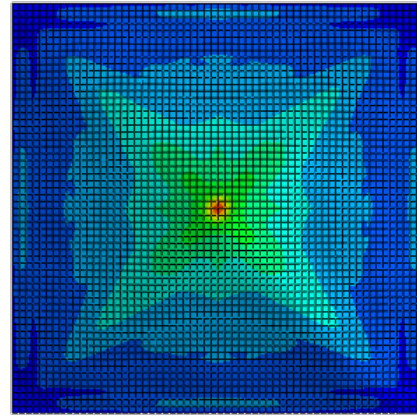
(f) T7 with combined hardening

(g) Color scheme for T7

Figure 5.30: The equivalent plastic strain field for the final deformed state for test series A1x

Test series	Temper	Maximum equivalent plastic strain, p	
		Isotropic hardening	Combined hardening
	T4	0.1527	0.1501
A1x	T6	0.1486	0.1560
	T7	0.1672	0.2071
	T4	0.1218	0.1101
A2x	T6	0.07536	0.07683
	T7	0.07828	0.08187
	T4	0.07021	0.06919
A3x	T6	0.04894	0.05045
	T7	0.05088	0.05269

Table 5.9: Maximum equivalent plastic strain in the model for the final deformed shape for blast loading

The plots depicting displacement versus time for the center node of the plate, shown in Figures 5.31 and 5.32, show large differences between the different tempers, especially for greater standoff distances. The response of T6 and T7 are highly dependent on the distance to the explosion, while the displacement plot for T4 has the same shape for all test series. T4 has no noteworthy oscillations and does not seem to be affected by the negative phase of the blast in the same way as seen for T6 and T7.

The explosion causes more displacement for the isotropic hardening model compared to the combined model in all test series and tempers, except for temper T4 in test series A1x where the two hardening model are indistinguishable. Even though the difference was only about 1 mm at the most, this can constitute a considerable amount as it corresponds to approximately 5 % of the total displacement for test series A3x T7. The difference observed between the two hardening models vary with both temper and explosion offset. For T4 the difference is almost unnoticeable for all test series, while the hardening models show distinguishable displacement for T6 and T7. There seems to be a trend towards greater difference between the hardening models for increasing charge standoff distances for these two tempers.

The experimental displacement versus time from Aune et al. [14] are shown in Figure 5.33. The displacement plots in Figure 5.31 and Figure 5.32a are similar in shape to the response of the experimental tests A11, A12 and A13 in Figure 5.33, while Figure 5.32c is almost identical to the displacement of the experimental tests A21 and A22. The reversed snap-buckling seen in experimental tests A31 and A33 was not recreated, but T6 A3x shows a clear tendency towards this behavior, with a maximum displacement of about 22 mm and a minimum displacement during the negative phase of about 8 mm. It should be noted that the aluminum alloy used in Aune et al. [14] has a yield stress of approximately 130 MPa and insignificant work hardening. The simulations also assume a perfectly clamped plate, while the plates in the experiments were only approximately clamped.
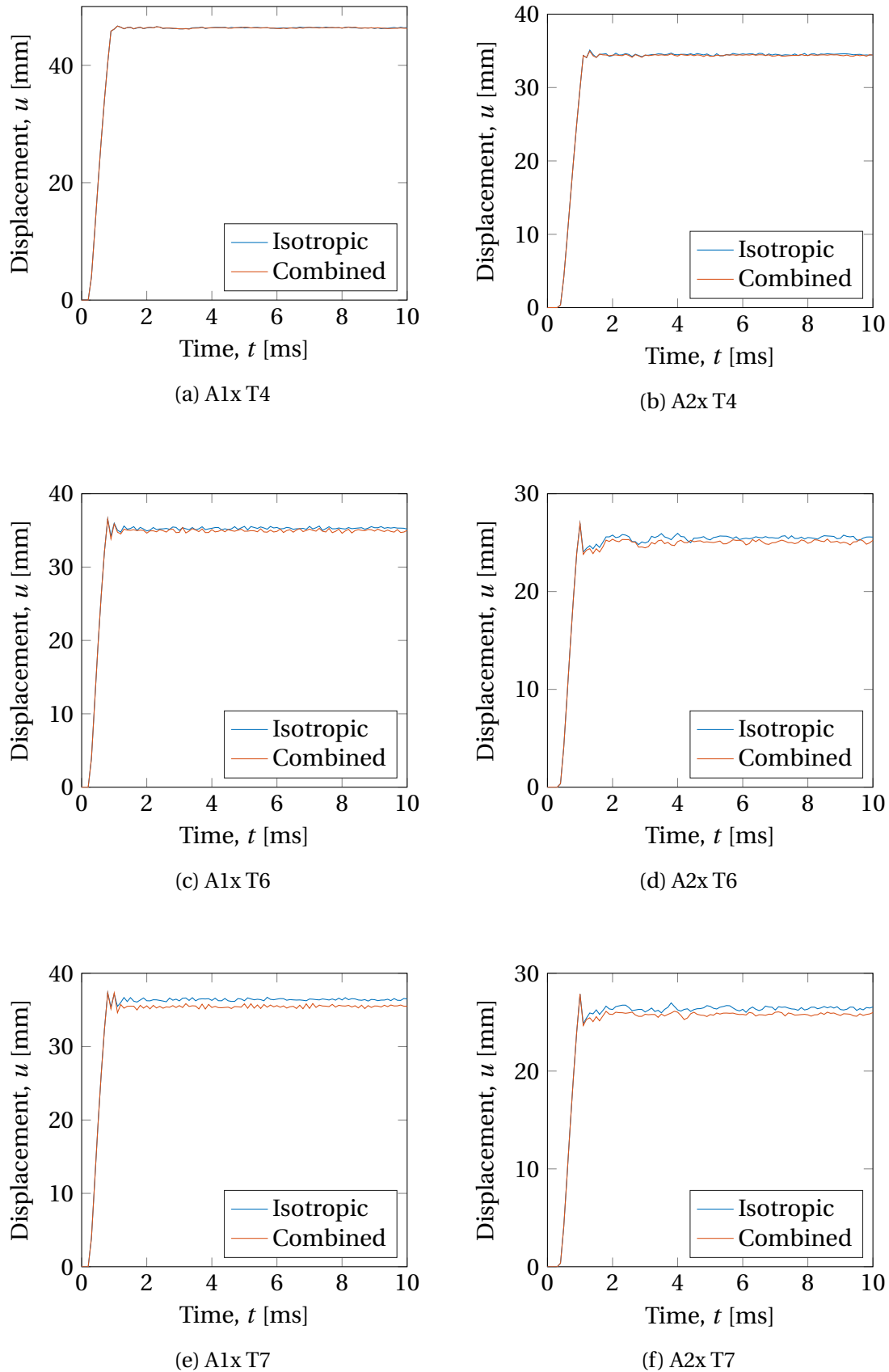
Figure 5.31: Displacement versus time in the center node for blast loading on plate. Test series A1x (left) and A2x (right) with isotropic and combined material hardening models
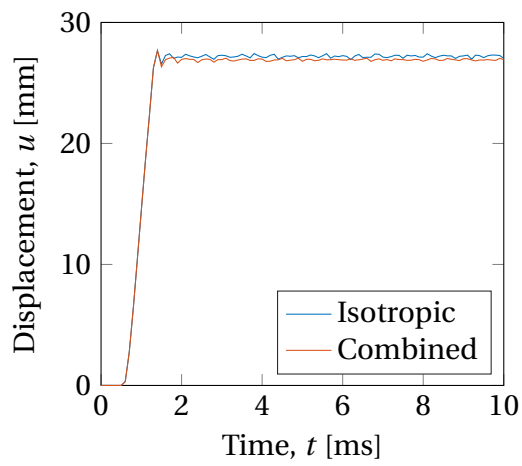
(a) A3x T4
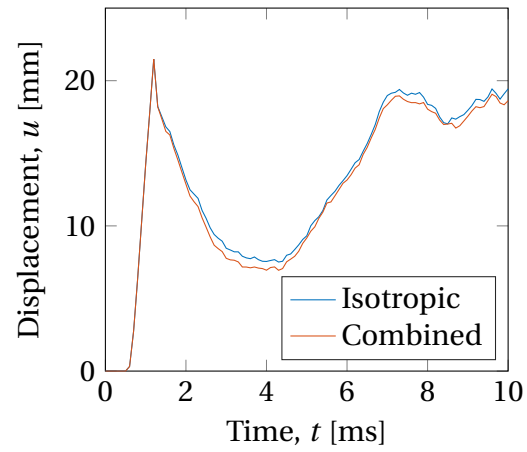
(b) A3x T6
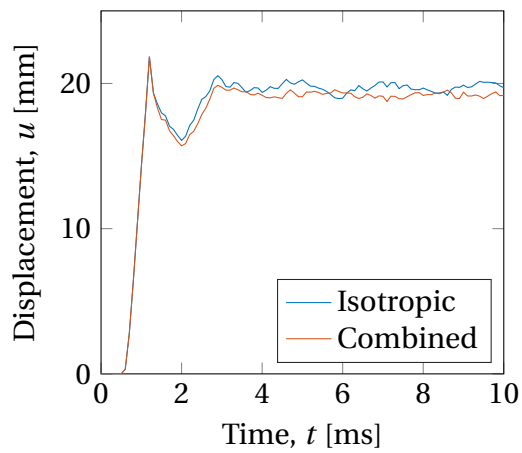
(c) A3x T7

Figure 5.32: Displacement versus time in the center node for blast loading on plate. Test series A3x with isotropic and combined material hardening models
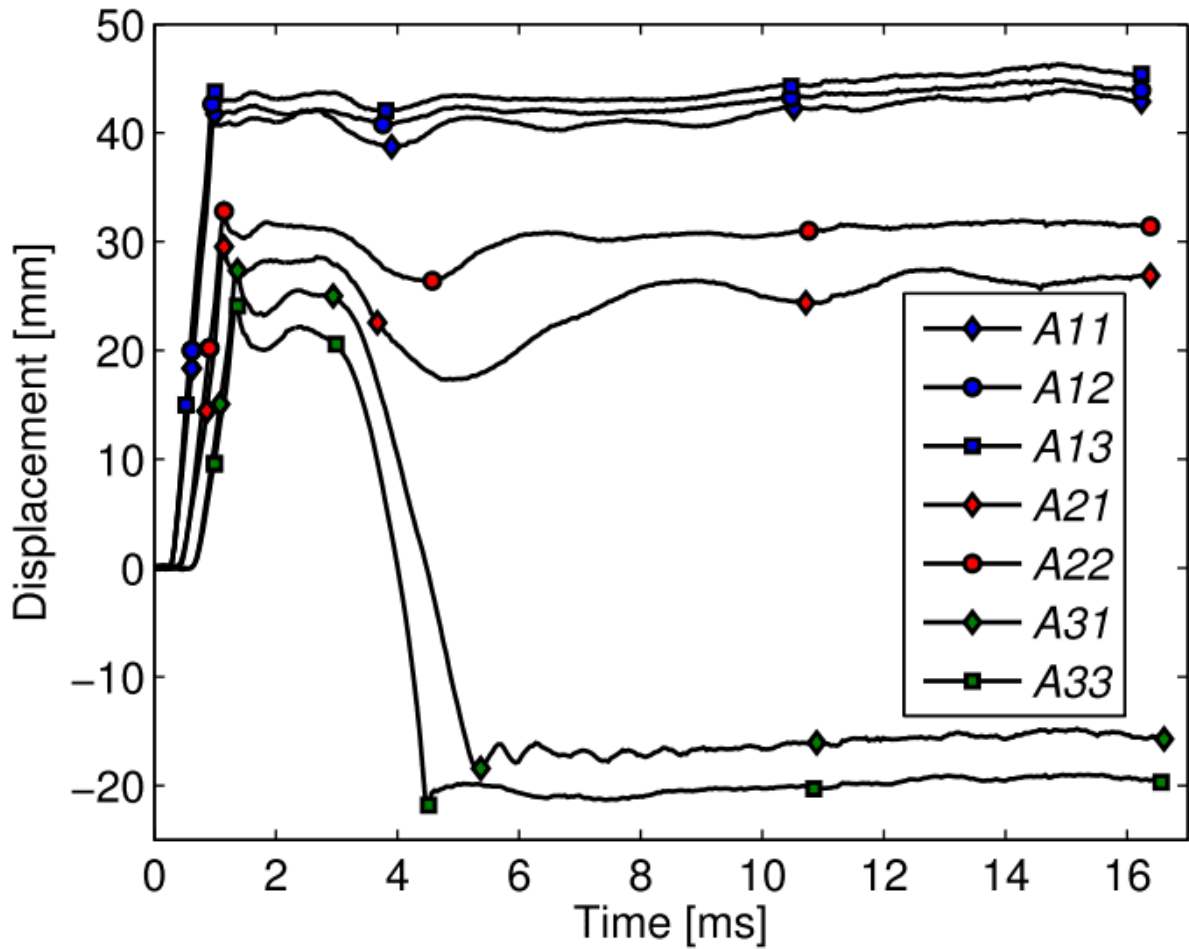
Figure 5.33: Deformation versus time for center point of the plate, taken from Aune et al. [14]. "A" in Axx denotes aluminum alloy AA1050A H14, the first digit denotes the standoff distances showed in Table 5.8 and the last digit denotes test number

5.4.3   Discussion

As observed here and in the other case studies of this thesis, the difference between hardening models is most prominent during fluctuating stress states. Temper T4 has only minor oscillations in all test series and neither of them has any distinction between the hardening models. T6 and T7 on the contrary show more oscillations and more distinctive responses from the isotropic and combined material hardening models than T4. The greatest distinction between the hardening models was seen for A3x T7 where the difference was about 5 % at the most.

An interesting note is that the center node for isotropic hardening has slightly more displacement and at the same time lower maximum equivalent plastic strain, compared the the combined hardening, for all test series in tempers T6 and T7. The reason for this is uncertain, but the combined model may cause more concentrated deformations from possible localized stress state fluctuations, causing high local strains but less total displacement.

T4 does not seem to be affected by the negative phase of the explosion, as opposed to T6, T7 and AA1050A H14. This may be cause by the fact that T4 has a lower yield stress and more work hardening than either of these.

6 | Concluding Remarks

As a concluding chapter of this thesis, remarks are given on the methods used and results obtained for the literature study, the experimental study, the material processing and the simulated numerical cases. Finally, suggestions for future work on this topic are given.

The literature study has been an immense tool to help understand key theoretical aspects of material mechanics. It is regrettable that the theory does not go into more details, but the theory provided here is considered to be adequate for understanding the principles at work in this thesis.

The experimental results of this thesis are considered somewhat unusual due to the wide variation of the yield stresses and material behavior within each temper. This might be due to the lower temperature used in the solution heat treatment of the specimens compared to Westermann et al. [27]. It was attempted to correct this anomaly with a yield stress normalization before the material parameters were calibrated. The effects of these alterations are uncertain and further work on this topic should take this into account when comparing results and conclusions. The load sequence of the tensile tests were concluded to be insignificant for the work hardening of the alloy by the experimental results.

A small selection of methods were used to identify material parameters such as the yield stress and for calibrating isotropic and combined isotropic-kinematic material hardening models. For the yield stress identification a Voce equation was curve fit to the material data provided results with minimal dispersion. A reduced-parameters method taken from Tarigopula et al. [10] proved the most promising for describing the combined hardening model, with acceptable estimates for the load reversal tensile tests. It should be noted that this method was somewhat time consuming to implement and the other method considered in this thesis, taken from Manes et al. [11], would be preferred if the amount of tensile tests were increased, as this is considered the simpler method and faster to implement.

The kinematic contribution to the work hardening for all tempers increased rapidly and saturated at a low plastic strain compared to the more gradual work hardening contributed by the isotropic hardening. A trend towards the kinematic contribution increasing less rapidly and saturate at higher plastic strains, as the temper number increased, was observed from the experimental data.

From the case studies, only minor differences between the two material hardening models were found for all tempers. However, when comparing each temper it was found that T4 showed a different structural response with a more uniform strain distribution for all cases compared to T6 and T7, which showed similar responses to each other. This distribution was seen to cause a lower maximum equivalent strain in the numerical model and a reduced chance of fracture. This is most likely due to the lower yield stress and the considerable work hardening of the T4 temper.

For some cases there was no noticeable difference between the two hardening models. This is most likely attributed to the limited fluctuations of the stress states in the case studies. One of the consistent results found in this thesis is a distinction between isotropic and combined hardening when a material undergoes considerable fluctuating stress states, as the theory predicts. From this it can be concluded that for simulation models without fluctuating stress states it is not worth the extra time and cost to calibrate a combined hardening model. In a model where fluctuating stress states might be suspected, it may be wise to investigate the significance of including kinematic hardening in the material model.

6.1 Further Work

As the tensile tests showed variation in both yield stress and work hardening within each temper, it would be interesting to repeat the experimental study with the specimens heat treated exactly as in Westermann et al. [27].

Seeing as this thesis has only assessed the impact of including kinematic hardening in aluminum alloy AA6060, the next step could be to investigate this effect in different aluminum alloys or steels.

Another possible addition to this thesis would be to examine the transition of when kinematic hardening should be included and when it could be neglected. This would require a study with cases undergoing a variety of load patterns or fluctuating stress states.

A possibility for further work is to include kinematic hardening in the Nano Structure Model (NaMo) developed from Myhr et al. [7]. This would make it possible to describe the kinematic hardening based on the temperature history of the material, which would reduce the need for reversed loading or cyclic material tests. However, this would require further analysis of the physically-based models and theory related to kinematic hardening.

It would be interesting to be able to see the path of the stress in 3D stress space as a function of time, and the evolution of the yield surface. This could prove to be an immense asset for identifying fluctuating or cyclic stress states, suggesting kinematic hardening should be considered.

References

[1] O. S. Hopperstad and T. Børvik. Material Mechanics Part I, 2015. Structural Impact Laboratory, NTNU.

[2] J. Bauschinger. Über die veranderung der elasticitätsgrenze und des elasticitätsmodulus verschiedener metalle. *Zivilingenieur*, 27:289–348, 1881.

[3] Q. Zhao and B. Holmedal. Modelling work hardening of aluminium alloys containing dispersoids. *Philosophical Magazine*, 93(23):3142–3153, 2013.

[4] E. Voce. The relationship between stress and strain for homogeneous deformation. *Journal of the Institute of Metals*, 74:537–562, 1948.

[5] P.J. Armstrong and C.O. Frederick. A mathematical representation of the multiaxial Bauschinger effect. *Technical Report RD/B/N 731*, 1966.

[6] J.L. Chaboche. Time-Independent Constitutive Theories for Cyclic Plasticity. *International Journal of Plasticity*, 2(2):149–188, 1986.

[7] O.R. Myhr, Ø. Grong, and K.O. Pedersen. A Combined Precipitation, Yield Strength, and Work Hardening Model for Al-Mg-Si Alloys. *Metallurgical and Materials Transactions A*, 41(9):2276–2289, 2010.

[8] O.S. Hopperstad, M. Langseth, and S.Remseth. Cyclic Stress-Strain Behaviour of Alloy AA6060, Part I: Uniaxial Experiments and Modelling. *International Journal of Plasticity*, 11(6):725–739, 1995.

[9] K.M. Zhao and J.K. Lee. Material Properties of Aluminum Alloys for Accurate Draw-Bend Simulation. *Journal of Engineering Materials and Technology*, 123(3):287–292, 2001.

[10] V. Tarigopula, O.S. Hopperstad, M. Langseth, and A.H. Clausen. Elastic-plastic behaviour of dual-phase, high-strength steel under strain-path changes. *European Journal of Mechanics - A/Solids*, 27(5):764–782, 2008.

[11] A. Manes, R. Porcaro, H. Ilstad, E. Levold, M. Langseth, and Tore Børvik. The behaviour of an offshore steel pipeline material subjected to bending and stretching. *Ships and Offshore Structures*, 7(4):371–387, 2012.

[12] N. H. Hoang, O. S. Hopperstad, O. R. Myhr, C. Marioara, and M. Langseth. An improved nano-scale material model applied in axial-crushing analyses of square hollow section aluminium profiles. *Thin-Walled Structures*, 92:93–103, 2015.

[13] M. Langseth, O.S. Hopperstad, and T. Berstad. Impact Loading of Plates: Validation of Numerical Simulations by Testing. *International Journal of Offshore and Polar Engineering*, 9(1), 1999.

[14] V. Aune, E. Fagerholt, K.O. Hauge, M. Langseth, and T. Børvik. Experimental study on the response of thin aluminium and steel plates subjected to airblast loading. *International Journal of Impact Engineering*, 90:106–121, 2016.

[15] Y. Chen, A.H. Clausen, O.S. Hopperstad, and M. Langseth. Stress–strain behaviour of aluminium alloys at a wide range of strain rates. *International Journal of Solids and Structures*, 46(21):3825–3835, 2009.

[16] J.A. Zukas, T. Nicholas, H.F. Swift, L.B. Greszczuk, and D.R. Curran. *Impact Dynamics*. Krieger Publishing Company, 1992.

[17] K.G. Rakvåg, T. Børvik, and O.S. Hopperstad. A Numerical Study on the Deformation and Fracture Modes of Steel Projectiles During Taylor Bar Impact Tests. *International Journal of Solids and Structures*, 51(3-4):808–821, 2014.

[18] P.W. Bridgman. *Transactions of the American Society for Metals*, volume 32. American Society for Metals, 1944.

[19] G. Le Roy, J.D. Embury, G. Edwards, and M.F. Ashby. A Model of Ductile Fracture Based on the Nucleation and Growth of Voids. *Acta Metallurgica*, 29(8):1509–1522, 1981.

[20] P.M. Dixit and U.S. Dixit. *Modeling of Metal Forming and Machining Processes*. Springer-Verlag London, 2008.

[21] M.G. Cockcorft and D.J. Latham. Ductility and the Workability of Metals. *Journal of the Institute of Metals*, 96(1):33–39, 1968.

[22] G. Gruben, E. Fagerholt, O.S. Hopperstad, and T. Børvik. Fracture Characteristics of a Cold-Rolled Dual-Phase Steel. *European Journal of Mechanics - A/Solids*, 30(3):204–218, 2011.

[23] W. Lode. Versuche über den Einfluß der mittleren Hauptspannung auf das Fließen der Metalle Eisen, Kupfer und Nickel. *Zeitschift für Physik*, 36(11):913–939, 1926.

[24] European Aluminium Association and MATTER. aluMATTER. http://aluminium.matter.org.uk [cited: 26.02.2016].

[25] J.E. Hatch. *Aluminum : Properties and Physical Metallurgy*. ASM International, 1984.

[26] ASM International Handbook Committee. *ASM Handbook Volume 2: Properties and Selection: Nonferrous Alloys and Special-Purpose Materials*. ASM International, 10th edition, 1990.

[27] I. Westermann, K. O. Pedersen, T. Furu, T. Børvik, and O. S. Hopperstad. Effects of particles and solutes on strength, work-hardening and ductile fracture of aluminium alloys. *Mechanics of Materials*, 79:58–72, 2014.

[28] I. Westermann, K. O. Pedersen, T. Børvik, and O. S. Hopperstad. Work-hardening and ductility of artificially aged AA6060 aluminium alloy. *Mechanics of Materials*, 97:100–117, 2016.

[29] Dassault Systèmes. Abaqus Standard/Explicit 2014. http://www.3ds.com/products-services/simulia/products/abaqus/ [cited: 08.04.2016].

[30] Dassault Systèmes. Abaqus Theory Guide 4.3.5, 2014.

[31] ABAQUS, Inc. Lecture 5, Quasi-Static Analyses, . http://imechanica.org/files/l5-quasi-static.pdf [cited: 20.05.2016].

[32] P.G. McCormick. The Portevin-Le Chatelier effect in an Al-Mg-Si alloy. *Acta Metallurgica*, 19(5):463–471, 1971.

[33] MathWorks. MATLAB R2015a. http://se.mathworks.com/products/matlab/ [cited: 08.04.2016].

[34] H. Proudhon, W.J. Poole, X. Wang, and Y. Bréchet. The role of internal stresses on the plastic deformation of the Al-Mg-Si-Cu alloy AA6111. *Philosophical Magazine*, 88(5): 621–640, 2008.

[35] G. Fribourg, Y. Bréchet, A. Deschamps, and A. Simar. Microstructure-based modelling of isotropic and kinematic strain hardening in a precipitation-hardened aluminium alloy. *Acta Materialia*, 59(9):3621–3635, 2011.

[36] O.S. Hopperstad, M. Langseth, and T. Børvik. Analysis of the Cockcroft-Latham and maximum shear stress criteria for ductile fracture of metals. *Technical Report*, page 7, 2006.

[37] ABAQUS, Inc. Lecture 2, Elements, . `http://imechanica.org/files/l2-elements.pdf` [cited: 12.04.2016].

[38] M. Seitzberger, F.G. Rammerstorfer, and H.P. Degischer. Crushing of axially compressed steel tubes filled with aluminium foam. *Acta Mechanica*, 125(1):93–105, 1997.

[39] Dassault Systèmes. Abaqus Analysis User's Guide 34.4.6, 2014.

A | Additional Plots, Figures and Tables

A.1   Yield Stress

Temper	Load sequence	No.	Yield stress [MPa]		
			Method 1	Method 2	Method 3
T4	Tension	1	67.26	72.10	62.00
		2	56.52	61.59	52.36
	Tension - compression	1	48.02	50.16	45.00
		2	42.17	49.67	45.00
		3	65.76	68.19	52.48
		4	53.06	52.80	53.30
		5	59.05	56.81	55.95
	Compression - tension	1	61.82	57.29	45.00
		2	62.30	48.61	45.96
		3	57.18	49.52	45.00
		4	50.66	49.68	49.34
		5	52.13	47.39	47.72
T6	Tension	1	109.1	140.7	130.9
		2	122.4	137.7	90.49
	Tension - compression	1	119.0	127.3	80.90
		2	131.9	138.9	80.47
		3	123.9	132.6	101.2
		4	132.4	131.6	86.05
		5	131.2	130.1	111.5
	Compression - tension	1	114.3	112.7	80.00
		2	136.5	141.6	104.2
		3	148.0	142.2	102.0
		4	120.7	123.0	92.75
		5	119.1	115.2	104.4
T7	Tension	1	136.8	135.3	125.1
		2	122.1	127.6	117.0
	Tension - compression	1	131.7	128.6	80.00
		2	127.5	131.2	95.59
		3	126.2	130.8	102.7
		4	117.8	129.5	88.34
		5	138.0	136.3	115.3
	Compression - tension	1	130.6	129.0	80.00
		2	125.4	130.2	96.46
		3	116.9	129.8	80.00
		4	122.0	128.1	80.00
		5	136.5	133.6	84.37

Table A.1: Yield stress calculation results for each individual tensile test

A.2 Material Parameter Estimates
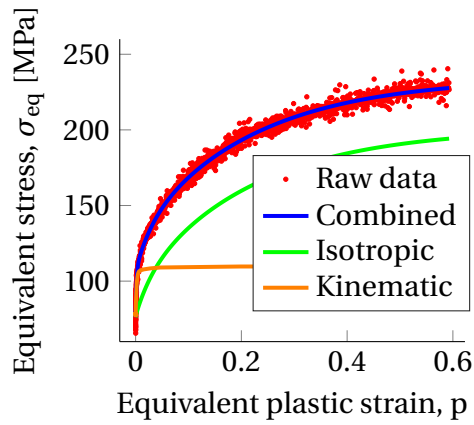
(a) T4 tension no. 1
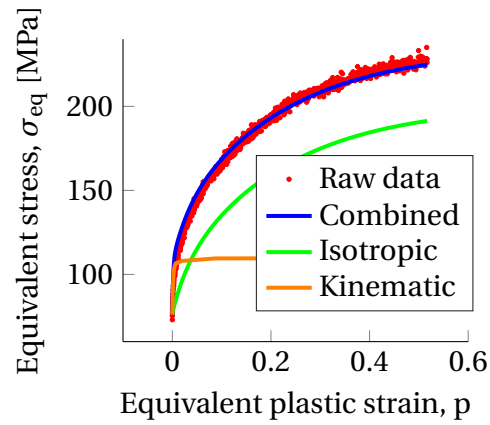
(b) T4 tension no. 2
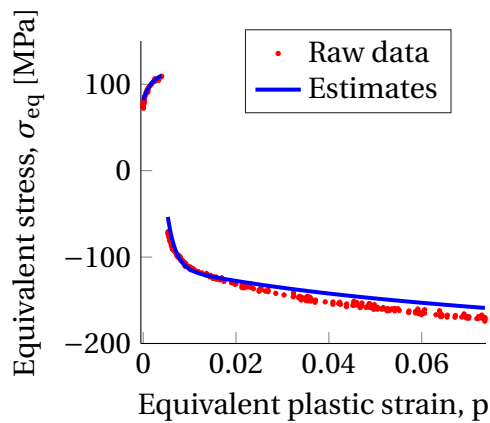
(c) T4 tension-compression no. 1
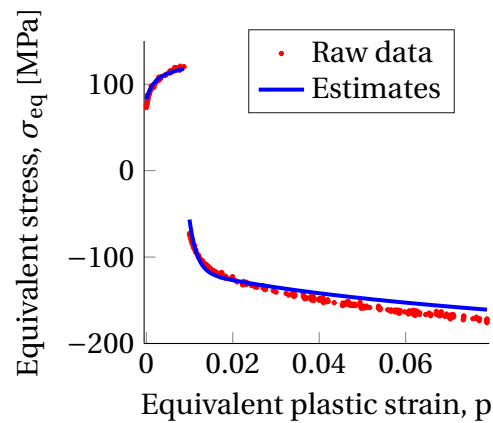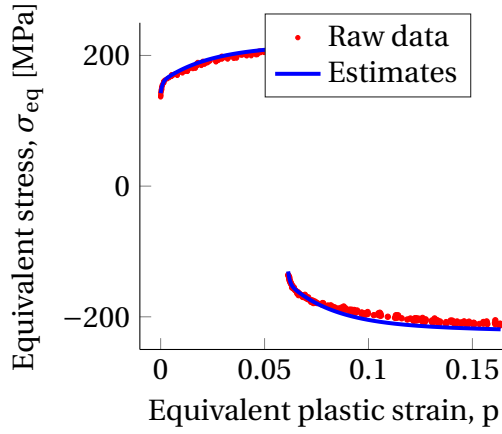
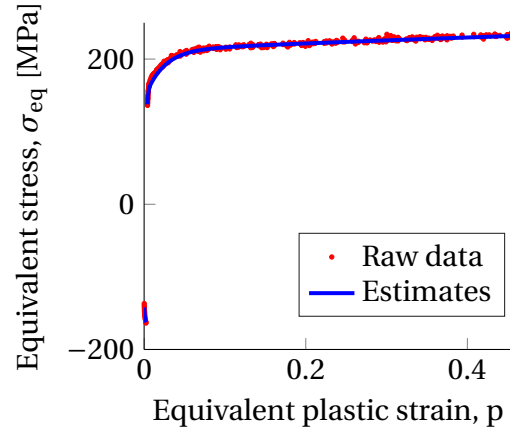(d) T4 tension-compression no. 2
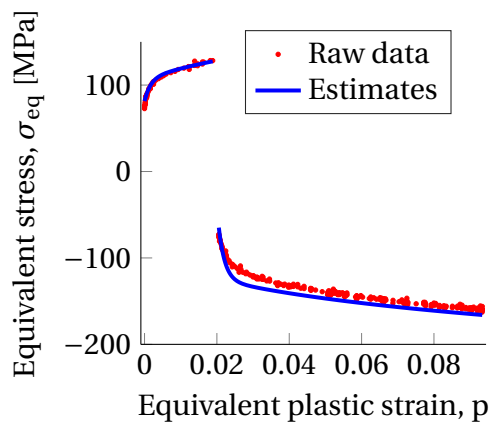
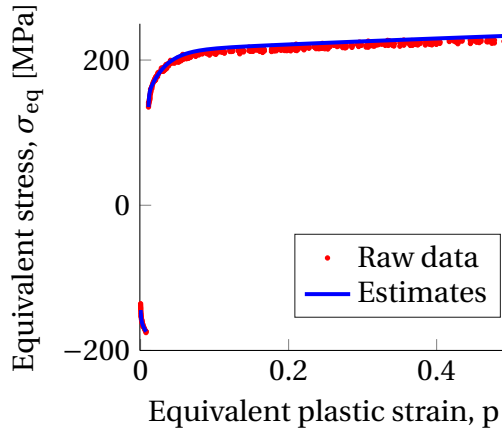(e) T4 tension-compression no. 3
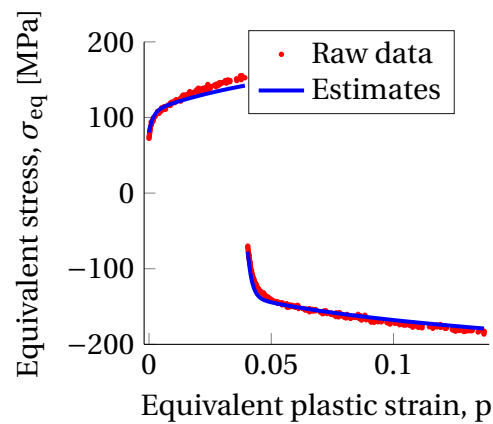
(f) T4 tension-compression no. 4

Figure A.1: Plot of the raw data and the material parameter estimate by the backstress calculation Method B for T4 tensile tests, plot 1
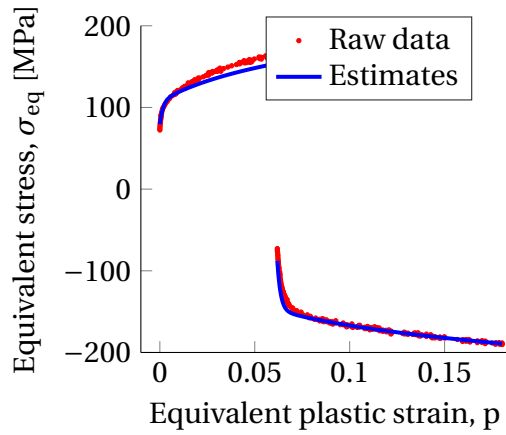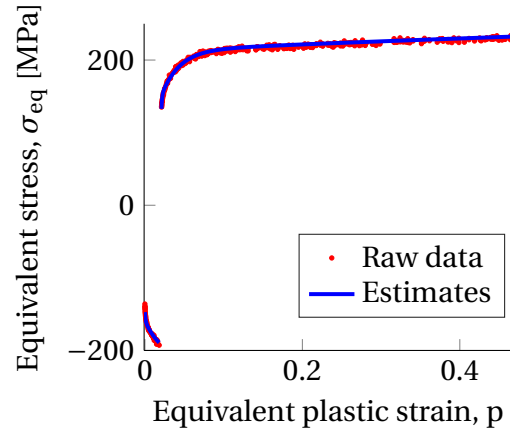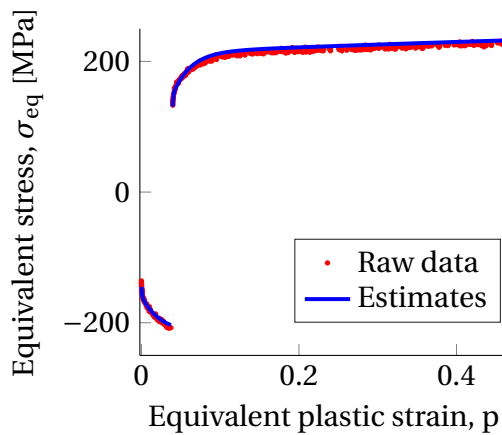
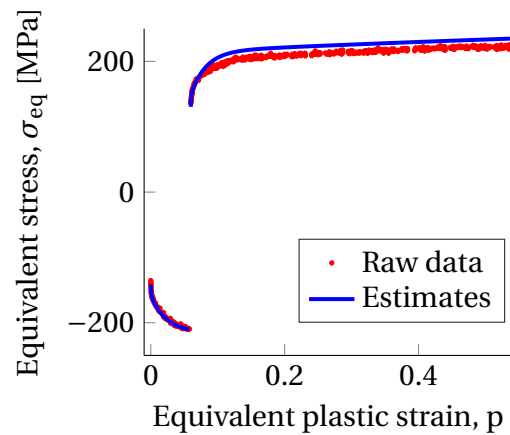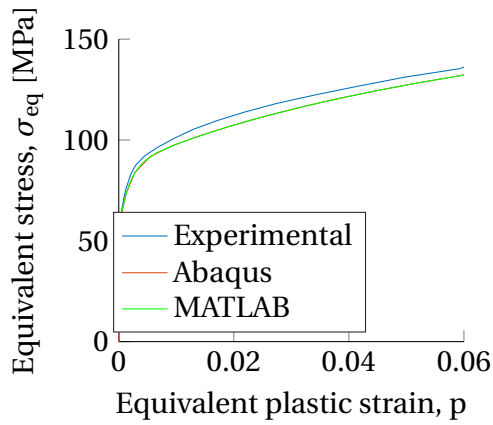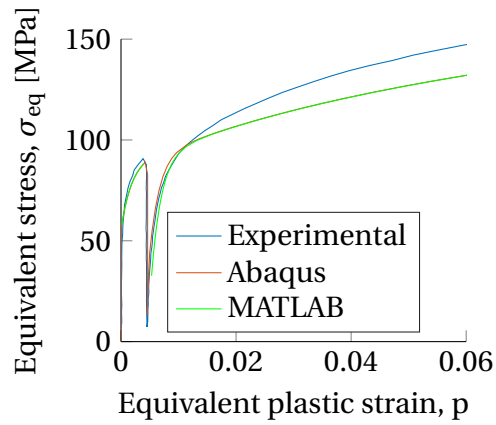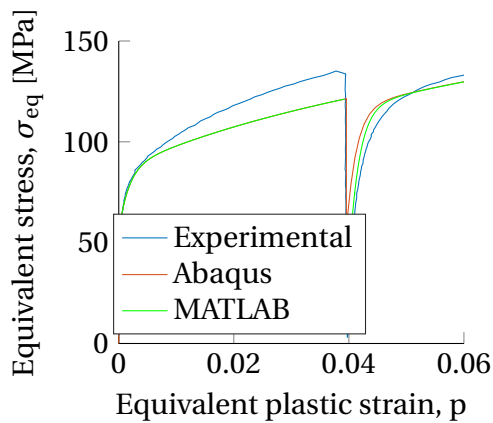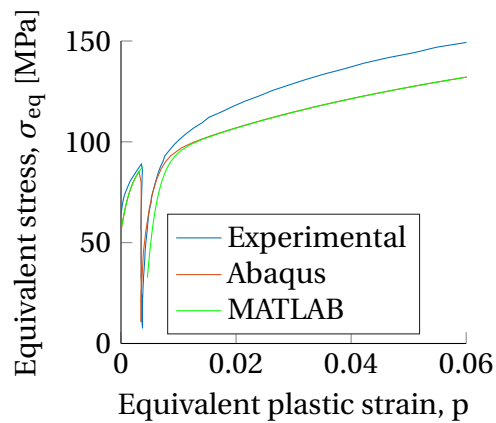(a) T4 tension-compression no. 5
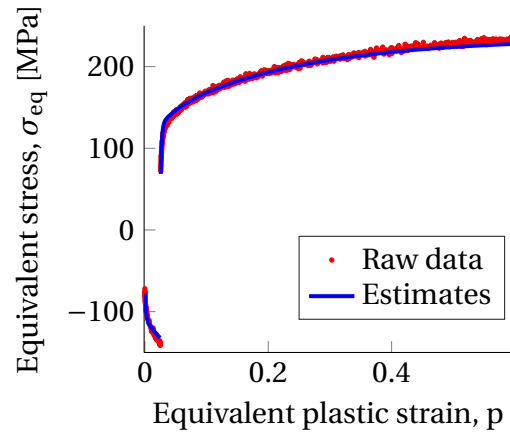
(b) T4 compression-tension no. 1
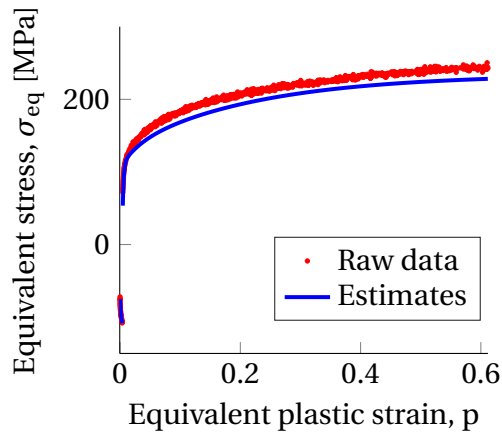
(c) T4 compression-tension no. 2
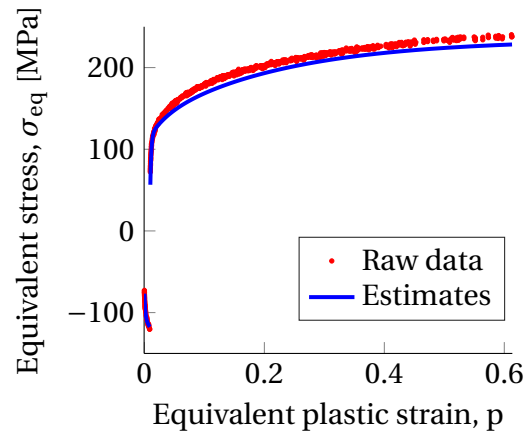
(d) T4 compression-tension no. 3
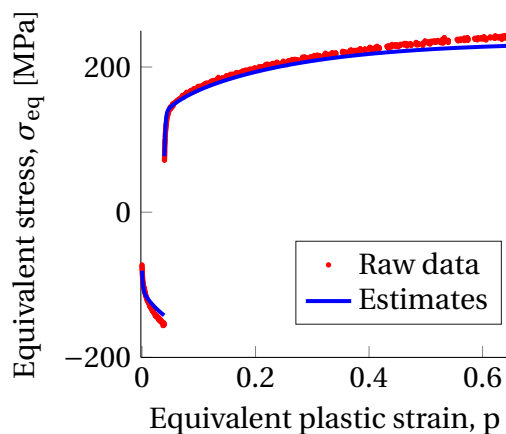
(e) T4 compression-tension no. 4
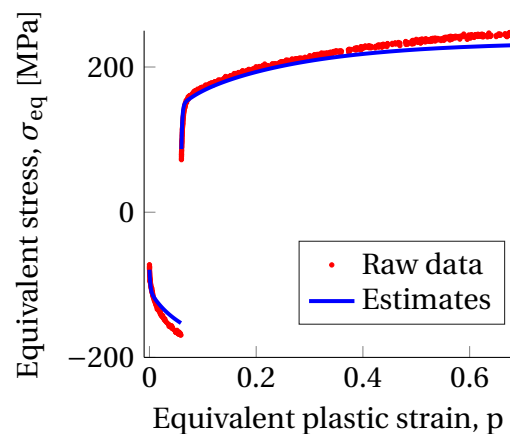
(f) T4 compression-tension no. 5

Figure A.2: Plot of the raw data and the material parameter estimate by the backstress calculation Method B for T4 tensile tests, plot 2
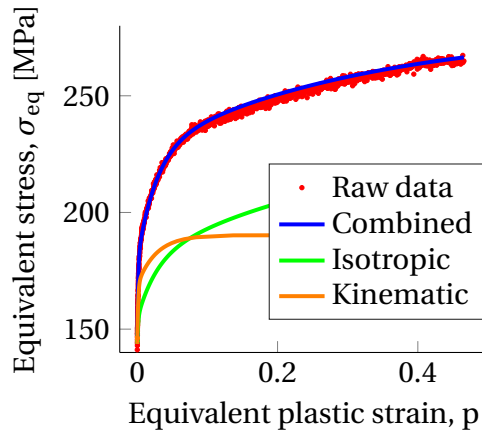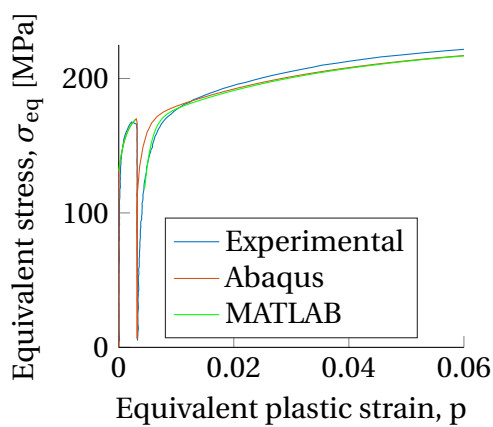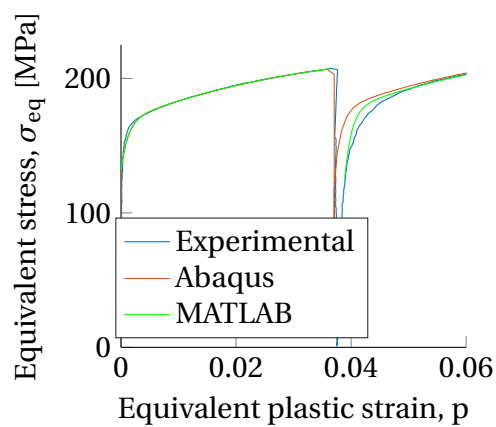
(a) T6 tension no. 1
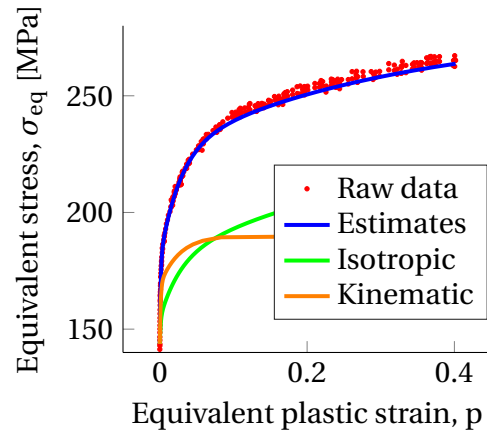
(b) T6 tension no. 2
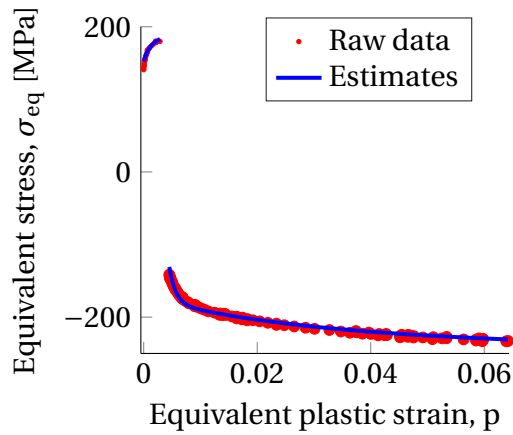
(c) T6 tension-compression no. 1
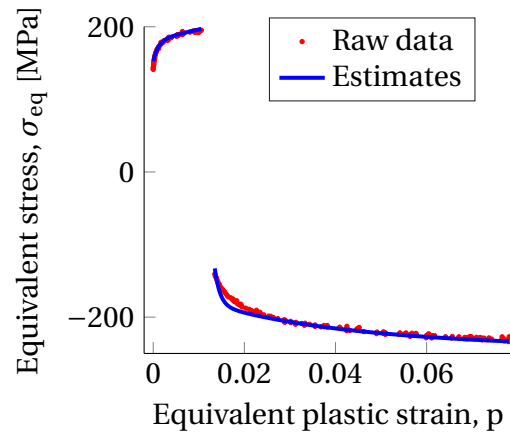
(d) T6 tension-compression no. 2
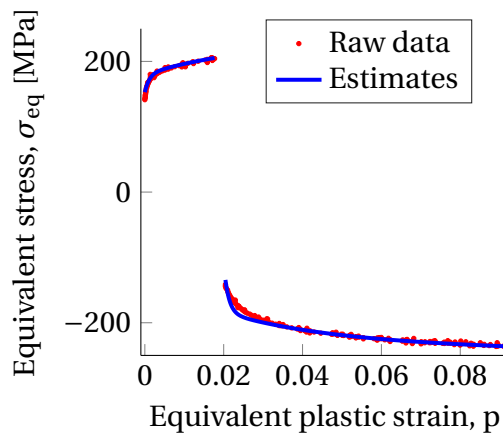
(e) T6 tension-compression no. 3
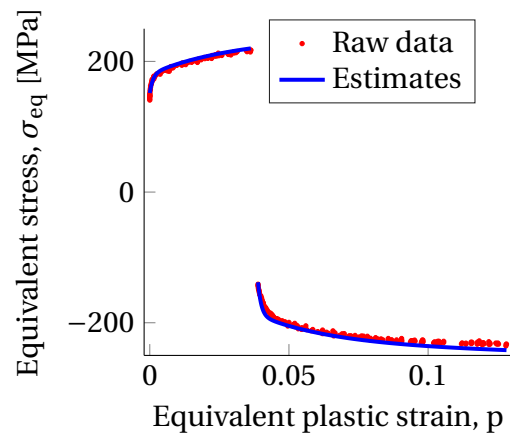
(f) T6 tension-compression no. 4

Figure A.3: Plot of the raw data and the material parameter estimate by the backstress calculation Method B for T6 tensile tests, plot 1
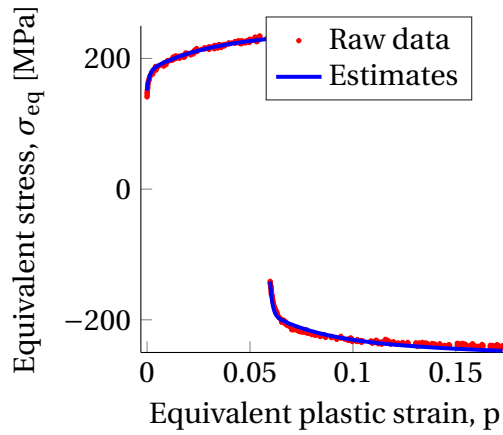
(a) T6 tension-compression no. 5
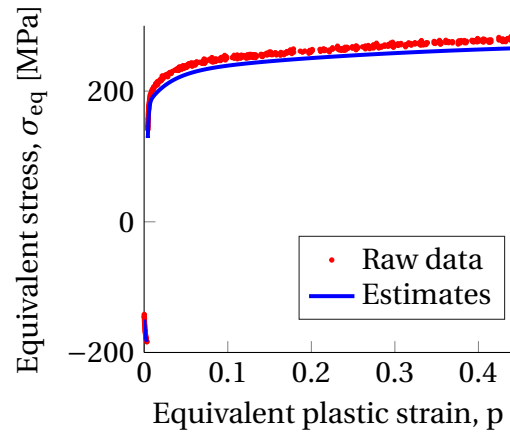
(b) T6 compression-tension no. 1
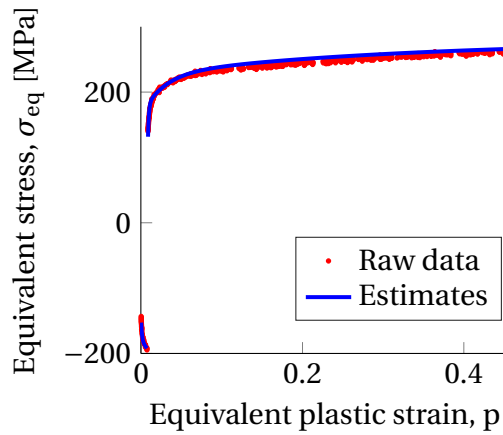
(c) T6 compression-tension no. 2
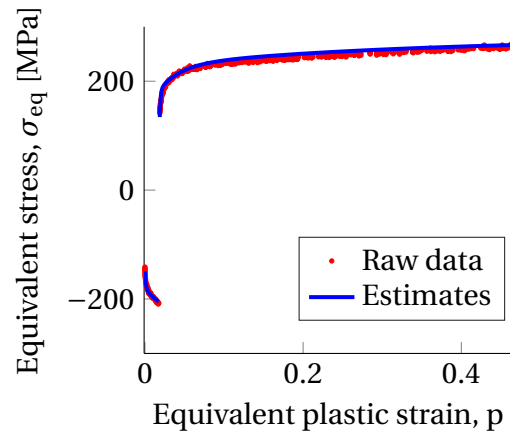
(d) T6 compression-tension no. 3
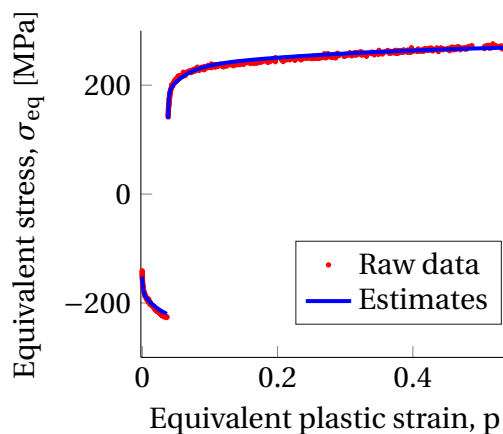
(e) T6 compression-tension no. 4
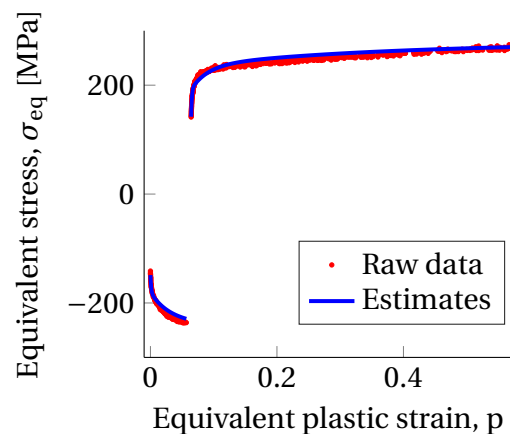
(f) T6 compression-tension no. 5

Figure A.4: Plot of the raw data and the material parameter estimate by the backstress calculation Method B for T6 tensile tests, plot 2
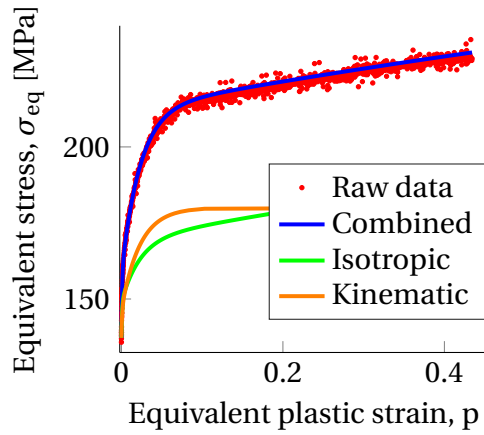
(a) T7 tension no. 1
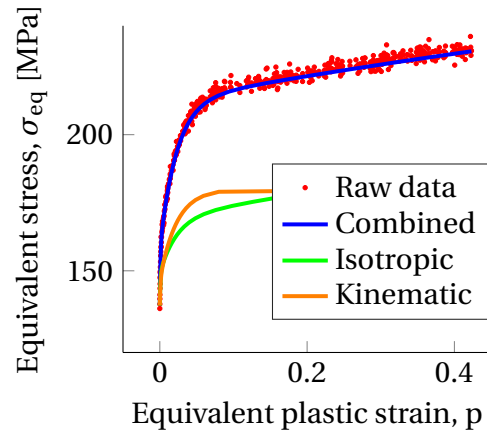
(b) T7 tension no. 2
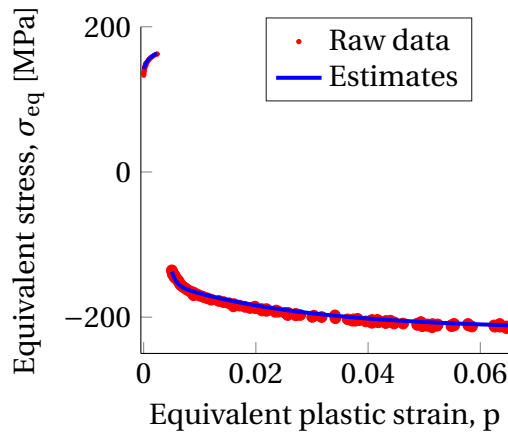
(c) T7 tension-compression no. 1
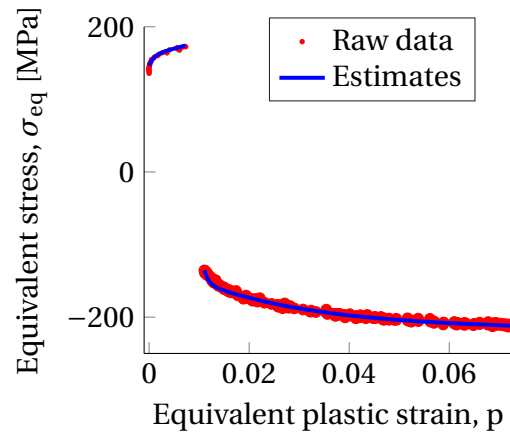
(d) T7 tension-compression no. 2
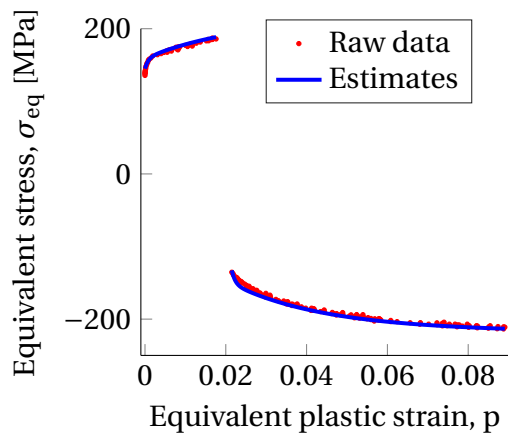
(e) T7 tension-compression no. 3
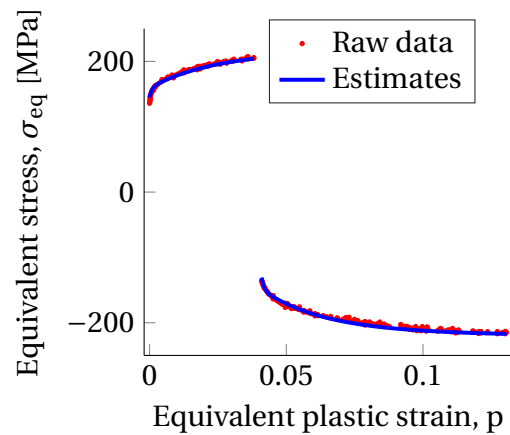
(f) T7 tension-compression no. 4

Figure A.5: Plot of the raw data and the material parameter estimate by the backstress calculation Method B for T7 tensile tests, plot 1

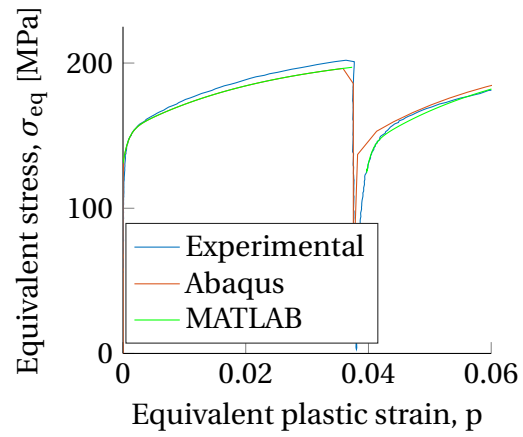(a) T7 tension-compression no. 5

(b) T7 compression-tension no. 1

(c) T7 compression-tension no. 2

(d) T7 compression-tension no. 3

(e) T7 compression-tension no. 4

(f) T7 compression-tension no. 5

Figure A.6: Plot of the raw data and the material parameter estimate by the backstress calculation Method B for T7 tensile tests, plot 2

A.3 Material Parameter Validation

(a) T4 tension no. 1

(b) T4 tension-compression no. 1

(c) T4 tension-compression no. 4

(d) T4 compression-tension no. 1

(e) T6 tension-compression no. 1

(f) T6 tension-compression no. 4

Figure A.7: Validation of combined isotropic-kinematic material hardening parameters, plot 1
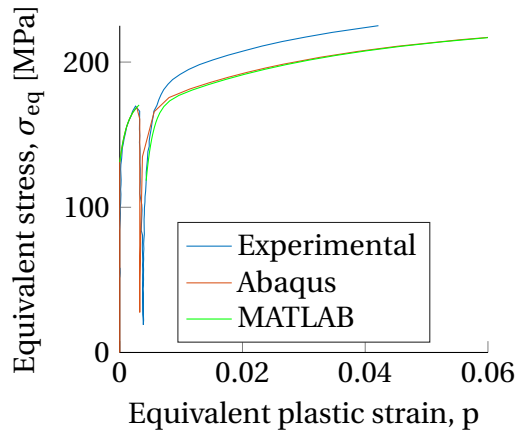
(a) T6 compression-tension no. 1
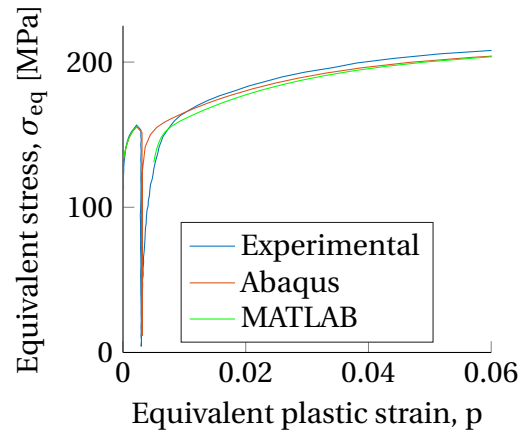
(b) T7 tension-compression no. 1
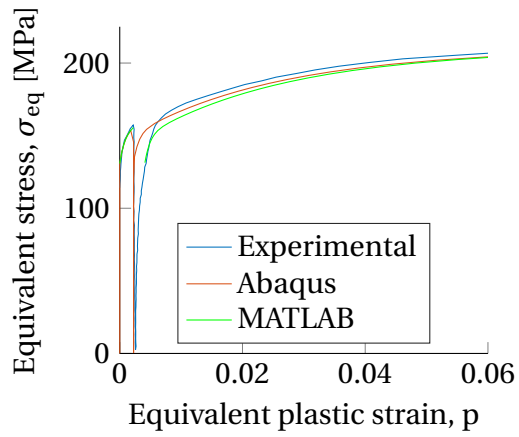
(c) T7 compression-tension no. 1

(d) T7 compression-tension no. 4

Figure A.8: Validation of combined isotropic-kinematic material hardening parameters, plot 2
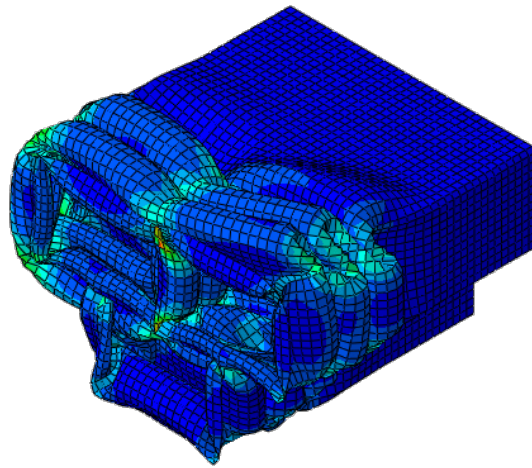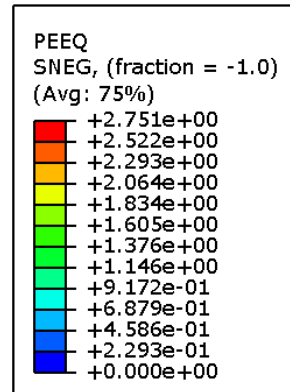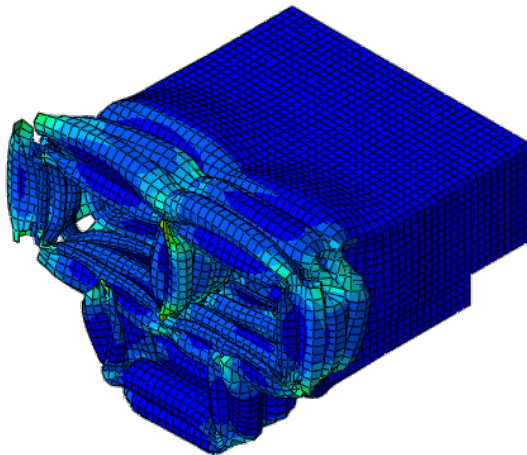
A.4 Case

A.4.1 Axial Crushing

(a) T4

(b) Color scheme for T4

(c) T6

(d) Color scheme for T6

(e) T7

(f) Color scheme for T7
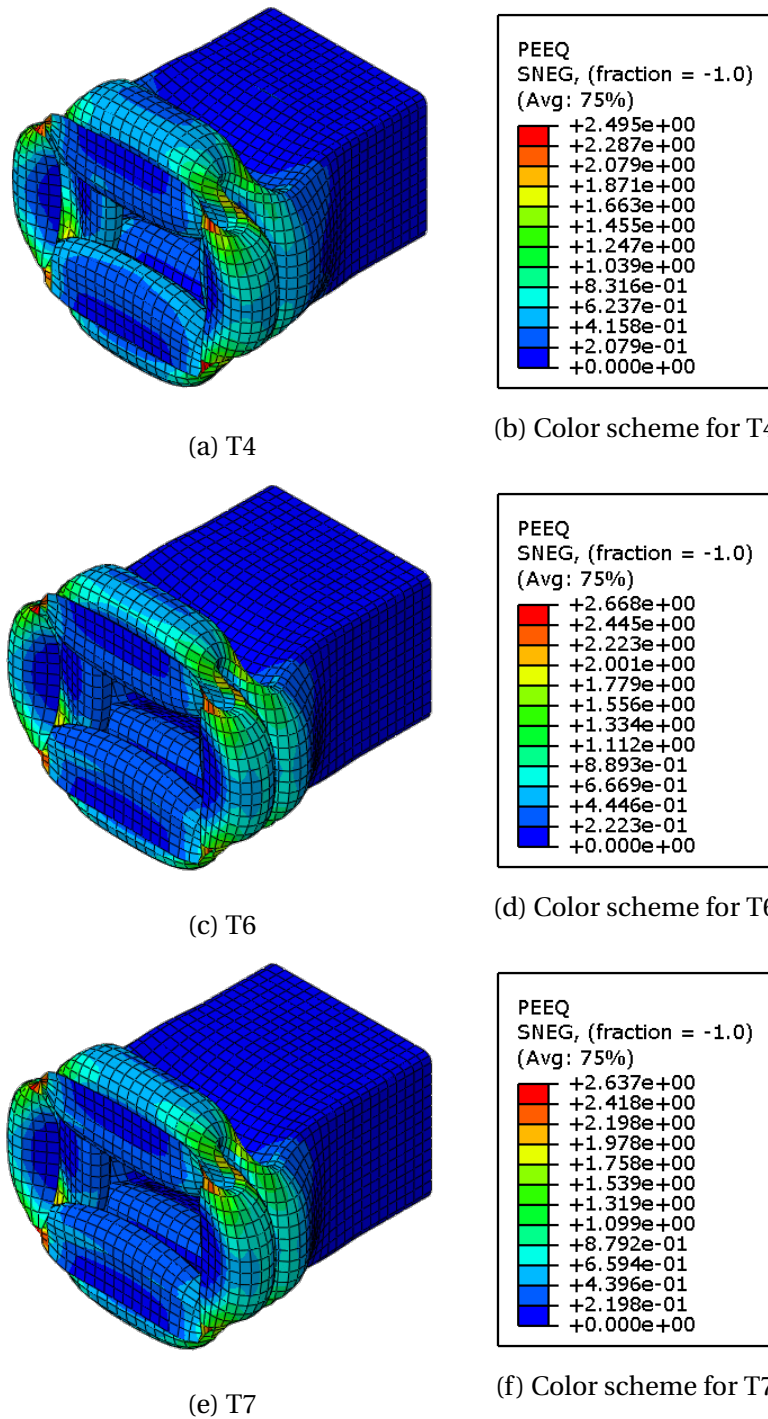
Figure A.9: The Equivalent plastic strain field for the final deformed state for the single chamber profile with isotropic hardening

(a) T4

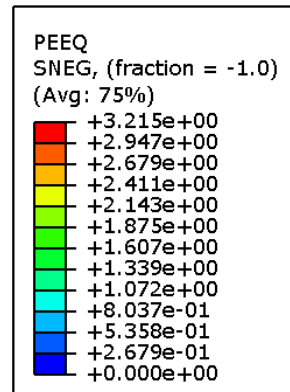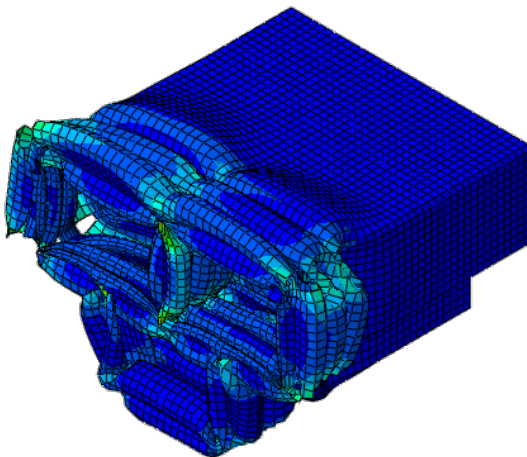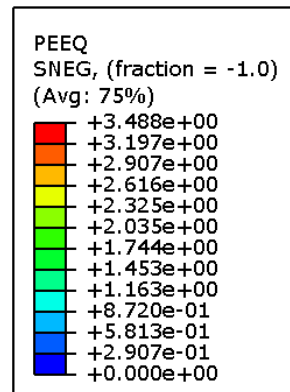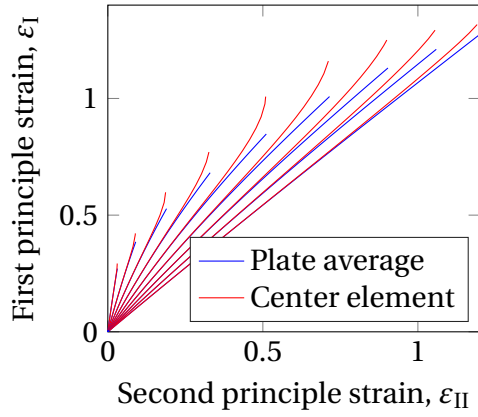(b) Color scheme for T4

(c) T6

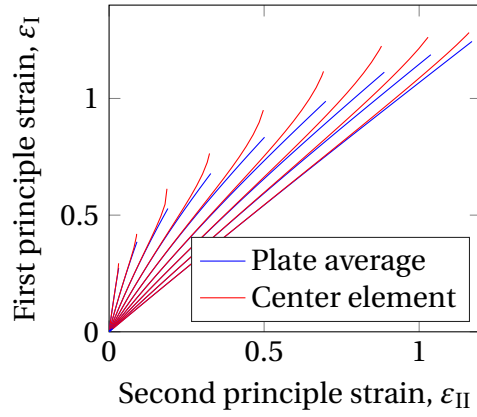(d) Color scheme for T6

(e) T7

(f) Color scheme for T7

Figure A.10: The Equivalent plastic strain field for the final deformed state for the triple chamber profile with isotropic hardening
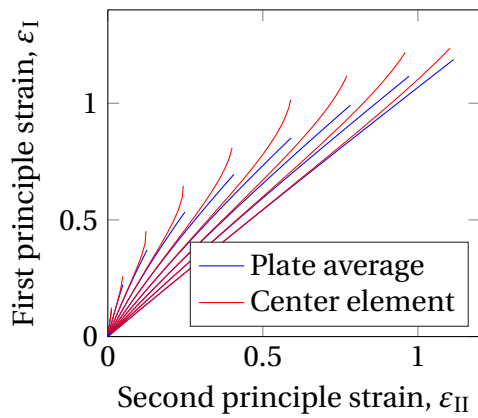
A.4.2 Forming Limit Diagram

(a) T4 with isotropic hardening

(b) T4 with combined hardening

(c) T6 with isotropic hardening

(d) T6 with combined hardening

(e) T7 with isotropic hardening

(f) T7 with combined hardening

Figure A.11: Plot showing the relationship between the principal strains in the ordinary study for isotropic hardening (left) combined hardening (right)
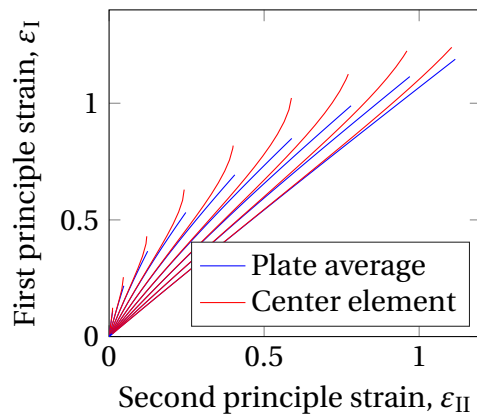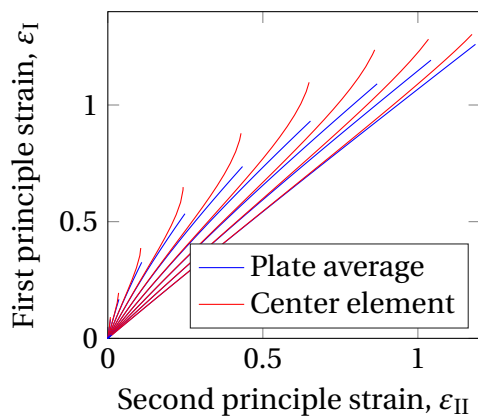
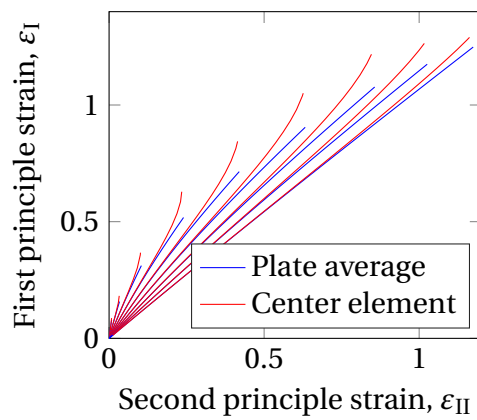(a) T4 with isotropic hardening
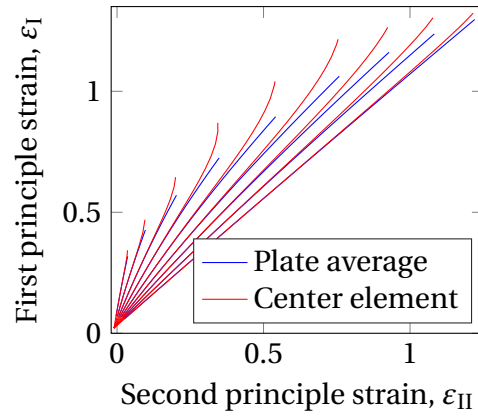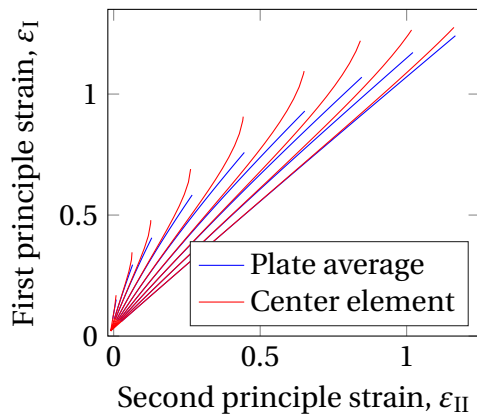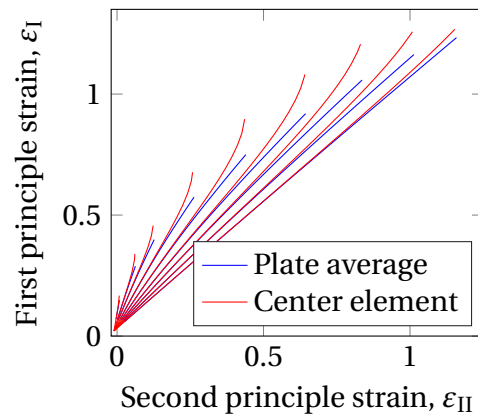
(b) T4 with combined hardening

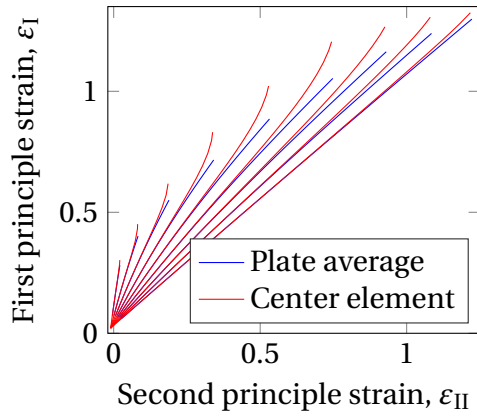(c) T6 with isotropic hardening

(d) T6 with combined hardening
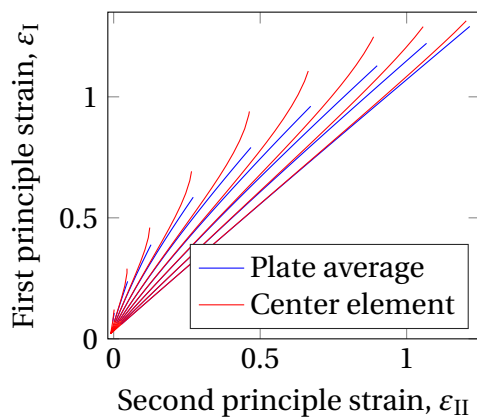
(e) T7 with isotropic hardening
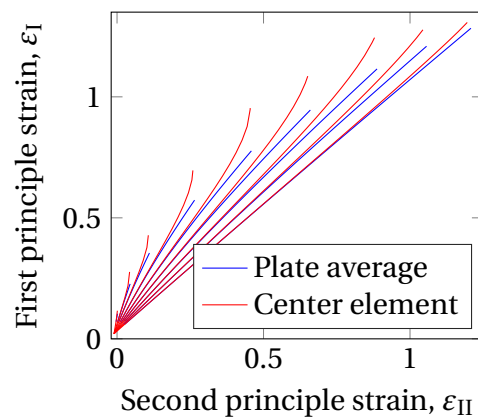
(f) T7 with combined hardening

Figure A.12: Plot showing the relationship between the principal strains in the pre-strained study for isotropic hardening (left) combined hardening (right)

A.4.3 Impact Loading on plates
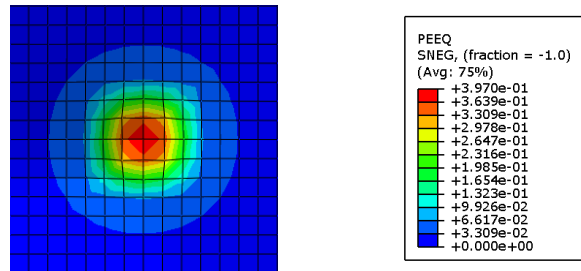
(a) Detailed cut of top view for T4
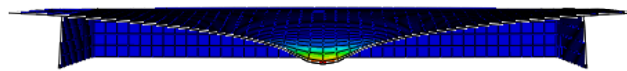
(b) Color scheme for T4

(c) Side view for T4 with cut through center line
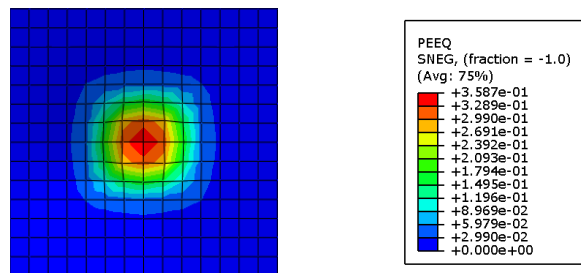
(d) Detailed cut of top view for T6

(e) Color scheme for T6
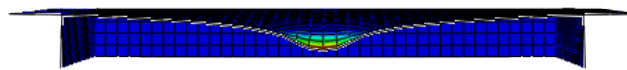
(f) Side view for T6 with cut through center line
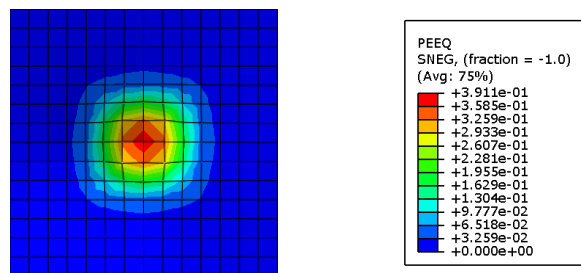
(g) Detailed cut of top view for T7

(h) Color scheme for T7
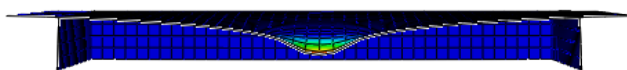
(i) Side view for T7 with cut through center line

Figure A.13: The equivalent plastic strain field in the final deformed shape of the E1 test series with the isotropic hardening model
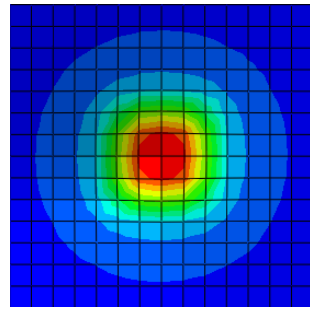
(a) Detailed cut of top view for T4
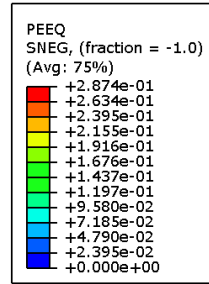
(b) Color scheme for T4
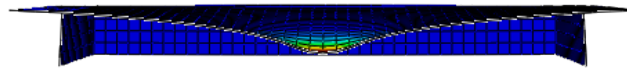
(c) Side view for T4 with cut through center line
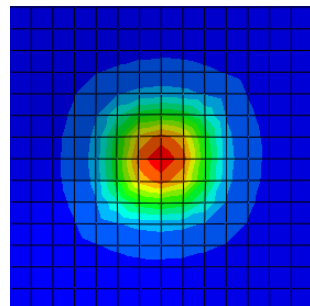
(d) Detailed cut of top view for T6
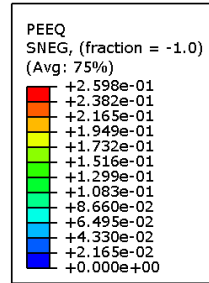
(e) Color scheme for T6
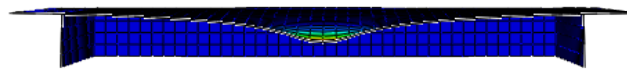
(f) Side view for T6 with cut through center line
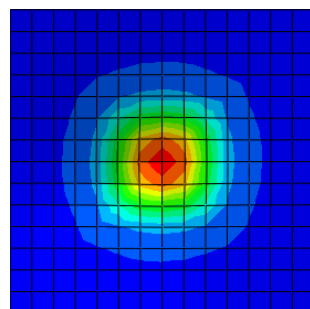
(g) Detailed cut of top view for T7
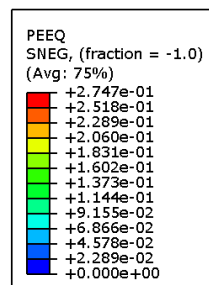
(h) Color scheme for T7
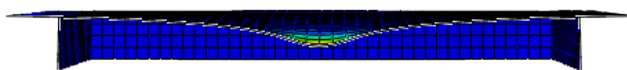
(i) Side view for T7 with cut through center line

Figure A.14: The equivalent plastic strain field in the final deformed shape of the E2 test series with the isotropic hardening model
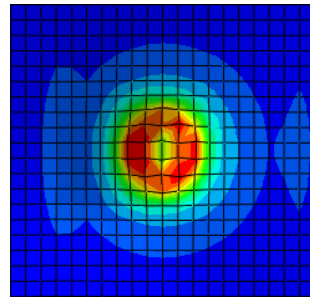
(a) Detailed cut of top view for T4
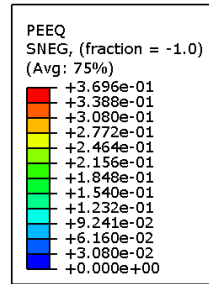
(b) Color scheme for T4
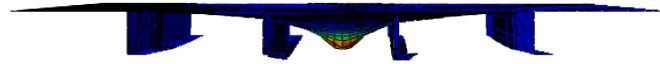
(c) Side view for T4 with cut through center line
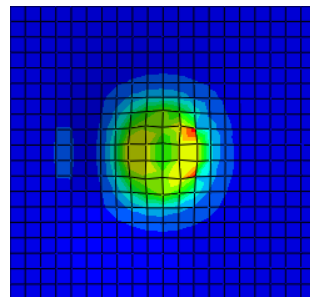
(d) Detailed cut of top view for T6
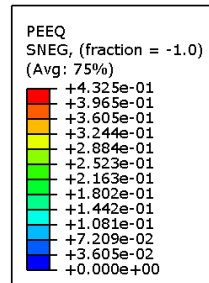
(e) Color scheme for T6
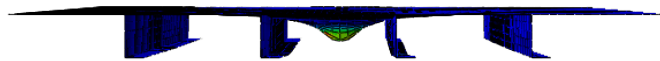
(f) Side view for T6 with cut through center line
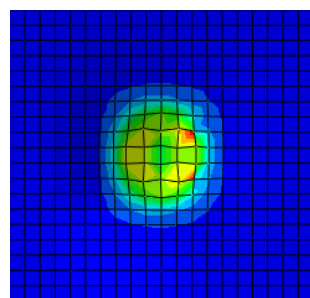
(g) Detailed cut of top view for T7
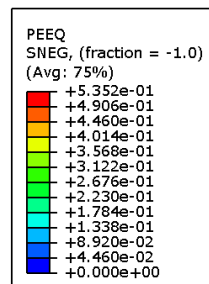
(h) Color scheme for T7
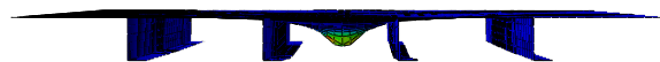
(i) Side view for T7 with cut through center line

Figure A.15: The equivalent plastic strain field in the final deformed shape of the DM test series with the isotropic hardening model

A.4.4   Blast Loading

The same color scheme is used for the same temper, to make it easier to compare the two material hardening models in the following figures.

(a) A1x T4 with isotropic hardening

(b) A1x T4 with combined hardening

(c) Color scheme for T4

(d) A1x T6 with isotropic hardening

(e) A1x T6 with combined hardening

(f) Color scheme, T6
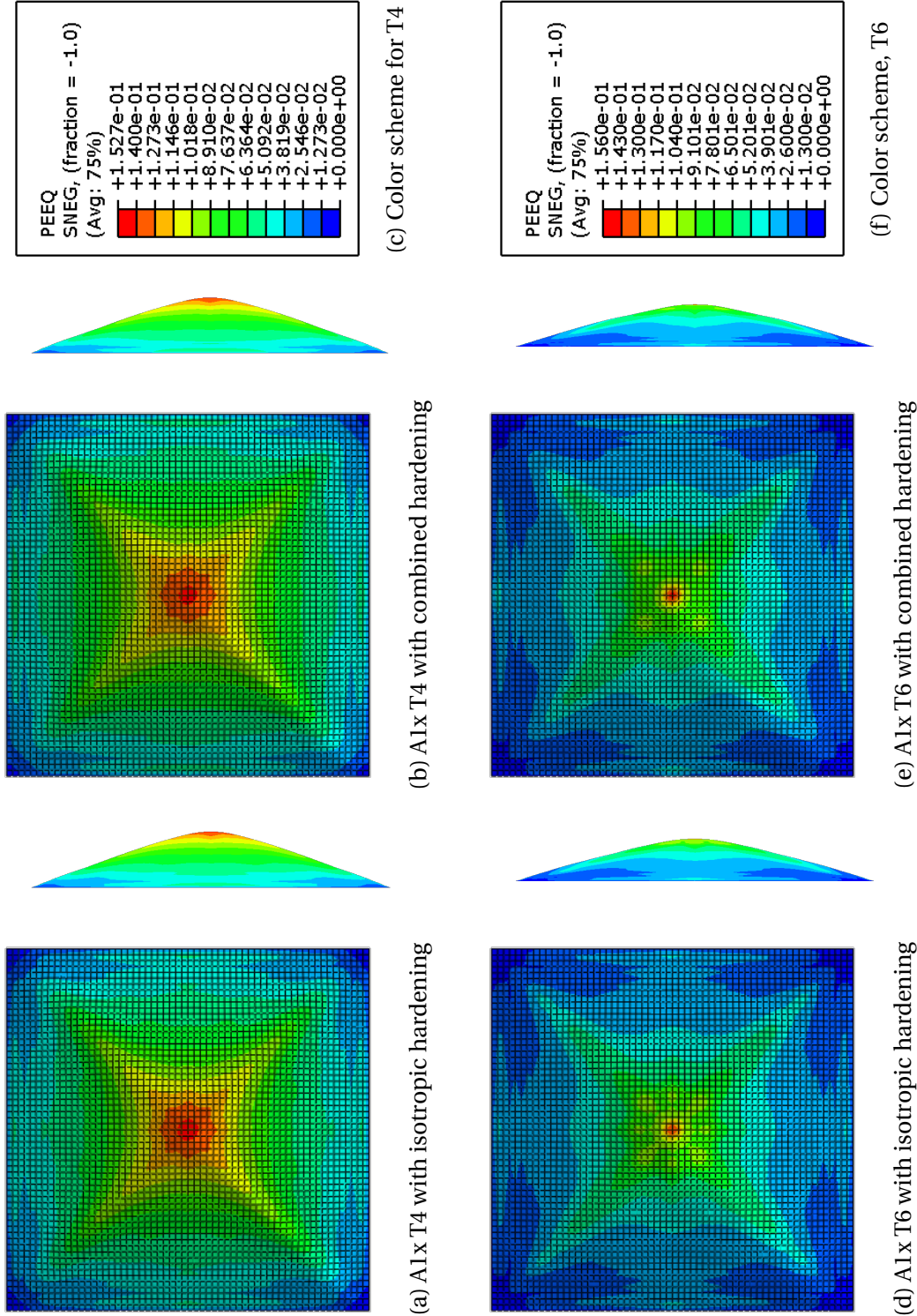
Figure A.16: Front and side view of the equivalent plastic strain field in the final deformed state for test series A1x T4 (upper) and T6 (lower)

(a) A1x T7 with isotropic hardening

(b) A1x T7 with combined hardening

(c) Color scheme
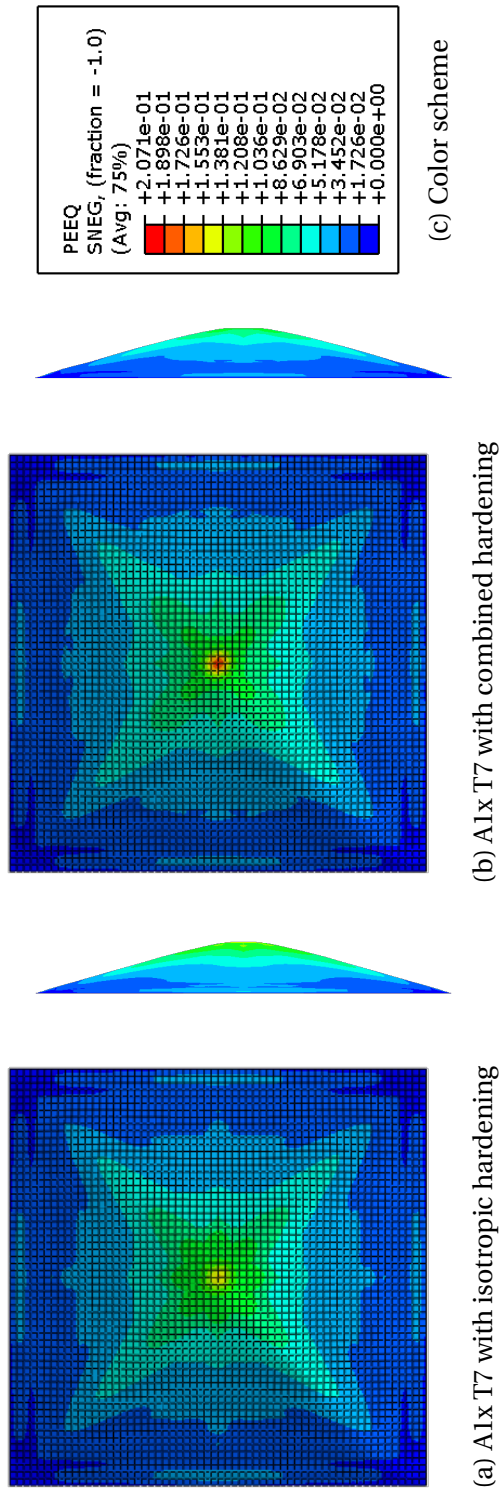
Figure A.17: Front and side view of the equivalent plastic strain field in the final deformed state for test series A1x T7

(a) A2x T4 with isotropic hardening

(b) A2x T4 with combined hardening

(c) Color scheme, T4

(d) A2x T6 with isotropic hardening

(e) A2x T6 with combined hardening

(f) Color scheme, T6
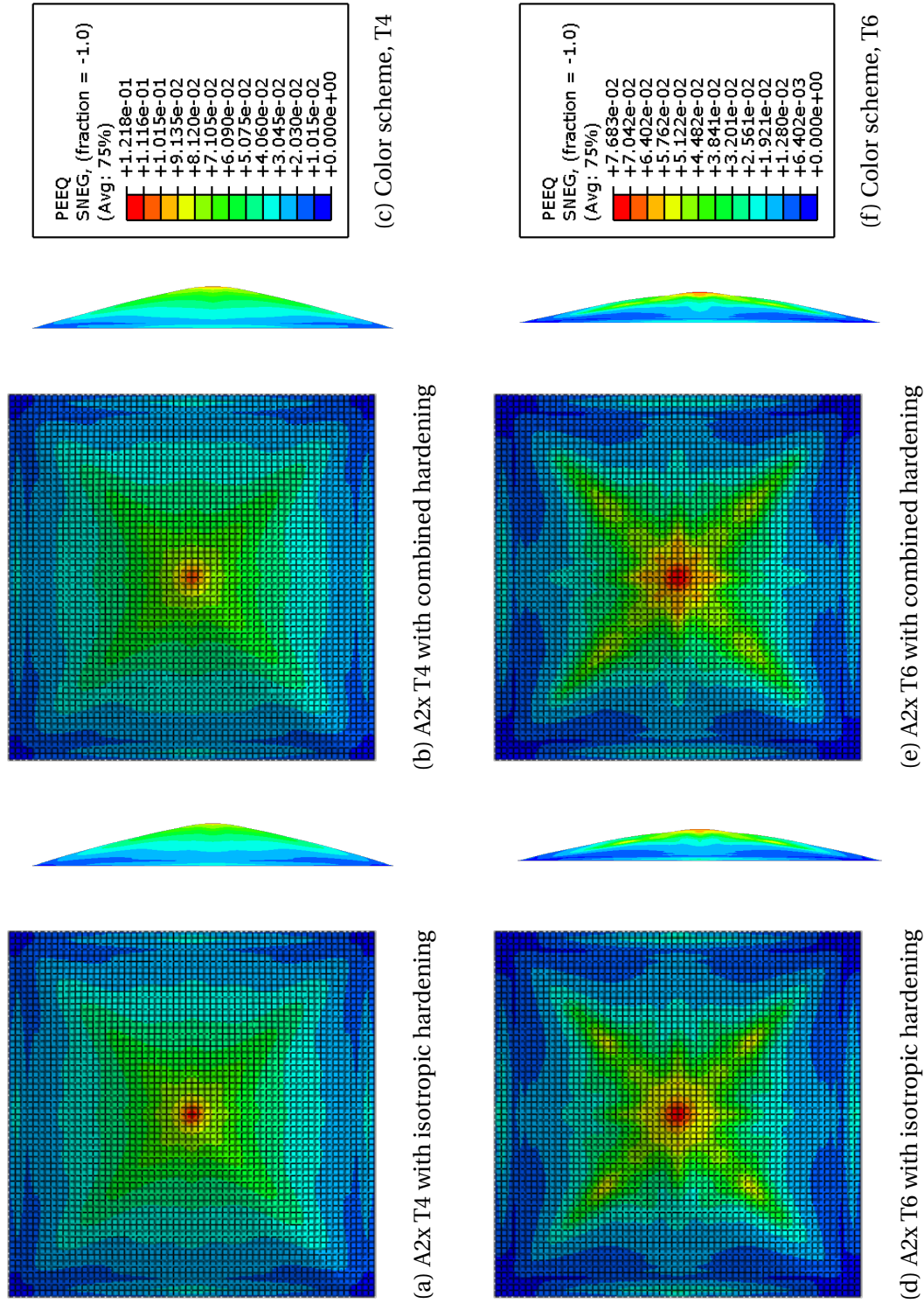
Figure A.18: Front and side view of the equivalent plastic strain field in the final deformed state for test series A2x T4 (upper) and T6 (lower)

(a) A2x T7 with isotropic hardening

(b) A2x T7 with combined hardening

(c) Color scheme
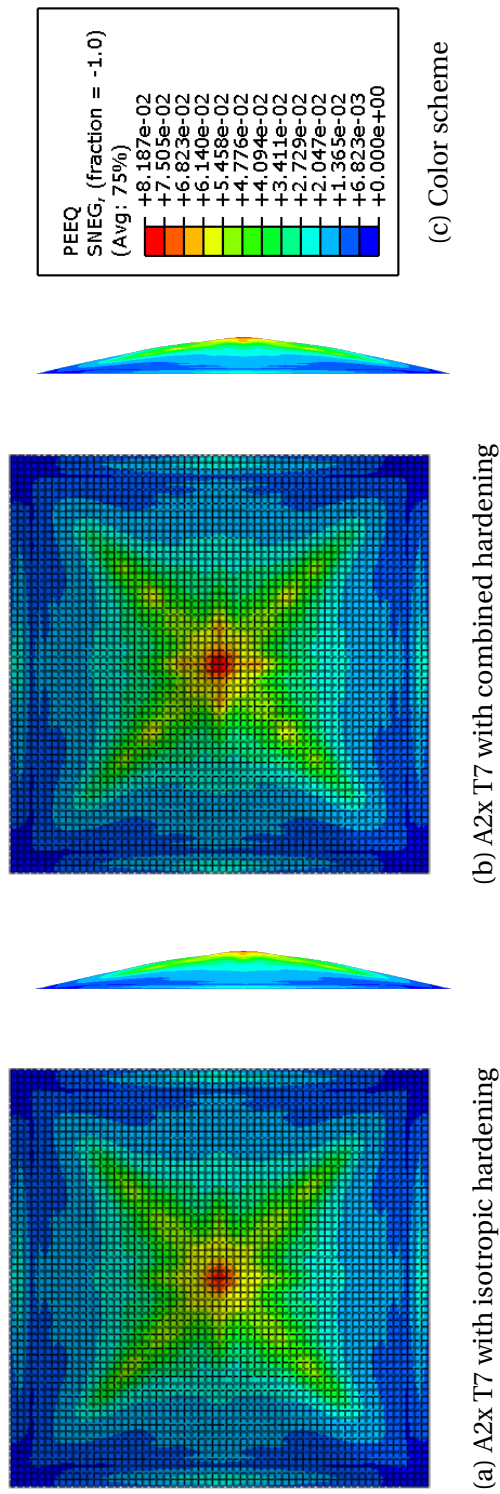
Figure A.19: Front and side view of the equivalent plastic strain field in the final deformed state for test series A2x T7

(a) A3x T4 with isotropic hardening

(b) A3x T4 with combined hardening

(c) Color scheme, T4

(d) A3x T6 with isotropic hardening

(e) A3x T6 with combined hardening

(f) Color scheme, T6
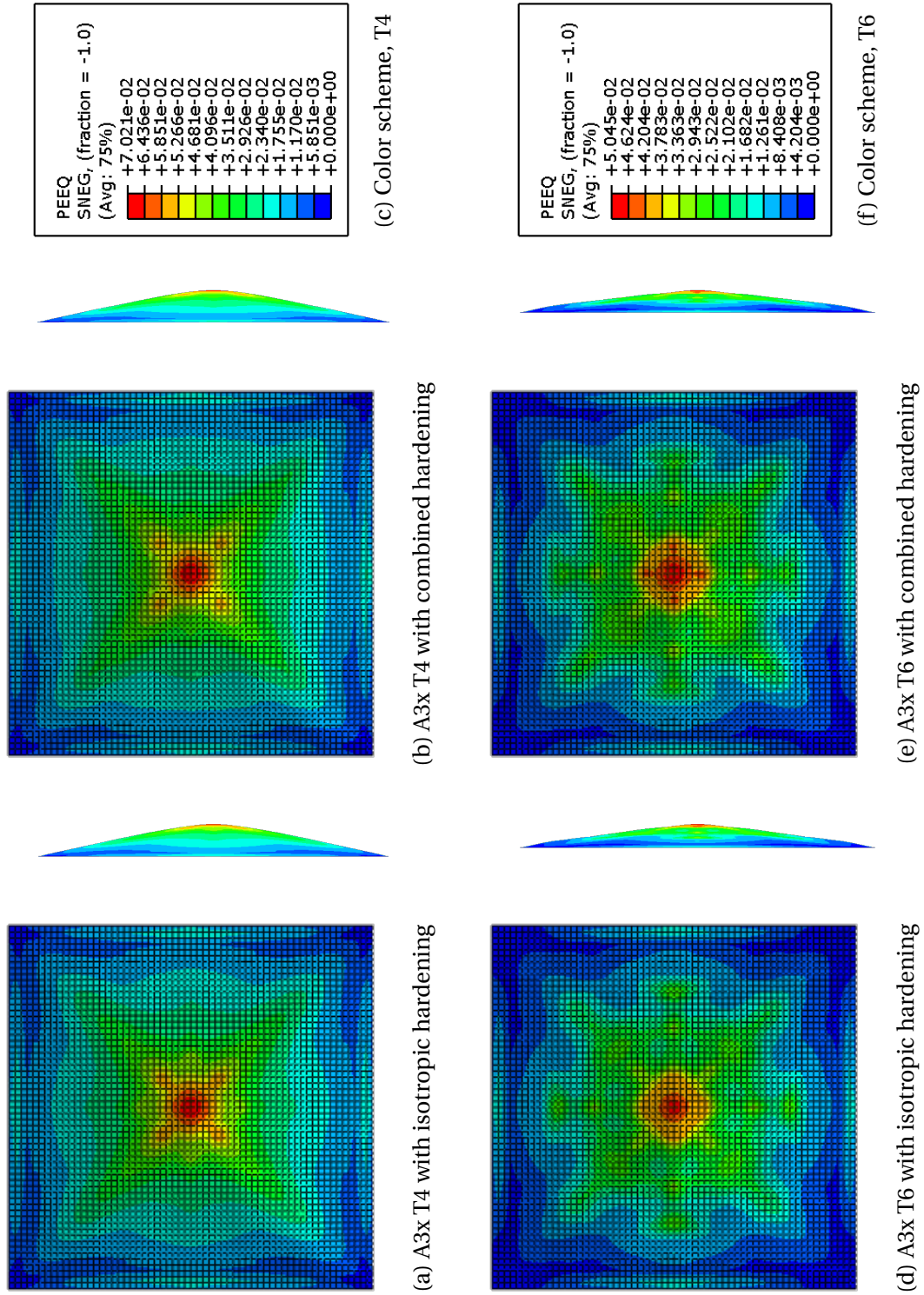
Figure A.20: Front and side view of the equivalent plastic strain field in the final deformed state for test series A3x T4 (upper) and T6 (lower)

(a) A3x T7 with isotropic hardening

(b) A3x T7 with combined hardening

(c) Color scheme

PEEQ
SNEG, (fraction = -1.0)
(Avg: 75%)
+5.269e-02
+4.830e-02
+4.391e-02
+3.952e-02
+3.513e-02
+3.074e-02
+2.635e-02
+2.196e-02
+1.756e-02
+1.317e-02
+8.782e-03
+4.391e-03
+0.000e+00
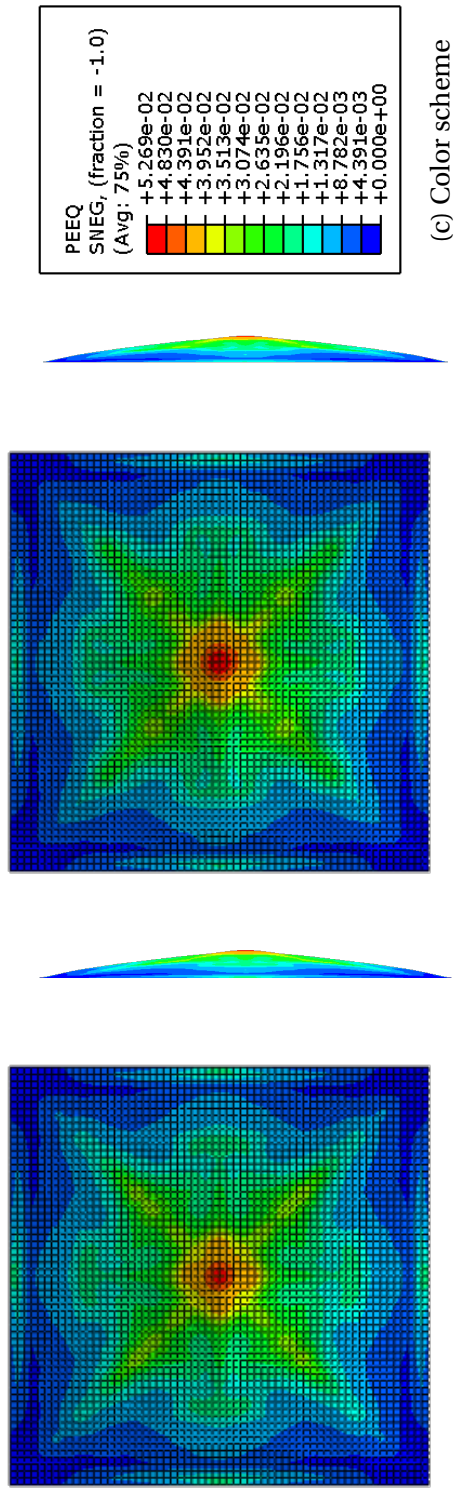
Figure A.21: Front and side view of the equivalent plastic strain field in the final deformed state for test series A3x T7

B | Matlab Code

```matlab
clear; clc;
%Material constants
E = 70000; v = 0.33; e_off = 0.0005;


%% ————————————————File Location
    ————————————————%
%Locate lab data files
materialDataDir = 'C:\Users\kris_\Documents\NTNU\OneDrive — NTNU\Skole\
    Masteroppgave\Materialdata LAB\';
labFiles = dir(strcat(materialDataDir,'AA6060*.txt'));
%Add tests to global file list. T4, T5, T6
fileNameList = { {}, {}, {} };
for i=1:length(labFiles)
    fileName = labFiles(i).name;
    if(strfind(fileName,'T4'))
        fileNameList{1}{end + 1} = fileName;
    elseif (strfind(fileName,'T6'))
        fileNameList{2}{end + 1} = fileName;
    elseif (strfind(fileName,'T7'))
        fileNameList{3}{end + 1} = fileName;
    end
end
%% ————————————————Material Processing
    ————————————————%
%Group the tests in such a fashion: Temper and Test
tStress = { {}, {}, {} };
lStrain = { {}, {}, {} };
plStrain = { {}, {}, {} };
```

```matlab
eqStress = { {}, {}, {} };
eqPlStrain = { {}, {}, {} };
Imax = { {}, {}, {} };
Imin = { {}, {}, {} };
for i =1:3
    for j = 1:12
        %Each file have the format:
        %Time(s) Force(kN) Position(mm) Diameter X(mm) Diameter Y(mm)
        file = strcat(materialDataDir,fileNameList{i}{j});
        fileID = fopen(file,'r');
        formatSpec = '%s %s %s %s %s';
        data = textscan(fileID, formatSpec,'Headerlines',13);
        fclose(fileID);
        %Replace ',' with '.' for matlab parsing
        for k=1:length(data)
            data{k} = strrep(data{k},',','.');
        end
        %Initial material parameters
        time = str2double(data{1});
        F = str2double(data{2});
        Dx = str2double(data{4});
        Dy = str2double(data{5});
        %Remove unwanted area values from the adjusting of the laser
        A = pi/4*Dx.*Dy;
        A0 = Dx(1)*Dy(1)/4*pi;
        [Fmax, imax] = max(smooth(F,20));
        [Fmin, imin] = min(smooth(F,20));
        [Fmax2, imax2] = max(F);
        [Fmin2, imin2] = min(F);
        imax = imax + (imax2 - imax)*(imax2 > imax);
        imin = imin + (imin2 - imin)*(imin2 > imin);
        if (j == 1 || j == 2)
            for l=1:length(A) - 1
                A(l+1) = min(A(l),A(l + 1));
            end
        elseif (j > 2 && j < 8)
            for l=1:imax
```

```matlab
            A(l+1) = min(A(l),A(l + 1));
        end
        for l=length(A):-1:imax
            A(l-1) = min(A(l),A(l - 1));
        end
    else
        for l=imin:-1:2
            A(l-1) = min(A(l),A(l - 1));
        end
        for l=imin + 1:length(A)-1
            A(l+1) = min(A(l),A(l + 1));
        end
    end
    %Experimental Measures
    tStress{i}{end + 1} = 1000*F./A;
    lStrain{i}{end + 1} = log(A0./A) + (1 - 2*v)*(1000.*F)./(A*E);
    plStrain{i}{end + 1} = lStrain{i}{end} - tStress{i}{end}/E;
    if (j == 1 || j == 2)
        eqPlStrain{i}{end + 1} = plStrain{i}{end};
        aOverR = 1.1*(plStrain{i}{end}(imax+1:end) - plStrain{i}{end}(
            imax));
        eqStress{i}{end + 1} = [tStress{i}{end}(1:imax); tStress{i}{
            end}(imax+1:end)./((1+2./aOverR).*log(1+aOverR/2))];
    elseif (j > 2 && j < 8)
        eqPlStrain{i}{end + 1} = [plStrain{i}{end}(1:imax); ...
            2 * plStrain{i}{end}(imax) - plStrain{i}{end}(imax + 1:end
                )];
        eqStress{i}{end + 1} = tStress{i}{end};
    else
        eqPlStrain{i}{end + 1} = [- plStrain{i}{end}(1:imin); ...
            - 2 * plStrain{i}{end}(imin) + plStrain{i}{end}(imin + 1:
                end)];
        aOverR = 1.1*(plStrain{i}{end}(imin+1:end) - plStrain{i}{end}(
            imin));
        eqStress{i}{end + 1} = [tStress{i}{end}(1:imin); tStress{i}{
            end}(imin+1:end)./((1+2./aOverR).*log(1+aOverR/2))];
    end
```

```matlab
        Imax{i}{end + 1} = imax;
        Imin{i}{end + 1} = imin;
    end
end


%% ───────────────────Calculation of Material Prameters
    ────────────────%
%Removing entries after frature
modEqStress = eqStress;
modEqPlStrain = eqPlStrain;
modPlStrain = plStrain;
nFracture = 5;
for i=1:3
    for j=1:12
        [m, iFracture] = max(abs(modEqStress{i}{j}));
        modEqStress{i}{j} = modEqStress{i}{j}(1:iFracture + nFracture);
        modEqPlStrain{i}{j} = modEqPlStrain{i}{j}(1:iFracture + nFracture)
            ;
        modPlStrain{i}{j} = modPlStrain{i}{j}(1:iFracture + nFracture);
        if (i == 2 && j == 4)
            modEqStress{i}{j} = modEqStress{i}{j}(1:iFracture);
            modEqPlStrain{i}{j} = modEqPlStrain{i}{j}(1:iFracture);
            modPlStrain{i}{j} = modPlStrain{i}{j}(1:iFracture);
        end
    end
end
%% Calculating backstress with method in Manes et al. 2011 METHOD A
chiKH = { {}, {}, {} };
chiIH = { {}, {}, {} };
plStrainH = { {}, {}, {} };
punkterXAbs = { {}, {}, {} };
punkterYAbs = { {}, {}, {} };
punkterXt = { {}, {}, {} };
punkterYt = { {}, {}, {} };
Emods = { {}, {}, {} };
listIU = { {}, {}, {} };
listIR = { {}, {}, {} };
```

```matlab
for i = 1:3
    for j = 1:12
        if (j > 2 && j < 8)
            %Find index stress value closes to zero
            [res, Izero] = min(abs(modEqStress{i}{j}(Imax{i}{j}:end)));
            Izero = Izero + Imax{i}{j} − 1;
            %Locate the sigmaU by locating max strain
            [~, IStrainMax] = max(lStrain{i}{j});
            iU = IStrainMax;
            for k=IStrainMax:−1:IStrainMax−20
                dS = (modEqStress{i}{j}(k)−modEqStress{i}{j}(k−1));
                if (dS > −0.3 && dS < 0.3)
                    iU = k;
                    break;
                end
            end
            sigmaU = modEqStress{i}{j}(iU);
            punkterXAbs{i}{end + 1} = plStrain{i}{j}(iU);
            punkterYAbs{i}{end + 1} = abs(sigmaU);
            punkterXt{i}{end + 1} = lStrain{i}{j}(iU);
            punkterYt{i}{end + 1} = sigmaU;
            %Linear approximate Eavg
            p = polyfit(lStrain{i}{j}(iU:Izero),modEqStress{i}{j}(iU:Izero
                ),1);
            Eavg = abs(p(1));
            Emods{i}{end + 1} = p;
            for k=Imax{i}{j}:length(lStrain{i}{j}(Imax{i}{j}:end))
                if (lStrain{i}{j}(k) < lStrain{i}{j}(Imax{i}{j}) − (sigmaU
                    − modEqStress{i}{j}(k))/Eavg − e_off)
                    iR = k;
                    break;
                end
            end
            plStrainH{i}{end + 1} = abs(modPlStrain{i}{j}(iU) − (
                modPlStrain{i}{j}(iU) − modPlStrain{i}{j}(iR(1)))/2);
            listIU{i}{end + 1} = iU;
        elseif (j >= 8)
```

```matlab
    %Finding index of zero stress
    [res, Izero] = min(abs(modEqStress{i}{j}(Imin{i}{j}:end)));
    Izero = Izero + Imin{i}{j}- 1;
    %Locate the sigmaU by locating min strain
    [~, IStrainMin] = min(lStrain{i}{j});
    iU = IStrainMin;
    for k=IStrainMin:-1:IStrainMin-20
        dS = (modEqStress{i}{j}(k)- modEqStress{i}{j}(k-1));
        if (dS > -0.3 && dS < 0.3)
            iU = k;
            break;
        end
    end
    sigmaU = modEqStress{i}{j}(iU);
    punkterXAbs{i}{end + 1} = plStrain{i}{j}(iU);
    punkterYAbs{i}{end + 1} = abs(sigmaU);
    punkterXt{i}{end + 1} = lStrain{i}{j}(iU);
    punkterYt{i}{end + 1} = sigmaU;
    %Linear approximate Eavg
    p = polyfit(lStrain{i}{j}(iU:Izero),modEqStress{i}{j}(iU:Izero
        ),1);
    Eavg = abs(p(1));
    Emods{i}{end + 1} = p;
    for k=Imin{i}{j}:length(lStrain{i}{j}(Imin{i}{j}:end))
        if (lStrain{i}{j}(k) > lStrain{i}{j}(Imin{i}{j}) - (sigmaU
            - modEqStress{i}{j}(k))/Eavg + e_off)
            iR = k;
            break;
        end
    end
    plStrainH{i}{end + 1} = abs(modPlStrain{i}{j}(iU) + (
        modPlStrain{i}{j}(iU) - modPlStrain{i}{j}(iR(1)))/2);
    listIU{i}{end + 1} = iU;
else
    continue;
end
sigmaR = modEqStress{i}{j}(iR(1));
```

```matlab
            listIR{i}{end + 1} = iR;
            punkterXAbs{i}{end + 1} = eqPlStrain{i}{j}(iR);
            punkterYAbs{i}{end + 1} = abs(sigmaR);
            punkterXt{i}{end + 1} = lStrain{i}{j}(iR);
            punkterYt{i}{end + 1} = sigmaR;
            chiKH{i}{end + 1} = abs((sigmaU + sigmaR)/2);
            chiIH{i}{end + 1} = abs((sigmaU - sigmaR)/2);
        end
    end


%% --------------------Yield Stress Calculation
    ------------------------------%
%METHOD 1 - Sigma_0.025%
yieldStresses1 = { {}, {}, {} };
plasticStrainStop = 0.00025;
stressStart = [35,95,100];
for i=1:3
    for j=1:12
        iYeild = find(abs(smooth(eqStress{i}{j},30)) > stressStart(i) &
            smooth(eqPlStrain{i}{j},30) > plasticStrainStop);
        yieldStresses1{i}{end + 1} = eqStress{i}{j}(iYeild(1));
    end
end
%METOD 2 - Two Voce, before load reversal
nStart = [[277, 305, 212, 206, 180, 198, 203, 126, 120, 102, 179, 126 ];
    ...
          [433, 345, 723, 344, 327, 306, 403, 250, 314, 282, 211, 215 ];
            ...
          [465, 465, 406, 283, 289, 820, 352, 283, 197, 279, 230, 146 ] ];
yieldStresses2 = { {}, {}, {} };
Voce_xList = { {}, {}, {} };
options=optimset('disp','iter','LargeScale','off','TolFun',1e-10,'MaxIter'
    ,100000,'MaxFunEvals',100000);
Q1_0 = 100; C1_0 = 5; Q2_0 = 500; C2_0 = 10; flyt = 60;
Voce_x0 = [Q1_0,C1_0,Q2_0,C2_0,flyt];
Voce_LB = [0, 0, 0, 0, 40];
```

```matlab
Voce_UB = [Q1_0*100, C1_0*100, Q2_0*10, C2_0*50,180];
listEnd = {cell(1,12),cell(1,12),cell(1,12)};
listEnd{1,1}(3:12) = listIU{1};
listEnd{1,2}(3:12) = listIU{2};
listEnd{1,3}(3:12) = listIU{3};
listEnd{1}{1} = length(modEqStress{1}{1});
listEnd{1}{2} = length(modEqStress{1}{2});
listEnd{2}{1} = length(modEqStress{2}{1});
listEnd{2}{2} = length(modEqStress{2}{2});
listEnd{3}{1} = length(modEqStress{3}{1});
listEnd{3}{2} = length(modEqStress{3}{2});
for i=1:3
    if( i == 1)
        Voce_LB(5) = 40;
        Voce_UB(5) = 120;
    else
        Voce_LB(5) = 70;
        Voce_UB(5) = 200;
    end
    for j=1:12
        x = find(modEqPlStrain{i}{j}(nStart(i,j):listEnd{i}{j}) < 0.06);
        [Voce_x,res] = lsqcurvefit(@VoceTwoPoints,Voce_x0,modEqPlStrain{i
            }{j}(nStart(i,j):nStart(i,j) + x(end)),abs(smooth(modEqStress{i
            }{j}(nStart(i,j):nStart(i,j) + x(end)),20)),Voce_LB,Voce_UB,
            options);
        Voce_xList{i}{end + 1} = Voce_x;
        yieldStresses2{i}{end + 1} = Voce_x(5);
        if (j > 7)
            yieldStresses2{i}{end} = -yieldStresses2{i}{end};
        end
    end
end
%% METHOD 3 Yield Stresses - Two Voce Two Chi, after load reversal
options=optimset('disp','iter','TolFun',1e-10,'TolX',1e-8,'MaxIter',10000,
    'MaxFunEvals',250000);
yieldStresses3 = { {}, {}, {}};
chi_xList = { {}, {}, {} };
```

```
kappa11_0 = 3500; kappa21_0 = 100; kappa12_0 = 400; kappa22_0 = 10;
Q1_0 = 500; C1_0 = 10; Q2_0 = 50; C2_0 = 1;
chi_x0 = [kappa11_0,kappa21_0,kappa12_0,kappa22_0,Q1_0,C1_0,Q2_0,C2_0,flyt
    ];
chi_LB = [0, 0, 0, 0, 0, 0, 0, 0, 40];
chi_UB = [kappa11_0*1000,kappa21_0*100,kappa12_0*1000,kappa22_0*100,Q1_0
    *100, C1_0*100, Q2_0*100, C2_0*100,150];
for i=1:3
    if( i == 1)
        chi_LB(9) = 45;
        chi_UB(9) = 90;
    else
        chi_LB(9) = 80;
        chi_UB(9) = 160;
    end
    for j=1:12
        if (j < 3)
            [chi_x,res] = lsqcurvefit(@TwoVoceTwoChiF1,chi_x0,
                modEqPlStrain{i}{j}(nStart(i,j):end),smooth(modEqStress{i}{
                j}(nStart(i,j):end),20),chi_LB,chi_UB, options);
        else
            [chi_x,res] = lsqcurvefit(@TwoVoceTwoChiF4,chi_x0,
                modEqPlStrain{i}{j}(listIU{i}{j-2}:end),abs(smooth(
                modEqStress{i}{j}(listIU{i}{j-2}:end),20)),chi_LB,chi_UB,
                options);
        end
        chi_xList{i}{end + 1} = chi_x;
        yieldStresses3{i}{end + 1} = chi_x(9);
        if (j > 7)
            yieldStresses3{i}{end} = -yieldStresses3{i}{end};
        end
    end
end
%Choosing Yield Stress Method 2 as yield stresses
yield(1) = abs(yieldStresses2{1}{1});
yield(2) = abs(yieldStresses2{2}{1});
yield(3) = abs(yieldStresses2{3}{1});
```

```matlab
%% Nonlinear regression of the backstress calculation METHOD A
nonLinRegKUR = { {}, {}, {} };
nonLinRegIUR = { {}, {}, {} };
for i=1:3
    %Initial parameters
    kappa11 = 1e4;
    kappa21 = 1e2;
    chi_x0 = [kappa11, kappa21];
    Q_IH = 1e4;
    C_IH = 40;
    iso_x0 = [Q_IH C_IH yield(i)];
    for j=1:3
        if (j == 1)
            chi_x = lsqcurvefit(@nonLinRegBackstress,chi_x0,cell2mat(
                plStrainH{i}(1:5)),cell2mat(chiKH{i}(1:5)));
            iso_x = lsqcurvefit(@nonLinRegIsotropic,iso_x0,cell2mat(
                plStrainH{i}(1:5)),cell2mat(chiIH{i}(1:5)), [0 0 0], []);
        elseif (j == 2)
            if (i == 2)
                chi_x = lsqcurvefit(@nonLinRegBackstress,chi_x0,cell2mat(
                    plStrainH{i}(6:9)),cell2mat(chiKH{i}(6:9)));
                iso_x = lsqcurvefit(@nonLinRegIsotropic,iso_x0,cell2mat(
                    plStrainH{i}(6:9)),cell2mat(chiIH{i}(6:9)), [0 0 0],
                    []);
            else
                chi_x = lsqcurvefit(@nonLinRegBackstress,chi_x0,cell2mat(
                    plStrainH{i}(6:10)),cell2mat(chiKH{i}(6:10)));
                iso_x = lsqcurvefit(@nonLinRegIsotropic,iso_x0,cell2mat(
                    plStrainH{i}(6:10)),cell2mat(chiIH{i}(6:10)), [0 0 0],
                    []);
            end
        else
            if (i == 2)
                chi_x = lsqcurvefit(@nonLinRegBackstress,chi_x0,cell2mat(
                    plStrainH{i}(1:9)),cell2mat(chiKH{i}(1:9)));
                iso_x = lsqcurvefit(@nonLinRegIsotropic,iso_x0,cell2mat(
                    plStrainH{i}(1:9)),cell2mat(chiIH{i}(1:9)), [0 0 0],
```

```matlab
                []);
            else
                chi_x = lsqcurvefit(@nonLinRegBackstress,chi_x0,cell2mat(
                    plStrainH{i}(1:10)),cell2mat(chiKH{i}(1:10)));
                iso_x = lsqcurvefit(@nonLinRegIsotropic,iso_x0,cell2mat(
                    plStrainH{i}(1:10)),cell2mat(chiIH{i}(1:10)), [0 0 0],
                    []);
            end
        end
        nonLinRegKUR{i}{end + 1} = chi_x;
        nonLinRegIUR{i}{end + 1} = iso_x;
    end
end
%% METHOD B BACKSTRESS CALCULATION - FEWER MATERIAL PARAMETERS METHOD FROM
    TARIGOPULA ET AL. (2008)
options=optimset('disp','iter','TolFun',1e-20,'TolX',1e-10,'MaxIter'
    ,100000,'MaxFunEvals',100000);
%Step 1 - Determin the initial Q and C from the uniaxial tension tests
Q = ones(3,3)*1e3;      %Three tempers and three terms
C = ones(3,3)*1e2;
%Initial values and boundary conditions
modEqPlStrainTenCom1 = cell(3,1);
modEqStressTenCom1 = cell(3,1);
for i=1:3
    for j=1:2
        dYield = abs(yieldStresses2{i}{j}) - yield(i);
        if (i == 1)
            dYield = 0;
        end
        if ~(i == 1 && j == 2)
            iStart = find(modEqStress{i}{j} - dYield > yield(i));
            dEpsilon1 = modEqPlStrain{i}{j}(iStart(1));
            modEqPlStrainTenCom1{i} = [modEqPlStrainTenCom1{i};
                modEqPlStrain{i}{j}(iStart) - dEpsilon1];
            modEqStressTenCom1{i} = [modEqStressTenCom1{i}; modEqStress{i
                }{j}(iStart) - dYield];
        end
```

```matlab
        end
    end
[fitResults, GOF] = createFits(modEqPlStrainTenCom1{1}, modEqStressTenCom1
    {1}, modEqPlStrainTenCom1{2}, modEqStressTenCom1{2},
    modEqPlStrainTenCom1{3}, modEqStressTenCom1{3}, 1);
newYield = zeros(3,1);
for i=1:3
    coeffs = coeffvalues(fitResults{i});
    Q(i,:) = coeffs(4:6);
    C(i,:) = coeffs(1:3);
    newYield(i) = coeffs(7);
    %Sort C values based on
    sorting = true;
    while(sorting)
        Ctemp = C(i,1);
        sorting = false;
        for j=2:3
            if Ctemp < C(i,j)
                C(i,j-1) = C(i,j);
                Qtemp = Q(i,j-1);
                Q(i,j-1) = Q(i,j);
                C(i,j) = Ctemp;
                Q(i,j) = Qtemp;
                sorting = true;
            end
            Ctemp = C(i,j);
        end
    end
end
%Step 2 - Optimize eta in formulas of Chi and Voce terms
eta = ones(3,3,3)*0.25;       %Three tempers, three terms, three states (
    tension-compression, compression-tension and both)
x_LB =[0 0 0];
x_UB =[1 1 0];
for i=1:3
    modEqPlStrainTenCom1 = [];
    modEqStressTenCom1 = [];
```

```
modEqPlStrainTenCom2 = [];
modEqPlStrainTenCom2P0 = [];
modEqStressTenCom2 = [];
modEqPlStrainComTen1 = [];
modEqStressComTen1 = [];
modEqPlStrainComTen2 = [];
modEqPlStrainComTen2P0 = [];
modEqStressComTen2 = [];
for j=3:12
    if (j < 8)
        dYield = abs(yieldStresses2{i}{j}) − yield(i);
        iStart = find(modEqStress{i}{j}(1:listIU{i}{j−2}) − dYield >
            yield(i));
        dEpsilon1 = modEqPlStrain{i}{j}(iStart(1));
        modEqPlStrainTenCom1 = [modEqPlStrainTenCom1; modEqPlStrain{i
            }{j}(iStart) − dEpsilon1];
        modEqStressTenCom1 = [modEqStressTenCom1; modEqStress{i}{j}(
            iStart) − dYield];
        iStart2 = find(modEqStress{i}{j}(listIU{i}{j−2}:end) + dYield
            < − yield(i));
        iStart2 = listIU{i}{j−2} + iStart2(1);
        dEpsilon2 = dEpsilon1;
        s = modEqPlStrain{i}{j}(iStart2:end) − dEpsilon2;
        modEqPlStrainTenCom2 = [modEqPlStrainTenCom2; s];
        modEqPlStrainTenCom2P0 = [modEqPlStrainTenCom2P0; ones(length(
            s),1)*s(1)];
        modEqStressTenCom2 = [modEqStressTenCom2; modEqStress{i}{j}(
            iStart2:end) + dYield];
    else
        dYield = abs(yieldStresses2{i}{j}) − yield(i);
        iStart = find(modEqStress{i}{j}(1:listIU{i}{j−2}) + dYield < −
             yield(i));
        dEpsilon1 = modEqPlStrain{i}{j}(iStart(1));
        modEqPlStrainComTen1 = [modEqPlStrainComTen1; modEqPlStrain{i
            }{j}(iStart) − dEpsilon1];
        modEqStressComTen1 = [modEqStressComTen1; modEqStress{i}{j}(
            iStart) + dYield];
```

```matlab
            iStart2 = find(modEqStress{i}{j}(listIU{i}{j−2}:end) − dYield ...
                > yield(i));
            iStart2 = listIU{i}{j−2} + iStart2(1);
            dEpsilon2 = dEpsilon1;
            s = modEqPlStrain{i}{j}(listIR{i}{j−2} + 1:end) − dEpsilon2;
            modEqPlStrainComTen2 = [modEqPlStrainComTen2; s];
            modEqPlStrainComTen2P0 = [modEqPlStrainComTen2P0; ones(length( ...
                s),1)*s(1)];
            modEqStressComTen2 = [modEqStressComTen2; modEqStress{i}{j}( ...
                listIR{i}{j−2} + 1:end) − dYield];
        end
        Istart(i,j) = iStart(1);
        Istart2(i,j) = iStart2;
    end
end
%Tension−Compression
x0 = eta(i,:,1);
F1 = @(x) yield(i) + (1 − x(1))*Q(i,1)*(1 − exp(−C(i,1)* ...
    modEqPlStrainTenCom1)) ... %Yield + Voce1
    + (1 − x(2))*Q(i,2)*(1 − exp(−C(i,2)*modEqPlStrainTenCom1)) ...
        ...                 %Voce2
    + (1 − x(3))*Q(i,3)*(1 − exp(−C(i,3)*modEqPlStrainTenCom1)) ...
        ...                 %Voce3
    + x(1)*Q(i,1)*(1 − exp(−C(i,1)*modEqPlStrainTenCom1)) ...
        ...                     %Chi1
    + x(2)*Q(i,2)*(1 − exp(−C(i,2)*modEqPlStrainTenCom1)) ...
        ...                     %Chi2
    + x(3)*Q(i,3)*(1 − exp(−C(i,3)*modEqPlStrainTenCom1)); ...
                            %Chi3
F2 = @(x) − yield(i) − (1 − x(1))*Q(i,1)*(1 − exp(−C(i,1)* ...
    modEqPlStrainTenCom2))... %Yield + Voce1
    − (1 − x(2))*Q(i,2)*(1 − exp(−C(i,2)*modEqPlStrainTenCom2))... ...
                        %Voce2
    − (1 − x(3))*Q(i,3)*(1 − exp(−C(i,3)*modEqPlStrainTenCom2))... ...
                        %Voce3
    − x(1)*Q(i,1) + (x(1)*Q(i,1).*(1 − exp(−C(i,1).* ...
        modEqPlStrainTenCom2P0)) + x(1)*Q(i,1)).*exp(−C(i,1)*( ...
        modEqPlStrainTenCom2 − modEqPlStrainTenCom2P0))... %Chi1
```

```matlab
        - x(2)*Q(i,2) + (x(2)*Q(i,2).*(1 - exp(-C(i,2).*
            modEqPlStrainTenCom2P0)) + x(2)*Q(i,2)).*exp(-C(i,2)*(
            modEqPlStrainTenCom2 - modEqPlStrainTenCom2P0))...      %Chi2
        - x(3)*Q(i,3) + (x(3)*Q(i,3).*(1 - exp(-C(i,3).*
            modEqPlStrainTenCom2P0)) + x(3)*Q(i,3)).*exp(-C(i,3)*(
            modEqPlStrainTenCom2 - modEqPlStrainTenCom2P0));...     %Chi3
f = @(x)[(modEqStressTenCom1 - F1(x)); (modEqStressTenCom2 - F2(x))];
optimal_x = lsqnonlin(f,x0,x_LB,x_UB,options);
eta(i,:,1) = optimal_x;
%Compression-Tension
x0 = eta(i,:,2);
F3 = @(x) - yield(i) - (1 - x(1))*Q(i,1)*(1 - exp(-C(i,1)*
    modEqPlStrainComTen1)) ... %Yield + Voce1
    - (1 - x(2))*Q(i,2)*(1 - exp(-C(i,2)*modEqPlStrainComTen1))
        ...                %Voce2
    - (1 - x(3))*Q(i,3)*(1 - exp(-C(i,3)*modEqPlStrainComTen1))
        ...                %Voce3
    - x(1)*Q(i,1)*(1 - exp(-C(i,1)*modEqPlStrainComTen1))
        ...                   %Chi1
    - x(2)*Q(i,2)*(1 - exp(-C(i,2)*modEqPlStrainComTen1))
        ...                   %Chi2
    - x(3)*Q(i,3)*(1 - exp(-C(i,3)*modEqPlStrainComTen1));
                        %Chi3
F4 = @(x) yield(i) + (1 - x(1))*Q(i,1)*(1 - exp(-C(i,1)*
    modEqPlStrainComTen2))...       %Yield + Voce1
    + (1 - x(2))*Q(i,2)*(1 - exp(-C(i,2)*modEqPlStrainComTen2))...
                        %Voce2
    + (1 - x(3))*Q(i,3)*(1 - exp(-C(i,3)*modEqPlStrainComTen2))...
                        %Voce2
    + x(1)*Q(i,1) + (- x(1)*Q(i,1).*(1 - exp(-C(i,1).*
        modEqPlStrainComTen2P0)) - x(1)*Q(i,1)).*exp(-C(i,1)*(
        modEqPlStrainComTen2 - modEqPlStrainComTen2P0))...     %Chi1
    + x(2)*Q(i,2) + (- x(2)*Q(i,2).*(1 - exp(-C(i,2).*
        modEqPlStrainComTen2P0)) - x(2)*Q(i,2)).*exp(-C(i,2)*(
        modEqPlStrainComTen2 - modEqPlStrainComTen2P0))...     %Chi2
    + x(3)*Q(i,3) + (- x(3)*Q(i,3).*(1 - exp(-C(i,3).*
        modEqPlStrainComTen2P0)) - x(3)*Q(i,3)).*exp(-C(i,3)*(
```

```matlab
            modEqPlStrainComTen2 − modEqPlStrainComTen2P0));        %Chi3
    f = @(x)[(modEqStressComTen1 − F3(x)); (modEqStressComTen2 − F4(x))];
    optimal_x = lsqnonlin(f,x0,x_LB,x_UB,options);
    eta(i,:,2) = optimal_x;
    %Both directions
    x0 = eta(i,:,3);
    f = @(x)[(modEqStressTenCom1 − F1(x)); (modEqStressTenCom2 − F2(x)); (
        modEqStressComTen1 − F3(x)); (modEqStressComTen2 − F4(x))];
    optimal_x = lsqnonlin(f,x0,x_LB,x_UB,options);
    eta(i,:,3) = optimal_x;
end
%% Cockcroft − Latham Fracture Criterion to file
targetPath = 'C:\Users\kris_\Documents\NTNU\OneDrive − NTNU\Skole\
    Masteroppgave\Materialdata\';
Beta = −2:0.01:1;
triax = 1/sqrt(3)*(Beta + 1) ./(sqrt(Beta.^2+Beta+1));
halfwayIndex = 16;
mu = [3*(Beta(1:halfwayIndex) + 1)./(Beta(1:halfwayIndex) − 1),...
     3*Beta(halfwayIndex+1:end)./(Beta(halfwayIndex+1:end) + 2 )];
lode = atan(1/sqrt(3).*mu) + pi/6;
for i=1:3
    pf_ultimate = min([modEqPlStrain{i}{1}(end), modEqPlStrain{i}{2}(end)
        ]);
    fid_Brudd = fopen(strcat(targetPath,'Bruddkriterie − ',getTemperString
        (i),'.txt'),'w');
    formatSpec_Brudd = '%f  %f  %f\n';
    Wc = (1/3 + 2/3)*integral(@(p) yieldAvg(i) + Q(i,1)*(1−exp(−p*C(i,1)))
        + Q(i,2)*(1−exp(−p*C(i,2))) + Q(i,3)*(1−exp(−p*C(i,3))), 0,
        pf_ultimate);
    pf = zeros(1,length(Beta));
    syms p_f;
    pf(1) = 1e10;
    fprintf(fid_Brudd,formatSpec_Brudd,pf(1),triax(1),0);
    for j=2:length(Beta)
        pf(j) = real(vpasolve(yieldAvg(i).*p_f + Q(i,1)*((exp(−C(i,1)*p_f)
            −1)/C(i,1) + p_f) + Q(i,2)*((exp(−C(i,2)*p_f)−1)/C(i,2) + p_f)
            + Q(i,3)*((exp(−C(i,3)*p_f)−1)/C(i,3) + p_f) − Wc./(triax(j)
```

```matlab
            +(3-mu(j))/(3*sqrt(3+mu(j)^2))) == 0,p_f));
        fprintf(fid_Brudd,formatSpec_Brudd,pf(j),triax(j),0);
    end
    fclose(fid_Brudd);
end
%% Write MATERIAL PARAMETERS to file
p = linspace(0,5,10000);
for i=1:3
    fid_Isotropic = fopen(strcat(targetPath,'Material parameters -
        Isotropic -',getTemperString(i),'.txt'),'w');
    formatSpec_Isotropic = '%f   %f\n';
    fid_Combined_Iso = fopen(strcat(targetPath,'Material parameters -
        Combined_Isotropic -',getTemperString(i),'.txt'),'w');
    formatSpec_Combined_Iso = '%f   %f\n';
    for j=1:length(p)
        s = VoceThreePoints([Q(i,1) C(i,1) Q(i,2) C(i,2) Q(i,3) C(i,3)
            yieldAvg(i)],p(j));
        fprintf(fid_Isotropic,formatSpec_Isotropic, s,p(j));
        iso = VoceThreePoints([(1- eta(i,1,1))*Q(i,1) C(i,1) (1- eta(i
            ,2,1))*Q(i,2) C(i,2) (1- eta(i,3,3))*Q(i,3) C(i,3) yieldAvg(i)
            ],p(j));
        fprintf(fid_Combined_Iso,formatSpec_Combined_Iso, iso,p(j));
    end
    fclose(fid_Isotropic);
    fclose(fid_Combined_Iso);
    fid_Combined_Kin = fopen(strcat('Material parameters -
        Combined_Kinematic -',getTemperString(i),'.txt'),'w');
    %Format for Abaqus input of Kinematic Hardening parameters:
    %Yield   K_11    K_21    K_12    K_22
    formatSpec_Combined_Kin = '%f  %f  %f  %f  %f\n';
    %Using alpha and beta from tension-compression
    fprintf(fid_Combined_Kin,formatSpec_Combined_Kin,yieldAvg(i),eta(i
        ,1,3)*Q(i,1)*C(i,1),C(i,1),eta(i,2,3)*Q(i,2)*C(i,2),C(i,2));
    fclose(fid_Combined_Kin);
end
```